ENDGAME STRATEGIES FOR PLANETARY MOON ORBITERS

by

RYAN WOOLLEY
B.S., PHYSICS-ASTRONOMY, BRIGHAM YOUNG UNIVERSITY, 2003
M.S., ASTRONAUTICAL ENGINEERING, UNIVERSITY OF SOUTHERN CALIFORNIA, 2005

A thesis submitted to the
Faculty of the Graduate School of the
University of Colorado in partial fulfillment
of the requirements for the degree of
Doctor of Philosophy
Department of Aerospace Engineering Sciences
2010

This thesis entitled:
Endgame Strategies for Planetary Moon Orbiters
written by Ryan Woolley
has been approved for the
Department of Aerospace Engineering Sciences

Daniel Scheeres

George Born

Steve Nerem

Rodney Anderson

Elizabeth Bradley

Date_____

The final copy of this thesis has been examined by the signatories, and we find that both the content and the form meet acceptable presentation standards of scholarly work in the above-mentioned discipline.

ABSTRACT

Woolley, Ryan Cliff (Ph.D. Aerospace Engineering Sciences)

Endgame Strategies for Planetary Moon Orbiters

Directed by Daniel Scheeres, Professor, Department of Aerospace Engineering Sciences, University of Colorado at Boulder

Delivering an orbiter to a planetary moon such as Titan or Europa requires an exorbitant amount of fuel if the trajectory is not carefully and cleverly planned. V-infinity leveraging maneuvers are an effective means to reduce total Delta-V requirements to achieve orbit about a planetary satellite. This work seeks to characterize optimal trajectories making use of flybys, leveraging maneuvers, and capture orbits in order to minimize fuel requirements. With the aid of customized tools to construct, map, and analyze sequences of resonances and maneuvers, we derive heuristics of global optima and formulate a theoretical minimum. The theoretical minimum, which is found using an infinite series of flybys and leveraging maneuvers, results in a Delta-V savings of over 70% when compared to a direct insertion during flyby. We then generate numerical results, which show that the optimal location for performing V-infinity reduction maneuvers is not necessarily at apoapsis, due to targeting constraints. By plotting total Delta-V vs. time-of-flight for tens of thousands of generated sequences, a Pareto front is created of the most

efficient sequences for each given flight time. This Pareto front shows that while infinite missions are not possible, it is feasible to reduce the total Delta-V by 50% with only a modest increase in flight time. Increasing the mission duration further does not result in significant reductions.

It is shown that periodic orbits exist in the restricted three-body problem whose Jacobi constants correspond to a positive V-infinity in the two-body problem. This indicates that these orbits are classically hyperbolic and yet are gravitationally bound to the vicinity of the target body. This dissertation explores the limits and usefulness of these hyperbolic periodic orbits and their application to the endgame problem. Families of orbits are generated using a single shooting method and integrated into the final phase of V-infinity leveraging sequences. Using a hyperbolic periodic orbit to capture to the vicinity of a target moon following an optimized sequence of leveraging maneuvers and flybys yields significant fuel savings (60-70%) over direct trajectories.

DEDICATION

This dissertation is dedicated to my wife, Venessa, and to my beautiful young children, Jeremy and Chloe. My quest for more education brought you into my life, and for that I will be eternally grateful.

> "…yea, and all things denote there is a God; yea, even the earth, and all things that are upon the face of it, yea, and its motion, yea, and also all the planets which move in their regular form do witness that there is a Supreme Creator."
>
> Alma 30:44

ACKNOWLEDGEMENTS

First and foremost, I need to thank my wife, Venessa, for loving me unconditionally and supporting me more than I could have imagined was possible. Your love and encouragement help me to believe that I can accomplish anything. You believed in me and helped pick me up when I was discouraged. Your ability to understand science and engineering constantly amazes me. The conversations we have had about my research made my project better and allowed me to complete this dissertation. Your expertise in technical editing has kept this dissertation readable and intelligible. I cannot thank you enough for all of the help you have provided.

I am also indebted to Dr. Scheeres for his constant support in this research. He helped me focus my efforts and steered me through the difficulties incumbent upon projects of this magnitude. His ability to immediately delve right into the deepest subject matter and recall governing principles and equations always astounds me.

I began my time at the University of Colorado under the guidance of Dr. George Born, whose reputation and accomplishments brought me to the university in the first place. I am grateful for all the time he spent with me as my advisor over the first two years of my study. Dr. Born was also instrumental in my acquiring a part time research position at the Laboratory of Atmospheric and Space Physics (LASP), which funded the majority of my studies here in Colorado. I also met many

wonderful and brilliant people at LASP as well as learning many valuable skills that will serve me well throughout my career.

I also wish to thank my fellow graduate students with whom I have had the pleasure to associate. Jeff Parker, Brandon Jones, Rodney Anderson, and Kate Davis served as excellent TA's for interplanetary mission design and quickly became mentors, teammates, and friends that made my experience here all the more enjoyable.

CONTENTS

LIST OF TABLES

LIST OF FIGURES

1 Introduction

The Cassini-Huygens spacecraft entered orbit about Saturn on July 1, 2004. On Christmas day of that year, the Huygens probe was released and made its way towards the surface of Titan. The data sent back from Huygens and Cassini about this amazing moon were nothing short of astounding. They revealed an icy world with methane seas and a thick organic haze, with rugged shorefronts and winding canyons. Scientific interest in Titan exploded and the community called for plans to send a dedicated orbiter.

Missions being studied by the National Aeronautics and Space Administration (NASA) at the time (e.g. Titan Explorer) required the use of aerocapture, an unproven technology, to enable a spacecraft to enter orbit about Titan. Studies had shown that aerocapture would allow 2.4 times as much mass to be delivered when compared to an all-propulsive trajectory (Edwards, 2005). However, in 2007, it was decided that aerocapture was too great of a risk, both technologically and in cost, to be included in baseline architectures. The problem of how to minimize the fuel requirements of a chemical trajectory to a Titan orbit in order to enable a mission without aerocapture became the impetus for this research.

1.1 Motivation

In situ exploration of the outer planets and their moons over the past 40 years has given us spectacular imagery of alien worlds and has revolutionized our scientific understanding. In 1973, Pioneer 10 was the first spacecraft to make direct observations of Jupiter as it flew by on its way out of the solar system. Later, the Voyager spacecrafts were launched in 1977 in order to take advantage of the Grand Tour possibility of the outer planets. They were launched two weeks apart (Voyager 2 first) and both flew by the Jovian and Saturnian systems. Because Pioneer 11 had detected a thick, gaseous atmosphere over Titan one year earlier, the Voyager space probes' controllers at the Jet Propulsion Laboratory elected for Voyager 1 to make a close approach of Titan and of necessity, end its Grand Tour there. Voyager 2 continued the tour to Uranus and Neptune. Figure 1.1 is an artist rendering of the spacecrafts that were the first to fly by and to orbit Jupiter and Saturn.

Figure 1.1. Past Missions to the outer planets. Pioneer (1973) and Voyager (1979) were the first to fly by Jupiter and Saturn, respectively. Galileo orbited Jupiter from 1995 to 2003 and returned wonderful data on the whole system. Cassini-Huygens was launched in 2004 and continues to send invaluable data on the Saturnian system, including Titan.

In 1989, the nearly 3 ton interplanetary probe Galileo was sent to study the Jovian system. Galileo arrived in 1995, and despite the failure of its high-gain antenna, it continued to send groundbreaking images and information until it was plunged into Jupiter in 2003. The next NASA flagship mission, Cassini-Huygens, was a joint effort with the European Space Agency. Launched to Saturn in 1997, Cassini continues to orbit Saturn today. Recently the mission was extended until 2017, enabling another 155 revolutions around the planet - 54 flybys of Titan and 11 flybys of Enceladus.

NASA has sanctioned dozens of studies for over a decade to determine the next flagship mission (> $1B) to follow Galileo and Cassini. Some examples include

Europa Orbiter, JIMO, and the Titan Explorer. The Outer Planets Assessment Group (OPAG) was established by NASA in late 2004 to identify scientific priorities and pathways for exploration in the outer solar system. The group consists of a 15-person steering committee, which actively solicits input from the scientific community and reports its findings to NASA Headquarters. OPAG has held numerous meetings to determine scientific benefits and technological feasibility for dedicated missions to most of the outer planets.

In 2007-2008 NASA and ESA put forth various concepts for missions to Saturn and Jupiter. In February 2009, NASA and ESA officials selected the Europa Jupiter System Mission (EJSM) as the next Outer Planet Flagship Mission, but it was also decided to continue pursuing another potential mission to the Saturnian system. Both missions require the delivery of large payloads to useful scientific orbits about planetary moons, a task that can require an excessive amount of fuel if the trajectory and implementation are not carefully and cleverly planned.

This dissertation makes extensive use of normalized quantities and generalizing assumptions so as to make the results applicable to any three-body system and not just the Saturn-Titan System. The hope is that the principles and concepts set forth in this research will aide in the global effort to explore the many interesting moons of the solar system.

1.2 Problem Characterization

The final phase of a trajectory to a science orbit is known as the "endgame." This phase is very challenging and often tedious for mission designers (Sweetser et

al., 1997). Typical science orbits require close proximity to the surface and high inclinations to provide global coverage for mapping purposes. These orbits are very costly (fuel-wise) to achieve via direct insertion. Furthermore, since delivering the desired scientific payloads requires large amounts of fuel, missions are limited by launch vehicle capabilities. There are a variety of techniques and tools available to aide in the reduction of the total required ΔV[1]. Recently much work has been done to determine how to optimally apply these techniques to meet mission requirements and to minimize manual effort (Sims et al., 1997; Ross and Grover, 2007a; Brinckerhoff and Russell, 2009; Campagnola and Russell, 2010a; Ross and Scheeres, 2007; Casalino et al., 1998).

In practice, missions to planetary moons such as Europa and Titan employ the use of extensive tours with multiple gravity-assists in order to reduce hyperbolic excess velocity[2] (hereafter referred to as V_∞) at the final moon encounter, enabling a feasible orbit insertion. Figure 1.2 shows the trajectory of the Europa Explorer (Clark, et al., 2007). The mission begins with a flyby of Venus and two at Earth en route to Jupiter. Upon arrival, a flyby of Callisto is used to lower the fuel needed for the large Jupiter orbit insertion (JOI) burn. Following capture in the Jovian system, the spacecraft begins a tour of highly elliptical orbits using flybys of the massive moons to remove orbital energy and to set up the final insertion at Europa. The

[1] The cost of impulsive maneuvers can be expressed in terms of mass, but this measure is dependent on the dry mass of the spacecraft and the efficiency (I_{sp}) of the engine. Instead, it is more common to express the effects of impulsive maneuvers in terms of the magnitude of the change in velocity they produce, known as ΔV, which can be used as a surrogate for fuel usage.

[2] See Appendix A: Nomenclature at the end of this dissertation for a description of symbols used

energy-reducing tour and final capture (steps 3 and 4 in Figure 1.2) make up the "endgame".

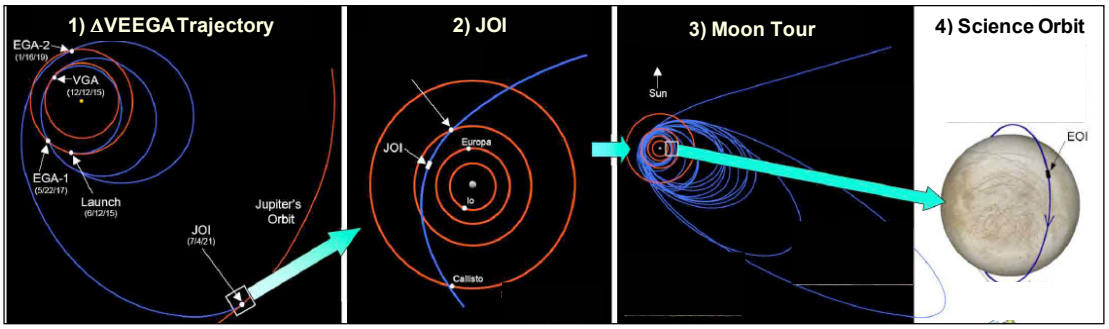

Figure 1.2. Typical mission sequence to Europa. Following a lengthy interplanetary tour (1) and large JOI burn (2), the endgame is comprised of an energy-reducing tour (3) and orbital capture at Europa (4).

These tours also serve as opportunities to study the planetary environment and to target fly-bys of other moons. However, gravity-assists alone do not change the V_∞ magnitude. V_∞ at the target moon is only reduced via ΔV maneuvers and gravity-assists at other moons. In this research we simplify the problem by ignoring the existence of other moons and characterize the optimal use of ΔV maneuvers to enable orbital capture.

One particular technique that has proven useful in planetary tour design is the V_∞ leveraging maneuver (Boutonnet et al., 2008; Johannesen and D'Amario, 1999). This approach makes use of small, deep-space maneuvers near apoapsis to alter the V_∞ magnitude at the next fly-by. The change in V_∞ can be 5-10 times or more the size of the deep-space burn. One aim of this research is to aid in the understanding of the dynamics governing V_∞ leveraging maneuvers and their use in planetary endgame tours. Sims and Longuski (1994, 1997) laid much of the groundwork on these maneuvers in the 90's. Their work has been followed with renewed interest in the

past few years as evidenced by the papers of Campagnola (2010a, 2010b) and Brinkerhoff (2009). This dissertation will focus on same-body transfers (as opposed to multi-moon tours) where only one body is used during the endgame. We will also confirm some of the findings of the research mentioned above. The results are presented with the mission designer in mind who wishes to quickly evaluate the possibilities and trade space before moving to a more detailed trajectory.

In order to better visualize the optimization of the endgame design process, we propose the use of a three-dimensional "V_∞ Sphere" as a guide map. This map is based on the "V_∞ Globe"[3] as proposed by Strange and Russell (2007). As spacecraft maneuvers are performed the magnitude of the V_∞ vector, which will later be shown to be analogous to the Jacobi constant, is modified. Strategically placed maneuvers will reduce the size of the V_∞ Globe at the next encounter, which can be thought of as the next layer of the V_∞ Sphere. The contours delineating post fly-by orbit parameters on the surface of the V_∞ Globe trace out three-dimensional surfaces as the size of the sphere shrinks. Getting to the center of this sphere using the minimal amount of fuel is the ultimate goal of the endgame design process.

Traditional planetary capture methods require that this V_∞ Sphere be reduced to zero, which is not possible using fly-bys alone. With the additional use of V_∞ leveraging maneuvers, it is possible to greatly reduce the amount of fuel required to bring down the V_∞ magnitude and ultimately capture into an orbit about the body. With the V_∞ Sphere providing a map for potential orbit sequences, the problem

[3] We will use the term "globe" to denote a surface, whereas "sphere" is used to denote the entire 3-dimensional object.

becomes how to optimally shrink the sphere. V_∞ leveraging maneuvers are typically performed at the spacecraft's apoapsis and tangent to the orbit. Sweetser (1993) showed that this maximizes the change in Jacobi constant. However, our numerical investigations have shown that this is slightly suboptimal due to the targeting restraints when solving Lambert's problem.

In the 2-body problem (2BP), V_∞ at the target moon is a constant in the absence of perturbations or leveraging maneuvers, much like the Jacobi constant in the 3-body problem (3BP). Since gravity assists and the transition to gravitational capture are essentially expressions of third body effects, it makes more sense to analyze them using three-body techniques. In the patched 2BP, $V_\infty = 0$ corresponds to a parabolic orbit or the limit of gravitational capture. Relationships between the Jacobi and V_∞ yield the possibility of bound, periodic, or quasi-periodic orbits with a positive V_∞. If such orbits exist, then they would amount to hyperbolic orbits in the 2-body sense yet be bound to the vicinity of the secondary. Targeting a "hyperbolic periodic" orbit during the final phase of a leveraging maneuver sequence would result in a lower required insertion ΔV.

1.3 Historical Roots

The purpose of this section is to provide a brief history of previous work in astrodynamics that has lead to modern day mission design and to show the background leading up to this dissertation.

1.3.1 A Brief History of Two-Body Problem

Great minds throughout the ages have been interested in the celestial motions they observed in the night sky. In 1601, Johannes Kepler became the director of the Prague Observatory following the death of Tycho Brahe. Using Brahe's meticulously collected data, Kepler formulated his famous three laws of planetary motion:

1) Every planet moves in an elliptical orbit, with the sun at one focus.

2) The radius vector sweeps out equal areas in equal times.

3) The square of the period is proportional to the cube of the semimajor axis.

Later that century, Newton (1687) would go on to devise his three laws of motion and put forth his theory of gravitation:

$$F = \frac{Gm_1m_2}{r^2} \tag{1.1}$$

where G is the universal gravitational constant and r is the distance between mass 1 (m_1) and mass 2 (m_2). Armed with his newly invented calculus and laws of gravitation, Newton set out to explain Kepler's laws. He succeeded in mathematically and geometrically describing the laws that govern planetary motion and derived many of the equations that are used today.

In 1744, Leonhard Euler went on to find the full analytical solution to the two-body equations. He was also one of the first to derive the equations defining the change in osculating elements with time, giving rise to the analytic theory of perturbed motions (Euler, 1744). In works published in 1761 and 1771, Johann Lambert used a geometrical approach to generalize Euler's formulas to include elliptical and hyperbolic orbits. Therefore, solving for the orbit between two known position vectors is usually known as Lambert's problem (see 2.1.3). General

understanding of orbit determination in the 2BP was further enhanced by the works of Lagrange (1778), Laplace (1880), and Gauss (1802).

One of the most well known transfers in the two-body problem is the Hohmann transfer. Hohmann (1925) proposed a theory which suggests that the minimum cost transfer between two circular orbits, in terms of fuel expenditure, can be achieved by employing two burns: the first maneuver is tangential to the initial orbit, and the second maneuver is tangential to the final orbit. The Hohmann transfer represents the minimum change in velocity between most coplanar orbits.

1.3.2 A Brief History of the Three-Body Problem

The 3BP is a classic problem of celestial mechanics, wherein we are interested in the motion of a third particle in the presence of two massive bodies. One of the earliest contributors to the 3BP was Sir Isaac Newton (1687), in the years after he published his theory of gravitation. The problem of ocean navigation required an understanding of the motion of the Moon, which is strongly affected by both the Earth and the Sun and, hence, beyond the scope of the basic 2BP. This problem was of great interest throughout the eighteenth century and was approached in basically two ways: by an infinite series expansion to describe the solution (Clairaut, 1752) or by variation of parameters (Euler, 1744). It was Euler who first used rotating coordinates to frame the problem. However, it was not until 1772 that Lagrange (1867-1892) demonstrated a reduction of the problem from its original form, with 18 unknowns, to a problem of order 7 in the rotating frame. Lagrange proposed the assumptions that lead to the "restricted" model, allowing closed form solutions and more detailed analyses of celestial motions (Barrow-Green, 1997).

It was also Lagrange who first identified the five equilibrium points in the circularly restricted three-body problem (CR3BP): the three collinear points (which were also described by Euler in 1772) and two equilateral points. This is why they are usually denoted the Lagrange points.

The next significant contribution to the 3BP did not appear until Carl Jacobi in 1836. He discovered the only integral of the motion in the CR3BP, which bears his name as the Jacobi Constant. Jacobi's work was further extended by Hill (1878) who used this lone integral to define curves of zero velocity that limit the motion of the third particle. Hill's investigations focused on the Moon and, thus, constrained the Moon's motion to certain regions of space around the two main bodies (the Sun and the Earth).

Another significant step in understanding the three-body problem came about due to a mathematical competition to honor the 60th birthday King Oscar II of Sweden and Norway in 1889. Henri Poincaré was awarded the prize for his study of the CR3BP. What set his work apart was that he shifted from a quantitative aspect to a more qualitative assessment. While Poincaré (1890) was interested in finding solutions to the three-body problem, his approach differed from all previous developments, since he was more interested in the nature of the solutions than in the actual solutions themselves. His mathematical work showed that an infinite number of periodic orbits exist in the 3BP. Poincaré also introduced an innovative method, the Poincaré section (or stroboscopic map) to study the behavior of solutions as time tends to infinity (Barrow-Green, 1997). Poincaré is considered by many to be the father of dynamical systems theory.

Around the turn of the century, there was much work being done in the field of dynamical systems theory. Tisserand (1896) used it to study and identify comets and their orbits. Lyapunov (1892) and Levi-Civita (1901), were interested in a more general theory of the stability of motion, and in the case of Levi-Civita, its application to the CR3BP. Their work laid the foundation for modern efforts to compute the invariant manifolds associated with periodic orbits in the 3BP. Other notable researchers in the areas of periodic orbits and general solutions include Darwin (1897, 1911), Sundman (1912), and Strömgren (1935).

Continuing advancements in the determination of periodic orbits and the advent of modern computers and technology led to the launch of the ISEE-3 spacecraft in 1978 (Farquhar, 1998). It was the first spacecraft to be inserted into a halo orbit in the vicinity of the L1 Sun-Earth libration point. Since then many spacecraft have benefited from orbits determined by dynamical systems theory, including SOHO, ACE, and Genesis. Other researchers that have contributed significantly to the understanding of periodic orbits include Hénon (1965-1970), Szebehely (1967), and Broucke (1968).

1.3.3 Recent Related Work

In the past few decades, many new techniques have been developed in support of missions to the outer planets and their moons. In the late 1990's and early 2000's, a multitude of papers were published concerning mission designs to Europa and other moons of Jupiter. Most of these were in support of the Europa Orbiter or Jupiter Icy Moons Orbiter (JIMO) missions. In 1997, Ted Sweetser and others spelled out "a plethora of astrodynamic challenges" facing trajectory design for a Europa Orbiter.

Mission designers and theorists alike set to work tackling these problems incumbent upon sending an orbiter to a small planetary moon.

The first challenge facing designers was the daunting task of finding a tour design that reduced the Jovicentric energy while simultaneously meeting all the other mission criteria. In 1999, Johannesen and D'Amario of JPL published the reference trajectory of the Europa Orbiter, which was the baseline for most studies of the day. However, this was only a point design[4] and inflexible to schedule or requirement changes. Heaton and others at Purdue set to work on an automated process that took in constraints on total time of flight and radiation dosage (Heaton, et al., 2000). They found an enormous number of possible sequences and documented the most promising.

The dynamics of the multi-moon environment lends itself well to optimization techniques and the application of dynamical systems theory. A number of researchers tackled this problem including Ross and Grover (2007b), who looked at low thrust and multiple gravity-assists to navigate the unstable manifolds on near-ballistic trajectories, with the aid of Keplerian maps. Papers by Strange and Longuski (2002) and Strange, Russell, and Buffington (2007) also put forth graphical methods for the design of tours with gravity-assists, including the V_∞ Globe (see Section 3.4).

Another problem identified early on was the stability of suitable science orbits. Scheeres, Guman, and Villac (2000, 2001) studied orbital stability using numerical and analytical techniques. They found that impact orbits only occur within ~45° of a polar orbit, but with certain initial conditions, impact can be delayed for a

[4] The launch date for Europa Orbiter was set for 2003.

considerable length of time. Gomez, Lara, and Russell (2006) took a dynamical systems approach to find orbits that were stable and met mission criteria by using averaged manifolds of unstable frozen orbits. Achieving these low orbits directly using an insertion maneuver is often very costly, fuel-wise. That is why Russell and Lam (2005, 2006) looked in to the use of unstable, periodic orbits as an intermediate capture mechanism. This idea of using quasi-periodic orbits for orbital capture was also studied by Nakamiya, et al. (2007), with applications to periodic orbits about libration points.

Most recently, the well established technique of V_∞ leveraging has been applied to the planetary moon tour problem (Brinkerhoff and Russell, 2009). Used in conjunction with resonant gravity-assists, it becomes a pathfinding problem to find optimal tour sequences. Campagnola and Russell (2010a, 2010b) developed Tisserand leveraging graphs and phase-free formulae in order to analyze the endgame to the multi-body gravity-assist problem. Their results help find the minimum ΔV transfers between two moons and have been applied to enable an Enceladus[5] orbiter (Strange et al, 2009a; Campagnola et al., 2010c).

1.4 Contributions of This Dissertation

As shown by the previous section, much work has been done that is applicable to mission design of planetary moon orbiters. However, some techniques are developed as solutions to very specific, mathematically interesting problems. These theoretical discoveries can be quite clever, but fail to be implemented in the practical

[5] Enceladus is difficult to orbit in that it is very small and close to Saturn.

realm as mission designers are not given the big picture nor the tools to easily incorporate them into their studies. Other techniques are well developed, but are only applicable to one small phase of the problem and are difficult to mesh with other techniques. This dissertation seeks to connect multiple techniques together so that they can be seen as a whole. From there, mission designers will be able to quickly assess the usefulness of techniques across the trade space.

As was mentioned previously, the tour design problem lends itself well to optimization schemes. However, optimization schemes are only as accurate as their inputs and often times can only provide local optima, unbeknownst to the user. In order to avoid these pitfalls it is important to have a firm understanding of the big picture to be able to describe the problem accurately. Most trajectory optimization software requires the input of a relatively good initial guess. In this work we seek to characterize the trade space and provide approximations of global minima as inputs to high fidelity optimizers.

The cartoon in Figure 1.3 shows the stages of our overall endgame strategy. The trajectory begins with a highly elliptical orbit following Saturn or Jupiter Orbit Insertion (JOI). Next, an alternating sequence of targeted flybys and leveraging maneuvers are used to reduce the V_∞ at the target moon. The design of these sequences is aided by the use of a map – the V_∞ Sphere. Finally, a three-body capture orbit is used to reduce ΔV requirement to capture to the moon's vicinity.

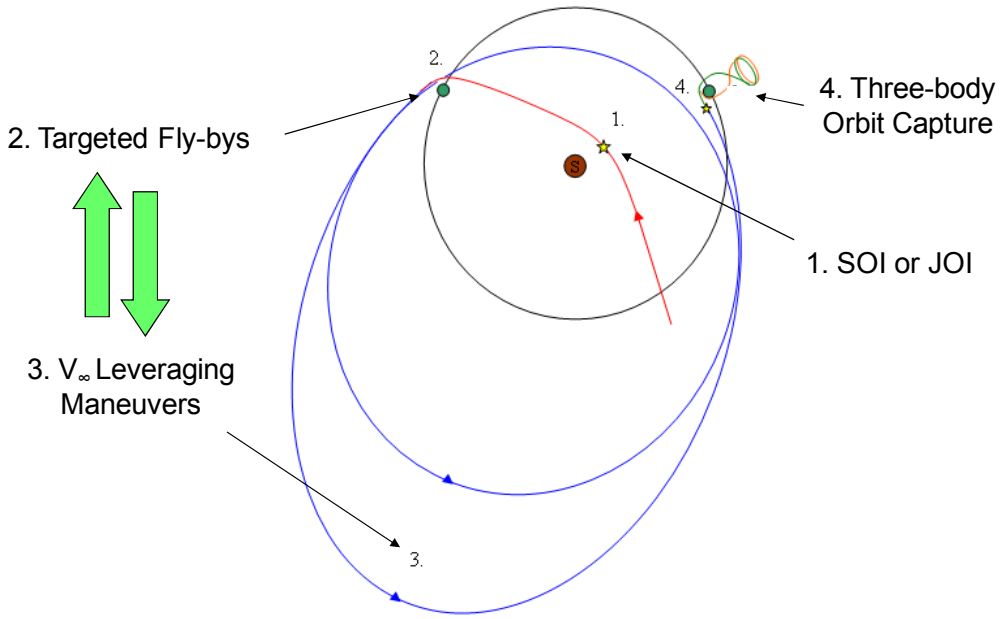

Figure 1.3. Cartoon of general endgame strategy. 1. Orbital Insertion. 2. and 3. Alternating sequence of flybys and leveraging. 4. Three-body orbit capture.

This dissertation provides a new method for the design and analysis of V_∞ leveraging maneuvers – the Lambert solution technique. This allows us to quantify and optimize these maneuvers with the aide of efficiency contours. This technique frees some of the constraints traditionally placed on leveraging maneuvers (e.g. that the maneuver take place exactly at apoapsis).

Armed with this tool, we generate tens of thousands of resonance sequences that are optimized at each leveraging maneuver. The results allow us to analyze the trends that characterize optimal trajectories. They also provide the mission designer with a good understanding of the trade off between the reduction of total ΔV and the increase in total time-of-flight.

The final section of this dissertation explores the relationships between the two- and three-body problems. This is useful during the capture phase as the

transition to the target moon's sphere of influence is better understood in the three-body realm. We show that hyperbolic periodic orbits do exist and can be more useful as capture mechanisms than standard two-body orbits. We also provide common terminology and metrics that allow us seamlessly connect the capture portion of a trajectory to the tour sequence and evaluate its usefulness.

Portions of this research have been presented at the following conferences:

1. *AAS/AIAA Astrodynamics Specialist Conference,* Pittsburgh, Pennsylvania, August 2009. AAS Paper 09-377, "Shrinking the V-infinity Sphere: Endgame Strategies for Planetary Moon Orbiters."
2. *AAS/AIAA Spaceflight Mechanics Meeting,* San Diego, CA, February 2010. AAS Paper 10-219, "Optimal Pathways for Sequences of V-infinity Leveraging Maneuvers."
3. *AAS George H. Born Symposium,* Boulder, CO, May 13-14, 2010. "Hyperbolic Periodic Orbits in the Three-Body Problem and Their Application to Orbital Capture."

It is also contained in the following (submitted) journal papers:

1. Woolley, R.C. and D.J. Scheeres, "Applications of V-infinity Leveraging Maneuvers to Endgame Strategies for Planetary Moon Orbiters," *Journal of Guidance, Control, and Dynamics*, Submitted Mar. 2010.
2. Woolley, R.C and D.J. Scheeres, "Hyperbolic Periodic Orbits in the Three-Body Problem and Their Application to Orbital Capture," *The Journal of the Astronautical Sciences*. (Pending submission).

1.5 Dissertation Organization

This dissertation is organized as follows: Chapter 2 reviews the models and methods used throughout this research. As the majority of the results are meant to rapidly characterize a trade space and to be used for preliminary analysis, 2BP equations are largely used. However, the transition to the sphere of influence of the secondary during capture is better suited to the 3BP. Therefore, a discussion of the 3-body approximation and trajectory design along with the relevant equations are put forth. The chapter is concluded with the mathematical relationship between integrals of motion in the two- and three-body problems.

Chapter 3 describes the use of V_∞ leveraging maneuvers during endgame sequences. The V_∞ Sphere, Globe, and Plane are introduced as maps of all possible orbits resulting from same body transfers. With the aid of these maps, we tackle the problem of finding sequences of leveraging maneuvers, flybys, and resonant orbits that lead to $V_\infty = 0$. A novel method for analyzing the leveraging maneuvers using a Lambert's solver is put forth. This method allows us to better understand the dynamics involved in designing the most efficient maneuvers. Using maximum efficiency plots, a theoretical minimum capture ΔV is derived.

Since the minimum also requires an infinite flight time, we then look at feasible sequences that may be used in tour design at Saturn or Jupiter. The combinatorics of the pathfinding problem lead to an infinite number of possible sequences. A Monte Carlo-type simulation is used to generate tens of thousands of

sequences and to analyze their characteristics. It was found that it is possible to reduce the total ΔV by 50% with only a modest increase in total time-of-flight. Increasing the mission duration further does not result in significant reductions.

Chapter 4 looks at ways to use three-body dynamics to become captured to the vicinity of the target moon without having to reduce V_∞ to zero first. Simple periodic orbits exist in the 3BP that are hyperbolic in the 2BP during the point of closest approach. Using these orbits as a capture mechanism, it is possible to expend approximately 25% less fuel during the insertion maneuver when compared to a similar elliptical orbit.

Chapter 5 draws conclusions from this research and its applications in the practical realm. We also suggest areas of future research that would be beneficial to the study of endgame strategies.

2 Models and Methods

In order to perform analyses of endgame strategies, this dissertation makes use of the equations of motion from the Two-Body model and the Circular Restricted Three-Body model. The Two-Body model is used for analyzing the motion of a spacecraft in the presence of one massive body and excludes any other perturbations. It is accurate under the assumptions listed in Section 2.1 and can be "patched" together to simulate trajectories with multiple bodies. It is the primary model used in the analysis in Chapter 3. The Circular Restricted Three-Body model assumes two massive bodies in circular orbits about their common barycenter. This approximates most planets and moons in our solar system quite well. The augmented equations of motion in this model allow for more complex orbits and it is the model used for analyses in Chapter 4.

2.1 The Two-Body Problem

The two-body problem (2BP) is the starting point for nearly all reference books in the field of astrodynamics. The basic problem describes the motion of two point-masses in mutual gravitational attraction. It is very well suited for quick approximations of trajectories in practical applications (including this dissertation) as most celestial bodies are spherically symmetric and the gravitational forces of one

body dominate all other perturbations for the majority of orbits. Newton's law of gravitation in Equation 1.1 leads to closed form solutions to the motions of the bodies with respect to the center of mass. These solutions can be used to analyze orbital properties without the need for cumbersome numerical propagation.

When the formula for gravitation force is applied to the two bodies, the equation relating each body's position with respect to the center of mass of the system may be written:

$$\ddot{\bar{r}}_{cm} = -\frac{G(m_1 + m_2)}{r_{cm}^3}\bar{r}_{cm} \tag{2.1}$$

where $\bar{r}_{cm}$ is the vector between either of the bodies and center of mass. In the case where one of the bodies is much smaller than the second ($m_1 >> m_2$)[6], such as an artificial satellite, we can neglect its mass and consider the center of mass to be the center of the larger body. The position vector magnitude, r, is now the distance from the larger body and the satellite. We can also replace Gm_1 with the more common mass parameter, μ. This leads to the simplified equation of motion for the satellite:

$$\ddot{\bar{r}} = -\frac{\mu_1}{r^3}\bar{r}\,. \tag{2.2}$$

Equation 2.2 is the basic two-body equation and is a second-order, nonlinear, vector, differential equation. It is the basis of the development of the remainder of the equations in this section, but it is only valid under the following assumptions:

1) No other forces act on either body except for their mutual gravitational attraction.

[6] For this dissertation the largest body will always have the lowest subscript, i.e. $m_1 > m_2 > m_3$

2) The bodies are spherically symmetric with uniform density and can therefore be treated point masses.

3) The mass of the smaller body is negligible compared to the central body.

4) The coordinate system must be inertial.

Manipulating Equation 2.2 gives what is known as the trajectory equation, which describes the shape of all two-body orbits:

$$r = \frac{a(1-e^2)}{1+e\cos(\nu)}, \tag{2.3}$$

where a is the semimajor axis, e is the eccentricity, and ν is the true anomaly. It shows that all trajectories are conic sections: circles, ellipses, parabolas, or hyperbolas. The shape that an orbit will take, and whether it is gravitationally bound or unbound to the central body, is determined by the specific mechanical energy. This energy is computed by subtracting the potential energy[7] from the kinetic energy:

$$E = \frac{v^2}{2} - \frac{\mu}{r}, \tag{2.4}$$

where v is the velocity of the satellite with respect to the central body. When energy is positive the orbit is hyperbolic and the satellite will escape the system. If energy is negative then the satellite is gravitationally bound and will follow an elliptical or circular orbit. Zero energy denotes a parabolic orbit where velocity goes to zero at an infinite distance and represents the boundary of gravitational capture.

The simplifying assumptions of the 2BP allow it to be a very well-characterized system. One way to look at it is to consider that all particles have 6

[7] Since potential energy is negative, it is actually added to kinetic, which is positve

degrees of freedom: 3 in position and 3 in velocity. If 6 constants, or integrals of motion, can be defined, then the motion can be known for any given time. The 2BP has 12 degrees of freedom, but since we assume that the first body is massive and fixed at the barycenter, the conservation of linear momentum allows us to eliminate 6. Conservation of energy (Equation 2.4) provides the first integral, and conservation of angular momentum along with Kepler's first two laws provide the remaining 5. Keep in mind this only provides a complete solution to the *relative* motion of the two bodies due to the assumptions listed above.

2.1.1 Orbital Parameters

Since we know that the angular momentum vector, $\boldsymbol{h} = \boldsymbol{r} \times \boldsymbol{v}$[8], is constant, the plane of the orbit is fixed in space. The $\boldsymbol{r}$ and $\boldsymbol{v}$ vectors lie in this plane which is normal to $\boldsymbol{h}$. Now let us define a reference plane that is fixed in inertial space. The angle between the planes is fixed and is called the inclination, i. Two more angular parameters define their relative orientation, as shown in Figure 2.1. The first, the longitude of the ascending node, Ω, is the angle between the x-axis (arbitrarily defined) and the line of nodes between the planes. The second is the argument of periapsis, ω, which measures the angle between the line of nodes and the point of periapsis.

The size and shape of an orbit are determined by two parameters – semimajor axis, a, and eccentricity, e. The semimajor axis is determined by the energy of an orbit as shown by the equation

---

[8] $\boldsymbol{v} = \dot{\boldsymbol{r}}$, or $d\boldsymbol{r}/dt$

$$E = -\frac{\mu}{2a}. \tag{2.5}$$

The eccentricity determines the shape of the orbit, ranging from a circle ($e = 0$), to an ellipse ($0 < e < 1$), all the way to a hyperbola ($e > 1$).

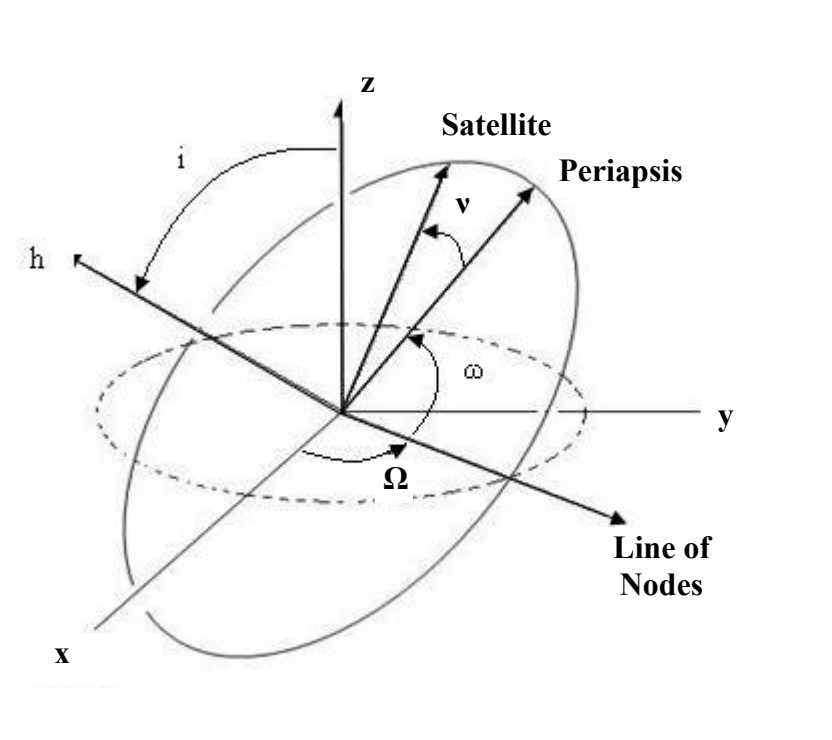

Figure 2.1. Two-Body orbital parameters. The reference plane and orbital plane are fixed in inertial space. Three angular quantities define their relationship and a fourth, ν, denotes the spacecraft's position on the orbit.

These five parameters (a, e, i, Ω, and ω) completely describe a spacecraft's orbit and its orientation in space. A sixth parameter, the true anomaly, ν, is needed to indicate its location on the orbit. True anomaly is measured from the point of periapsis to the spacecraft in the direction of travel and varies with time, whereas the others do not. The six parameters, or some variation of them, are commonly known as the orbital elements. They can readily be converted to position and velocity vectors and vice versa.

2.1.2 Orbital Transfers

One of the basic goals of space exploration missions is to get from one place to another. The mechanism for doing so is known as a transfer orbit. The most basic and common transfer is from one circular orbit to another co-planar circular orbit. In practice most orbits are not exactly circular nor co-planar, but the analysis of such transfers is a good approximation of many realistic orbits.

The most fundamental and most often used transfer is known as the Hohmann transfer. It is the most energy efficient two-impulse maneuver for transferring between two coplanar circular orbits under most circumstances. The Hohmann transfer ellipse is half of an orbit that is tangent to both circles at its apse line. The periapsis and apoapsis are the radii of the inner and outer circles, respectively. The transfer can take place in either direction, for the same total ΔV.

For the case of starting on the smaller orbit, a ΔV maneuver is required to boost the spacecraft to the transfer ellipse. The semimajor axis of this ellipse is simply $a_t = \frac{1}{2}(a_1 + a_2)$, where '1' and '2' represent the smaller and larger orbits, respectively. After coasting for 180 degrees towards the outer orbit, another ΔV maneuver is applied to boost the spacecraft's velocity to that of the larger circular orbit. The total ΔV required for a Hohmann transfer is given by

$$\Delta V_{Hohmann} = \sqrt{\mu}\left[\sqrt{\frac{2}{a_1} - \frac{1}{a_t}} - \sqrt{\frac{1}{a_1}}\right] + \sqrt{\mu}\left[\sqrt{\frac{1}{a_2}} - \sqrt{\frac{2}{a_2} - \frac{1}{a_t}}\right]. \qquad (2.6)$$

If the ratio between the outer radius and the inner radius is greater than 11.94, it may be more efficient to use what is known as the bi-elliptic transfer. This transfer uses two coaxial semi-ellipses which extend beyond the outer target orbit. Each of

the ellipses is tangent to one of the circular orbits and they are tangent to each other at the apoapsis of both. The reasoning is that the ΔV that takes place very far from the central body will be very small due to the decreased potential. In fact, as the apoapsis approaches infinity the ΔV goes to zero in what is known as a bi-parabolic transfer. These are not practical as they require an infinite amount of time. The total ΔV required for a bi-elliptical transfer is given by

$$\Delta V_{bi-elliptic} = \sqrt{\frac{\mu}{a_1}}\left[\sqrt{\frac{2(\alpha+\beta)}{\alpha\beta}} - \frac{1+\sqrt{\alpha}}{\sqrt{\alpha}} - (1-\beta)\sqrt{\frac{2}{\beta(1+\beta)}}\right]. \qquad (2.7)$$

where $\alpha = r_a/a_1$, $\beta = a_2/a_1$, and r_a is the location of the distant apoapsis burn. Bi-elliptic transfers are always more efficient than Hohmann transfers when α is greater than 15.58, as well as for large values of β when α is greater than 11.94.

Trajectories to the outer planetary moons often require transfers from large elliptical orbits down to the small circular orbits of a target moon. If we set one distance unit (DU) to the radius of the target orbit and make the circular velocity equal to one velocity unit (VU), we can apply this analysis generically. If we wish to apply a tangential, two-impulse transfer similar to the Hohmann, the question is now whether to apply the first ΔV at apoapsis to raise periapsis or at periapsis to lower the apoapsis. The optimal answer depends on the size and shape of the initial ellipse, as shown in Figure 2.2. For ellipses with smaller periapses, it is usually beneficial to perform the apoapsis maneuver first and vice versa for periapses nearer to the circular target orbit. Note also that magnitude of the total ΔV required is more dependent on the periapsis location than the size (i.e. energy) of the initial ellipse.

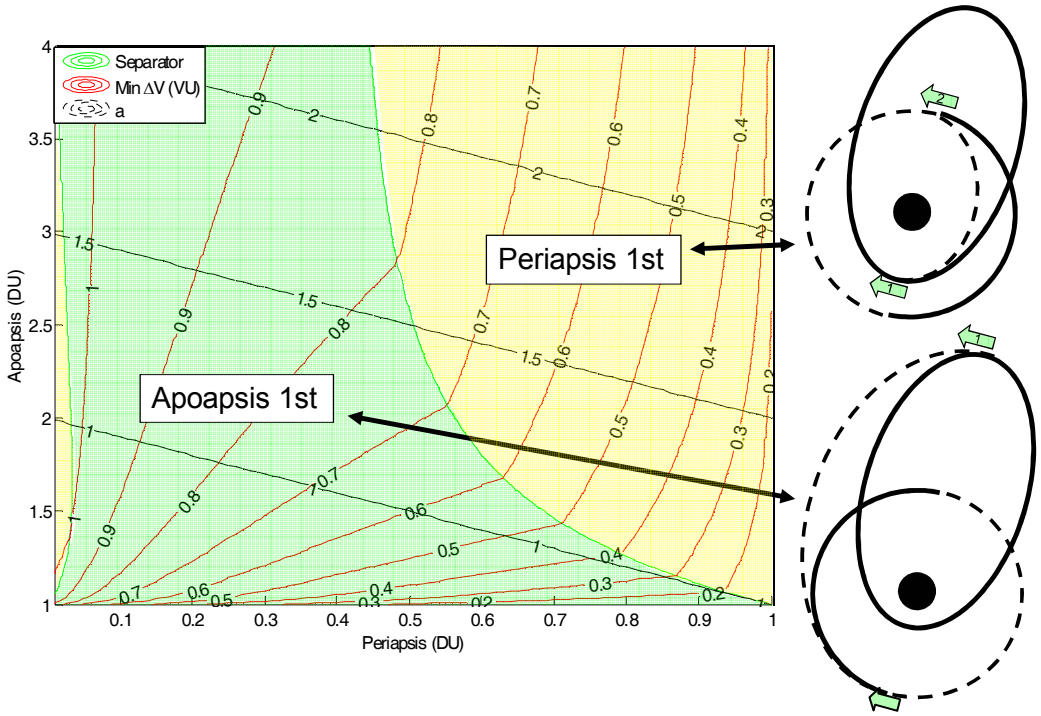

Figure 2.2. Optimal Transfer to Circular Orbit from an Elliptical. One distance unit (DU) is the radius of the target circle and one velocity unit (VU) is the circular velocity. Depending on the eccentricity of the ellipse, it may be most efficient to perform the 1st maneuver of a two-impulse transfer at either apoapsis or periapsis.

2.1.3 Lambert's Problem

According to the theorem of J. H. Lambert, the transfer time, Δt, from one point in space to another is independent of the orbit's eccentricity and depends only on the sum of the magnitudes of the position vectors, the semimajor axis, and the length of the chord connecting the points. If we are given Δt and two points, then Lambert's problem is to find the trajectory joining them. The trajectory is determined once we find the velocity vector at the first point, because the position and velocity of any point on an orbit are determined by $\boldsymbol{r}_1$ and $\boldsymbol{v}_1$. A proof of Lambert's theorem is given in Appendix C.

A primary application of Lambert's problem is that of interplanetary mission design. Known ephemeredes of the planets give the start and end positions when the launch and arrival dates are specified. Solving Lambert's problem defines the orbital elements of the desired transfer orbit. It also gives the magnitude and direction of the ΔV required to achieve the transfer and to arrive at the desired orbit. Figure 2.3 shows an example of an interplanetary Lambert transfer from Earth to Mars. With the launch and arrival dates and positions known, solving Lambert's problem yields the ΔV required to leave Earth orbit and to arrive at an orbit about Mars.

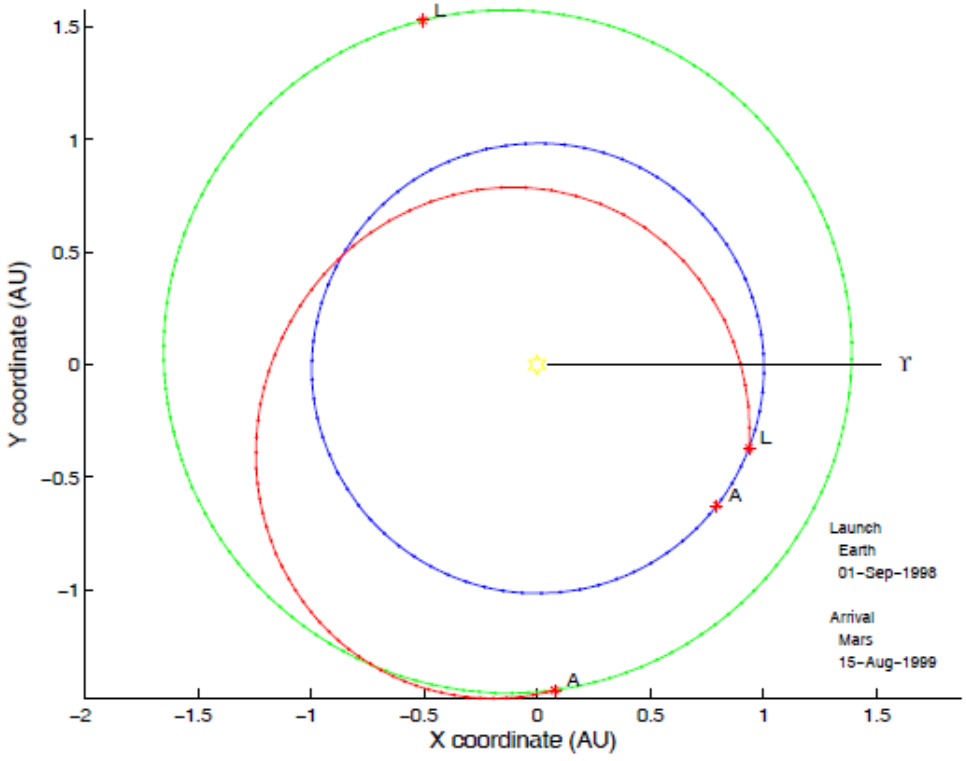

Figure 2.3. Interplanetary Lambert Transfer.

The time required for the transfer can be written

$$t - t_0 = \sqrt{\frac{a^3}{\mu}}\left[2k\pi + E - E_0 - e(\sin E - \sin E_0)\right] \tag{2.8}$$

where k is the number of complete revolutions and E is the eccentric anomaly given in radians. The subscript '$_0$' refer to values at the initial time. We now must find the correct values of a, E_0, E and e that will give the desired transfer time. With the latter three parameters given by the problem definition, it only remains to find the semimajor axis.

There are many ways to go about solving Equation 2.8 (Prussing and Conway, 1993; Schaub and Junkins, 1993), but the use of $(\Delta E)^2$ allows for well-behaved iteration and is the chosen method for the universal formulation (Battin, 1987). Such formulation allows transfers to be elliptical, parabolic, or hyperbolic without *a priori* information.

What follows is a derivation of how Lambert's problem is solved using a universal variables formulation. A similar derivation may be found in Bate, Mueller, and White (1971) and Vallado (1997). For now the $2k\pi$ term in Equation 2.8, which is used for multiple revolutions, will be omitted. (See Section 9.2 in the Appendix for a discussion of multi-revolution solutins). First we begin by defining the universal variables x and S

$$\begin{aligned} x &= \sqrt{a}\Delta E \\ S &= \frac{\Delta E - \sin \Delta E}{(\Delta E)^3} \end{aligned} \tag{2.9}$$

where $\Delta E = E - E_0$. Substituting $x^3 S$ into Equation 2.8 and rearranging yields

$$\sqrt{\mu}\Delta t = x^3 S + \sqrt{a^3}\sin \Delta E + \sqrt{a^3}\, e(\sin E - \sin E_0)\,. \tag{2.10}$$

Using the trigonometric identity

$$\sin \Delta E = \sin E \cos E_0 - \cos E \sin E_0\,. \tag{2.11}$$

and multiplying Equation 2.10 by $(1\text{-}e^2)^{1/2}(1\text{-}e\cos E_0)(1\text{-}e\cos E)$ over itself and collecting terms gives

$$\sqrt{\mu}\Delta t = x^3 S + \sqrt{a^3}\left[\frac{\sqrt{1-e^2}\sin E_0}{1-e\cos E_0}\frac{e-\cos E}{1-e\cos E} - \frac{\sqrt{1-e^2}\sin E}{1-e\cos E}\frac{e-\cos E_0}{1-e\cos E_0}\right]\Psi$$
$$\Psi = \frac{(1-e\cos E_0)(1-e\cos E)}{\sqrt{1-e^2}} \tag{2.12}$$

At this point we can use the true anomaly relationships

$$\cos\nu = \frac{e-\cos E}{e\cos E - 1} \text{ and } \sin\nu = \frac{\sqrt{1-e^2}\sin E}{1-e\cos E} \tag{2.13}$$

along with a similar trigonometric identity to Equation 2.11 and $r = a(1 - e\cos E)$ to yield

$$\sqrt{\mu}\Delta t = x^3 S + \frac{\sqrt{r_0 r}\sin\Delta\nu}{\sqrt{1-\cos\Delta\nu}}\left[\frac{\sqrt{r_0 r}\sqrt{1-\cos\Delta\nu}}{\sqrt{a(1-e^2)}}\right] = x^3 S + Ay\,. \tag{2.14}$$

where A and y have been introduced for convenience. The transfer time is now just a function of x, S, A, and y. Two new variables, $z = \Delta E^2$ and $C = (1/z)(1\text{-}\cos\Delta E)$, allow us to write

$$\begin{aligned} x &= \sqrt{y/C} \\ S &= \frac{\sqrt{z} - \sin\sqrt{z}}{z^{3/2}} \\ y &= r_0 + r + \frac{A(zS-1)}{\sqrt{C}} \\ A &= \sqrt{r_0 r(1+\cos\Delta\nu)} \end{aligned}\,. \tag{2.15}$$

where A is positive for $\Delta\nu < \pi$ and negative for $\Delta\nu > \pi$.

With $\boldsymbol{r}_0$ and $\boldsymbol{r}$ given, all that remains is to iterate on z until the desired Δt is attained. Each iteration of z is used to update C, S, y, and x (A is not a function of z

and is only calculated once). Once the desired transfer time is achieved, $\boldsymbol{v}_0$ and $\boldsymbol{v}$ can be found by using the *f* and *g* functions

$$\vec{v}_0 = \frac{\vec{r} - f\vec{r}_0}{g} \text{ and } \vec{v} = \frac{\dot{g}\vec{r} - \vec{r}_0}{g} \tag{2.16}$$

where

$$f = 1 - \frac{y}{r_0}, \quad \dot{g} = 1 - \frac{y}{r} \text{ and } g = A\sqrt{\frac{y}{\mu}}. \tag{2.17}$$

2.1.4 The Dynamics of a Gravity-Assist Flyby

Before considering interplanetary trajectories, a basic understanding of the dynamics of a hyperbolic passage, or flyby, is required. Figure 2.4 shows the trajectory of a typical hyperbolic trajectory. Let us consider a spacecraft approaching a planetary body which we will designate the "gravity-assist" body and denote with a subscript '*ga*'. The spacecraft has a relative velocity of $\boldsymbol{V}_{\infty,\text{in}}$ at a great distance ($r \sim \infty$). We now define r_p to be the radial distance of closest approach, ν_∞ to be the true anomaly of the asymptotes, and δ to be the turn angle of $\boldsymbol{V}_\infty$.

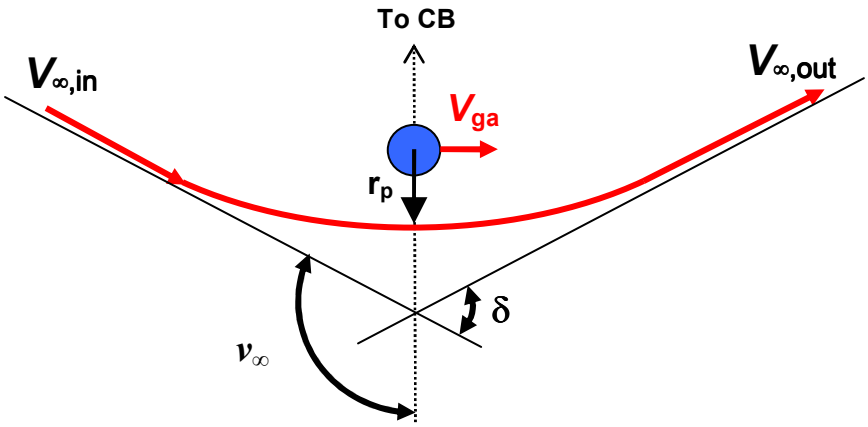

Figure 2.4. Geometry of a Hyperbolic Passage. V_{ga} is th velocity vector of the gravity-assist body. The V_∞ vector of the spacecraft has a true anomaly at infinity of $\boldsymbol{\nu}_\infty$. The point of closest approach is designated r_p. The V_∞ vector is bent by an the turn angle, δ. Subscript 'in' represents conditions before the fly-by, 'out' subscripts are after the fly-by.

For a hyperbola, $e > 1$ and $a < 0$ to maintain the energy equation $E = -\mu/2a$. Thus, energy is positive and constant. We also note that

$$E = -\frac{\mu}{2a} = \frac{V^2}{2} - \frac{\mu}{r} = \frac{V_\infty^2}{2}. \tag{2.18}$$

Therefore, the magnitude of $\boldsymbol{V}_\infty$ is the same on the inbound and outbound legs. The parameters e, δ, and ν_∞ can be found by using the equation for a conic section in Equation 2.3. Since ν_∞ occurs when $r \rightarrow \infty$, we can write

$$\nu_\infty = \cos^{-1}\left(\frac{-1}{e}\right). \tag{2.19}$$

From inspection of Figure 2.4

$$\nu_\infty = \frac{\pi}{2} + \frac{\delta}{2}. \tag{2.20}$$

Equating 2.19 and 2.20 yields

$$\frac{1}{e} = \sin\frac{\delta}{2}. \tag{2.21}$$

From the energy relation in Equation 2.18, the semimajor axis of the hyperbola is given by $a = -\mu/V_\infty^2$. Substituting this into Equation 2.3 gives us an equation for the eccentricity

$$e = 1 + \frac{r_p V_\infty^2}{\mu}. \tag{2.22}$$

The amount of bending, or turn angle, gained by a flyby is governed by the mass of the gravity-assist body, μ, the magnitude of V_∞, and the closest approach, r_p:

$$\delta = 2\sin^{-1}\left(\frac{\mu}{\mu + r_p V_\infty^{\ 2}}\right). \tag{2.23}$$

The discussion thus far has dealt with quantities in the inertial frame centered on the gravity-assist body. However, the assist body has a velocity of its own in an overall inertial frame centered on a central body. The hyperbolic excess velocity with respect to the gravity-assist body, or the V_∞ vector, is in fact defined as the velocity of the spacecraft with respect to the central body, V_{sc}, minus the velocity of the gravity-assist body, V_{ga}:

$$\vec{V}_\infty = \vec{V}_{sc} - \vec{V}_{ga}. \tag{2.24}$$

This relationship is best described by the velocity triangle in Figure 2.5. If the gravity-assist body is in a circular orbit, as is the assumed case for this dissertation, then the angle between V_{sc} and V_{ga} is the flight path angle, γ. The direction of the V_∞ vector is defined by the angle α, which is the angle between V_∞ and V_{ga} and varies from 0° (parallel) and 180° (anti-parallel). This is known as the "pump" angle (Uphoff, 1976), as changing α changes the orbital energy directly.

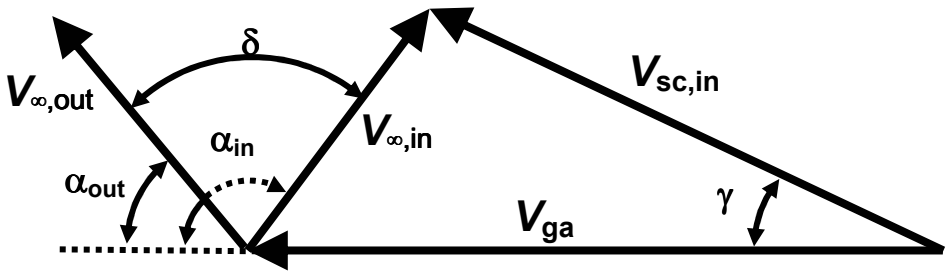

Figure 2.5. Geometry of a fly-by. V_{ga} and V_{sc} are the velocity vectors of the gravity-assist body and spacecraft, respectively. The V_∞ vector is the difference between the two. Subscript 'in' represents conditions before the fly-by, 'out' subscripts are after the fly-by. In coplanar orbits, the "pump" angle, α ,is changed by the turn angle, δ. The flight path angle, γ, is the angle between V_{ga} and V_{sc}.

The V_∞ vector is constant in the absence of perturbations and can be turned via close fly-bys of the gravity-assist body up to some maximum turn angle. This maximum occurs when r_p is minimized. If we define V_c to be the local circular velocity at the point of closest permissible approach to the gravity-assist body[9] given by

$$V_c = \sqrt{\frac{\mu}{r_{p,\min}}}. \tag{2.25}$$

If we substitute the expression for V_c into Equation 2.23 we have

$$\delta_{\max} = 2\sin^{-1}\left(\frac{V_c^2}{V_c^2 + V_\infty^2}\right). \tag{2.26}$$

The quantity V_c is very useful in quantifying the bending power of a celestial body and in assessing the difficulty of orbital capture. Table 3.1 on page 65 lists normalized V_c values for a few moons of interest.

[9] Typically the minimum flyby distance will be ~100 km above the body's surface if there is no atmosphere. For a dense atmosphere such as Titan it may be 300-500 km

The outgoing direction after a flyby can be controlled by fine tuning the approach condition via small orbital maneuvers. This is known as B-plane targeting. Typically these maneuvers only require a few m/s of ΔV or less. The new V_∞ vector also leads to a new V_{sc} vector that may be longer or shorter than prior to the flyby. This means that the orbital parameters and energy with respect to the central body can be modified to suit mission needs for a negligible cost in fuel. For this reason flybys are often called gravity-assists. The boost gained by a gravity assist is given by

$$\Delta V_{fb} = 2V_\infty \sin\left(\frac{\delta}{2}\right). \tag{2.27}$$

The realm of possible orbital parameters following a flyby can be plotted on a map called a V_∞ *Sphere*, as described in Section 3.4.

Orbital Capture. Many scientific missions end with an orbit about a target planet or moon. This can be achieved by reducing energy during hyperbolic passage. The simplest method of establishing a circular orbit with one decelerating impulse is to adjust the approach parameters such that the distance of closest approach is equal to the final orbit radius, r_c. When this point is reached an orbital insertion maneuver is performed to slow the spacecraft. The size of the maneuver is given by

$$\Delta V = \sqrt{V_\infty^2 + \frac{2\mu}{r_c}} - \sqrt{\frac{\mu}{r_c}}. \tag{2.28}$$

This maneuver may be optimized when the final orbit radius is not critical. To minimize ΔV, we take the derivative of Equation 2.28 with respect to r_c and set it equal to zero, noting that V_∞ is constant

$$\frac{\partial \Delta V}{\partial r_c} = \frac{-\mu / r_c^2}{\sqrt{V_\infty^2 + \frac{2\mu}{r_c}}} + \frac{1}{2}\sqrt{\frac{\mu}{r_c^3}} = 0 . \tag{2.29}$$

This indicates that the minimum ΔV occurs when

$$r_c = \frac{2\mu}{V_\infty^2} \tag{2.30}$$

and has the value

$$\Delta V_{\min} = \frac{V_\infty}{\sqrt{2}} . \tag{2.31}$$

2.1.5 Patched Two-Body Trajectories

The patched two-body approximation is a method to simplify trajectory calculations for spacecraft in a multiple body environment. The simplification is achieved by dividing space into various parts by assigning each of the n bodies (e.g. the Sun, planets, moons) its own sphere of influence. When the spacecraft is within the sphere of influence of a smaller body, only the gravitational force between the spacecraft and that smaller body is considered, otherwise the gravitational force between the spacecraft and the larger body is used. This reduces an unsolvable n-body problem to multiple solvable two-body problems, for which the solutions are the well-known conic sections of the Keplerian orbits. This method gives a good approximation of trajectories for interplanetary spacecraft missions.

Defining the sphere of influence (SOI) of the smaller body is not as simple as calculating the location where its gravitational pull is stronger than that of the larger. If this were the case, then the moon would fall 50% outside of the Earth's SOI, which is obviously not true. The correct definition of SOI, due to Laplace, involves

considering the spacecraft to be in orbit about one body and calculating the perturbing force due to the other body. This allows us to determine the ratio of the disturbing acceleration to the central body attraction. The resulting analysis yields the approximate radius of the SOI

$$r_{SOI} = \left(\frac{m_2}{m_1} \right)^{2/5} R , \tag{2.32}$$

where R is the distance between the two bodies and $m_1 >> m_2$.

The SOI is both very large and extremely small, depending on your frame of reverence. Relative to the size of m_2 it is so large so as to consider it at infinity. Relative to m_1, it is essentially a point and of little consequence. Because it is so large in the first case, the velocity relative to m_2 exiting the SOI on an escape hyperbola is considered to be the V_∞ vector. This vector is then added to the smaller body's orbital velocity to obtain the spacecraft's velocity with respect to the larger body. This velocity, along with the position upon exiting the SOI, determines the Keplerian orbit about m_1 until the SOI of a smaller body is again entered.

As a simplification due to the smallness of the SOI in the larger reference frame, the effects of a flyby can be considered to be instantaneous and occur exactly at the location of the smaller body. This is called a *zero sphere-of-influence* method of patched conics. This eliminates the need to calculate the actual location of the SOI boundary crossing and convert to the new reference frame. We can also assume that the B-plane targeting that controls the turn angle, δ, is negligible and occurs automatically to meet the mission design's needs. This method is used in the analysis of V_∞ leveraging in Chapter 3.

2.2 The Three-Body Problem

In this section the equations governing the PR3BP and planar Hill's Problem are set forth. Using consistent notation and quantities it is possible to show their equivalences under specified assumptions. Writing the 3BP Jacobi integral in an inertial coordinate system permits a derivation of Tisserand's criterion and also allows a relationship with 2BP orbital parameters and quantities, specifically V_{∞}.

2.2.1 Planar Circular Restricted Three-Body Problem

The primary body, m_1, and the secondary body, m_2, are assumed to be in circular orbits relative to each other and their center of mass, or barycenter, as illustrated in Figure 2.6. They are separated by a distance R. The coordinate frame, X-Y, rotates with constant angular velocity, ω, given by

$$\omega = \sqrt{\frac{\mu_1 + \mu_2}{R^3}}, \tag{2.33}$$

where $\mu_{1(or2)} = Gm_{1(or2)}$ and G is the gravitational constant. A massless third body, m_3, is located at

$$r = \sqrt{X^2 + Y^2} \tag{2.34}$$

$$\begin{aligned} r_1 &= \sqrt{(X + R_1)^2 + Y^2} \\ r_2 &= \sqrt{(X - R_2)^2 + Y^2} \end{aligned} \tag{2.35}$$

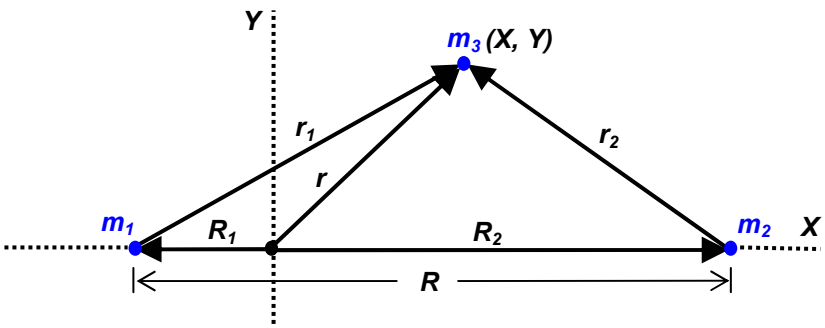

Figure 2.6. Problem setup for the PR3BP. Two massive bodies, where $m_1 > m_2$, are separated by a distance R. The coordinate frame rotates with angular velocity ω about their barycenter. A small third body, m_3, moves in their vicinity.

In this dissertation we will use capital letters to represent dimensional[10] coordinates and lower case to represent normalized coordinates. The augmented effective gravitational potential of the 3BP is given by

$$U = \frac{\mu_1}{r_1} + \frac{\mu_2}{r_2} + \frac{1}{2}\omega^2(X^2 + Y^2), \tag{2.36}$$

where the third term accounts for the effects of a rotating coordinate frame. Since total energy is classically given by the kinetic energy minus the potential, we can write an equation for the three-body energy as

$$E_{3b} = \frac{V^2}{2} - U, \tag{2.37}$$

where V is the velocity of the third body in the rotating frame given by

$$V = \sqrt{\dot{X}^2 + \dot{Y}^2}. \tag{2.38}$$

[10] SI units

2.2.2 Equations of Motion and Normalization

To scale the equations to any system, we introduce the mass parameter, μ, given by

$$\mu = \frac{\mu_2}{\mu_1 + \mu_2} << 1. \tag{2.39}$$

We also set $R = 1$, $m_1 + m_2 = 1$, and $\omega = 1$. This gives us $R_1 = \mu$, $R_2 = 1-\mu$, and the orbital period $P = 2\pi/\omega = 2\pi$. We can now write the equations of motion

$$\begin{aligned} \ddot{x} &= 2\dot{y} + x - (1-\mu)\frac{x+\mu}{r_1^3} - \mu\frac{x-1+\mu}{r_2^3} \\ \ddot{y} &= -2\dot{x} + y - (1-\mu)\frac{y}{r_1^3} - \mu\frac{y}{r_2^3} \end{aligned} \tag{2.40}$$

where

$$\begin{aligned} r_1 &= \sqrt{(x+\mu)^2 + y^2} \\ r_2 &= \sqrt{(x-1+\mu)^2 + y^2} \end{aligned} \tag{2.41}$$

in normalized units. Last, the energy and Jacobi in nondimensional units can no be written:

$$E_3 = \frac{1}{2}(\dot{x}^2 + \dot{y}^2) - \frac{1}{2}(x^2 + y^2) - \frac{1-\mu}{r_1} - \frac{\mu}{r_2} \tag{2.42}$$

$$J_3 = x^2 + y^2 + \frac{2(1-\mu)}{r_1} + \frac{2\mu}{r_2} - \dot{x}^2 - \dot{y}^2 \tag{2.43}$$

where the subscript '3' has been used to designate the non-dimensional form. For orbits that are very close to m_2, normalized energy, E_3, is usually around -1.5 and J_3 is around 3. In order to readily convert between the dimensional and nondimensional forms of the Jacobi, we can use the relation

$$J_{3b} = J_3 (R\omega)^2 = J_3 \left(\frac{\mu_1 + \mu_2}{R} \right). \tag{2.44}$$

2.2.3 Jacobi Constant

The energy in this approximation is constant and is an integral of motion. Indeed, the expression given by Equation 2.37 is called the Jacobi constant in some instances in the literature. However, the most common form of the Jacobi has a -2 multiplier and is given by

$$J_{3b} = -2E_{3b} = 2U - V^2 = \omega^2 (X^2 + Y^2) + \frac{2\mu_1}{r_1} + \frac{2\mu_2}{r_2} - \dot{X}^2 - \dot{Y}^2, \tag{2.45}$$

where the subscript '3b' is used to represent dimensional units.

2.2.4 Hill's Problem

Hill's problem is a special case of the restricted 3BP (Hill, 1878). In this case μ tends towards zero and the distance to m_1 goes to infinity. It is appropriate for spacecraft orbits near the secondary and where $\mu_1 >> \mu_2$.

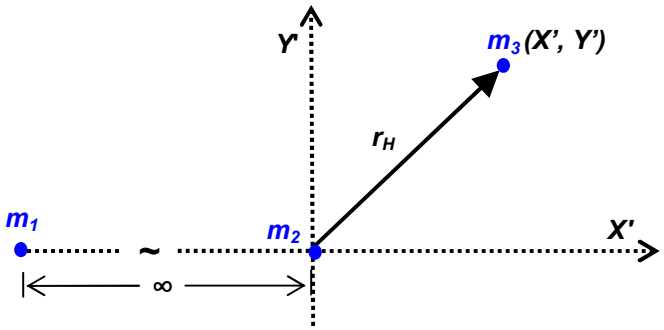

Figure 2.7. Formulation of Hill's Problem. The rotating coordinate frame is centered at the secondary, m_2, with the primary acting as a perturbing body at negative infinity.

Formulation of Hill's problem differs from the PR3BP in that the center of the rotating coordinate system, X'-Y', is now at m_2 and in that m_1 is at negative infinity on the X' axis and acts as a perturbing body only (Figure 2.7). Often the notation found in the literature is somewhat variable, but as much of the notation from the PR3BP as possible will be retained here so as to keep the quantities comparable.

The angular velocity, ω, is the same as is given by Equation 2.33, but occasionally it will be given without μ_2 because it is assumed to be small compared to μ_1. The coordinate transformation between X-Y and X'-Y' is simply

$$\begin{bmatrix} X' \\ Y' \end{bmatrix} = \begin{bmatrix} X \\ Y \end{bmatrix} - \begin{bmatrix} R_2 \\ 0 \end{bmatrix} \tag{2.46}$$

which gives

$$r_H = r_2 = \sqrt{(X - R_2)^2 + Y^2} = \sqrt{X'^2 + Y'^2}\,. \tag{2.47}$$

Velocity in the Hill frame is equivalent to the PR3BP. We can now give the equations of motion in dimensional units

$$\ddot{X}' = 2\omega\dot{Y}' - \frac{\mu_2}{r_H^3}X' + 3\omega^2 X'$$
$$\ddot{Y}' = -2\omega\dot{X}' - \frac{\mu_2}{r_H^3}Y' \tag{2.48}$$

Often the 'μ_2' in the above equations is simply denoted 'μ', which is not to be confused with the reduced mass of the 3BP. Note that setting $\omega = 0$ in the equations above reduces them to the equations of motion of the 2BP.

The Jacobi integral in Hill's problem is most commonly given by

$$J_{H,d} = \frac{V^2}{2} - \frac{\mu_2}{r_H} - \frac{3}{2}\omega^2 X'^2. \tag{2.49}$$

Here, 'H,*d*' in the subscripts denotes the dimensional nature of the quantity. A lone 'H' will be used when referring to the normalized value. Note once again that setting $\omega = 0$ yields the equation for energy in the two-body problem.

Hill Normalization

Normalization in Hill's problem is different from that of the PR3BP. Here the length unit is not the separation between the primaries but is given by[11]

$$l = \left(\frac{\mu_2}{\omega^2}\right)^{1/3}. \tag{2.50}$$

The unit of time is given by $\tau = 1/\omega$. Using Equation 2.50 to normalize the distance between m_2 and m_3, the realm of accuracy of Hill's approximation is given by

$$r_H < \left(\frac{m_2 + m_3}{m_1}\right)^{1/3}. \tag{2.51}$$

These scale factors allow us to write the nondimensional equations of motion

[11] *l* is approximately 1.5 times the distance to L1 or L2 and represents the radius of the Hill sphere.

$$\ddot{x}' = 2\dot{y}' - \frac{x'}{r_H^3} + 3x'$$
$$\ddot{y}' = -2\dot{x}' - \frac{y'}{r_H^3} \tag{2.52}$$

where x', y', and r_H are normalized by dividing by the length unit in Equation 2.50. The normalized Jacobi in Hill's approximation is given by

$$J_H = \frac{V^2}{2} - \frac{1}{r_H} - \frac{3}{2}x'^2 . \tag{2.53}$$

This most common form of the Jacobi, unlike the three-body formulation, is similar to the two-body energy (kinetic minus potential) and does not contain the '-2' multiplier. In his series on numerical exploration of the restricted problem, Hénon (1969) uses the designation Γ as the integral of motion in Hill's problem:

$$\Gamma = 3x'^2 + \frac{2}{r_H} - \dot{x}'^2 - \dot{y}'^2 , \tag{2.54}$$

which is given here using our notation. When compared to Equation 2.53, it can be seen that $\Gamma = -2J_H$, which is analogous to the relationship between energy and Jacobi in the 3BP.

We can readily convert between the dimensional and nondimensional forms of the Jacobi by using the relationships

$$J_{H,d} = J_H (l\omega)^2 = J_H (\mu_2 \omega)^{2/3} . \tag{2.55}$$

2.2.5 The Jacobi Integral – PR3BP vs. Hill's

Since velocity is equivalent in both reference frames, we start with Equation 2.45 plus 2 times Equation 2.49 to get

$$J_{3b} + 2J_{H,d} = 2\frac{\mu_2}{r_H} - 2\frac{\mu_2}{r_2} + 2\frac{\mu_1}{r_1} + \omega^2\left[(X^2 + Y^2) - 3X'^2\right]. \tag{2.56}$$

Next we institute the Hill's problem assumptions by presuming that the spacecraft is close to the secondary and $R_2 >> R_1$. These assumptions yield $r_1 \cong R$ and $r_H = r_2$. Substituting these relationships into Equation 2.56, we have

$$J_{3b} + 2J_{H,d} = 2\frac{\mu_1}{R} + \omega^2\left[R^2 - 3X'^2\right]. \tag{2.57}$$

Using Equation 2.33 in Equation 2.57 we get

$$J_{3b} + 2J_{H,d} = 2\frac{\mu_1}{R} + (\mu_1 + \mu_2)\left[\frac{R^2}{R^3} - \frac{3X'^2}{R^3}\right]. \tag{2.58}$$

Assuming $\mu_1 + \mu_2 \cong \mu_1$ and $X'^2 << R^3$ we have

$$J_{3b} + 2J_{H,d} \cong 2\frac{\mu_1}{R} + \frac{\mu_1}{R} = 3\frac{\mu_1}{R} \quad \rightarrow \quad J_{3b} \cong 3\frac{\mu_1}{R} - 2J_{H,d}, \tag{2.59}$$

which is the relationship between the Jacobi constants in the two problems. Note that μ_1/R is the circular velocity of m_2 squared.

If we use the scaling factors in Equations 2.44 and 2.55, we can write the nondimensional relationship as

$$J_3 \cong 3 - 3\mu - 2J_H\mu^{2/3} \tag{2.60}$$

where the reduced mass, μ, is used.

2.2.6 Propagating Orbits and the State Transition Matrix

Like any system of nonlinear differential equations, the generation of trajectories in the 3BP requires numerical integration. For a given set of initial conditions, $\boldsymbol{r_0}$ and $\boldsymbol{v_0}$, a trajectory is obtained by numerically integrating four first-order scalar differential equations derived from Equation 2.40:

$$\begin{aligned}
\dot{x} &= v_x \\
\dot{y} &= v_y \\
\dot{v}_x &= 2v_y + x - (1-\mu)\frac{x+\mu}{r_1^3} - \mu\frac{x-1+\mu}{r_2^3} \\
\dot{v}_y &= -2v_x + y - (1-\mu)\frac{y}{r_1^3} - \mu\frac{y}{r_2^3}
\end{aligned} \tag{2.61}$$

where r_1 and r_2 are given by Equation 2.41.

From differential equation theory, any State Transition Matrix (STM or Φ) defines, given the initial conditions, the solution to a set of linear differential equations of the form

$$\dot{\vec{s}} = A(t)\vec{s} \tag{2.62}$$

where $\boldsymbol{s}$ is the state vector $\boldsymbol{s} = [x\ y\ \dot{x}\ \dot{y}\ ]^{\mathrm{T}}$ and A is a matrix that is a function of time. The solution to this equation is

$$\vec{s}(t) = \Phi(t, t_0)\vec{s}(t_0) \tag{2.63}$$

where the STM, Φ, is the solution to the matrix differential equation

$$\dot{\Phi}(t, t_0) = A(t)\Phi(t, t_0). \tag{2.64}$$

A Taylor series expansion of the 3BP equations of motion (Equation 2.40) yields variational equations that can be integrated to find the STM. This linearization determines and equation that governs how a small difference from a given solution will behave. The solution to this variational equation is in the form of Equation 2.63, but with $\boldsymbol{s}(t)$ replaced with $\delta\boldsymbol{s}(t)$.

While special cases occur where the STM can be found analytically, it is typically found numerically using Equation 2.64, where the matrix $A(t)$ is equal to

$$A(t) = \frac{\partial\dot{\vec{s}}(t)}{\partial\vec{s}(t)}. \tag{2.65}$$

In the PCR3BP, A(t) is equal to

$$A(t) = \begin{bmatrix} 0 & I \\ U_{xx} & 2\Omega \end{bmatrix}, \tag{2.66}$$

where

$$U_{xx} = \begin{bmatrix} \frac{\partial \ddot{x}}{\partial x} & \frac{\partial \ddot{x}}{\partial y} \\ \frac{\partial \ddot{y}}{\partial x} & \frac{\partial \ddot{y}}{\partial y} \end{bmatrix} \quad \text{and} \quad \Omega = \begin{bmatrix} 0 & 1 \\ -1 & 0 \end{bmatrix}. \tag{2.67}$$

2.2.7 Stability and the Monodromy Matrix

The STM from the initial time (t_0) to the time after one period ($t_0 + P$) is referred to as the monodromy matrix. After being propagated for one full orbit, the matrix contains information about every region that a spacecraft would pass through along that orbit. The stability of a periodic orbit may be determined by analyzing the eigenvalues of the orbit's monodromy matrix. A random perturbation in the state of a spacecraft on an unstable orbit will cause the particle's state to exponentially diverge from that of the original orbit over time.

The monodromy matrices of periodic orbits in the PCR3BP have four eigenvalues: λ, $1/\lambda$, 1, and 1. The fact that these eigenvalues occur in reciprocal pairs is a consequence of the symplectic nature of the STM, while the pair of values equal to one is a result of Jacobi integral of motion. The stability of an orbit is related to the absolute value of the real component of each eigenvalues. If a value exists that is greater than 1, this indicates that an orbit is unstable to perturbations along the corresponding eigenvector. If the value is less than 1 then an orbit is considered to be

stable in that direction. In fact, the eigenvalues of Keplerian orbits are all equal to 1, indicating that any perturbation neither grows nor decays.

The instability of periodic orbits indicates that both stable and unstable manifolds exist, which lead to and leave from them, respectively. These manifolds contain the set of all trajectories that a spacecraft may take if it is perturbed in the direction of the orbit's unstable eigenvector. They are invariant, meaning that a point on the manifold will remain on the manifold as time evolves. Periodic orbits can be useful as capture mechanisms as a spacecraft can arrive nearly ballistically on an stable manifold, and then depart after a time on a stable manifold towards a lower orbit.

2.2.8 The Single-Shooting Method

The search for periodic orbits in the 3BP is typically an iterative process. An initial guess is propagated to some point where we check for some indicator of periodicity (usually a form of symmetry). Knowledge of the dynamics of the system allows for an educated update to the initial conditions and the process is repeated. This continues until periodicity conditions are met and a solution is found. In this section we lay out the equations for a form of differential correction known as the single-shooting method.

The basic algorithm, described by Howell (1984), is modified here for the planar case. It uses the symmetry about the *x*-axis in the CRTBP in order to search for periodic orbits. This means that if a trajectory intersects the x-axis twice with a velocity perpendicular to the x-axis, the trajectory will be periodic. In this method, a point on the x-axis with initial conditions close to the desired orbit is integrated

forward in time until it returns to the x-axis. The requirement that the intersection with the x-axis be perpendicular (i.e. $\dot{x} = 0$) imposes constraints that can be used to modify the initial conditions. This process is repeated until a periodic orbit within the desired tolerances is obtained. Howell found that if $|\dot{x}| < 10^{-8}$, then the orbit can be considered periodic.

The initial state has the form $[x_0 \ 0 \ 0 \ \dot{y}_0]^T$. After this state has been propagated for half the period, a state of $\boldsymbol{s}(P/2) = [x \ 0 \ 0 \ \dot{y}]^T$ will indicate a periodic orbit of period P. Since the initial guess rarely results in a subsequent perpendicular crossing, an algorithm must be developed to calculate the updates needed to the find the correct initial conditions. The initial state and the state at P/2 is related by

$$\begin{bmatrix} \delta x \\ \delta y \\ \delta \dot{x} \\ \delta \dot{y} \end{bmatrix} = \begin{bmatrix} \phi_{11} & \phi_{12} & \phi_{13} & \phi_{14} \\ \phi_{21} & \phi_{22} & \phi_{23} & \phi_{24} \\ \phi_{31} & \phi_{32} & \phi_{33} & \phi_{34} \\ \phi_{41} & \phi_{42} & \phi_{43} & \phi_{44} \end{bmatrix} \begin{bmatrix} \delta x_0 \\ \delta y_0 \\ \delta \dot{x}_0 \\ \delta \dot{y}_0 \end{bmatrix} + \begin{bmatrix} x \\ y \\ \dot{x} \\ \dot{y} \end{bmatrix} \delta(P/2) \tag{2.68}$$

where φ_{ij} are components of the STM. We can now use the fact that $\delta y_0 = \delta \dot{x}_0 = 0$ to find the δy component

$$\delta y = \phi_{21} \delta x_0 + \phi_{24} \delta \dot{y}_0 + \dot{y} \delta(P/2) . \tag{2.69}$$

Fixing x_0, we can find the updated to $\dot{y}_0$ from $\dot{x}$ by the equation

$$\delta \dot{y}_0 = \left[\phi_{34} - \frac{\ddot{x}}{\dot{y}} \phi_{24} \right]^{-1} \dot{x} . \tag{2.70}$$

The process is iterated until $\dot{y}_0$ yields a perpendicular crossing (within desired tolerance).

2.2.9 The Inertial Frame and Tisserand's Invariant

The state of a spacecraft in the rotating frame is given by $S_r = [X\ Y\ \dot{X}\ \dot{Y}]^T$. To transform the state from the rotational (or synodic) frame, to the inertial (or sidereal) frame we must take into account the rotational offset, θ, and the angular rate, $\omega = \dot{\theta}$. Here we will assume the offset is zero (see Anderson (2005) for non-zero θ transformations). Since the Z axes are aligned in both frames, we can write

$$S_i = \begin{bmatrix} X_i \\ Y_i \\ \dot{X}_i \\ \dot{Y}_i \end{bmatrix} = \begin{bmatrix} X \\ Y \\ \dot{X} - \omega Y \\ \dot{Y} + \omega X \end{bmatrix} \quad \text{and} \quad S_r = \begin{bmatrix} X_i \\ Y_i \\ \dot{X}_i + \omega Y_i \\ \dot{Y}_i - \omega X_i \end{bmatrix} \tag{2.71}$$

where the subscript 'i' denotes the inertial frame.[12] Note that ω = 1 in the nondimensional frame.

Recall that the rotating frame is centered at the barycenter of m_1 and m_2. However, most inertial frames are centered on either of the bodies. As such we must shift the state vectors to the new center.

$$S_{i,1} = \begin{bmatrix} X + R_1 \\ Y \\ \dot{X} - \omega Y \\ \dot{Y} + \omega(X + R_1) \end{bmatrix}, \quad S_{i,2} = \begin{bmatrix} X - R_2 \\ Y \\ \dot{X} - \omega Y \\ \dot{Y} + \omega(X - R_2) \end{bmatrix}$$

[12] Variables such as X and Y without a subscript are rotational quantities, where a subscript 'r' has been omitted for clarity and redundancy

and
$$s_{i,1} = \begin{bmatrix} x+\mu \\ y \\ \dot{x}-y \\ \dot{y}+x+\mu \end{bmatrix}, \quad s_{i,2} = \begin{bmatrix} x-(1-\mu) \\ y \\ \dot{x}-y \\ \dot{y}+x-(1-\mu) \end{bmatrix} \tag{2.72}$$

where states with the added subscript '1' refer to states centered at the primary and states with subscript '2' are centered at the secondary.

Applying the transformation in Equation 2.72 to Equation 2.45 gives the Jacobi in inertial coordinates

$$J_{3b,i} = \omega^2 (X_i^{\,2} + Y_i^{\,2}) + \frac{2\mu_1}{r_1} + \frac{2\mu_2}{r_2} - (\dot{X}_i + \omega Y_i)^2 - (\dot{Y}_i - \omega X_i)^2 . \tag{2.73}$$

Rearranging and canceling like terms we get

$$J_{3b,i} = -\left[\dot{X}_i^{\,2} + \dot{Y}_i^{\,2}\right] + \left[\frac{2\mu_1}{r_1} + \frac{2\mu_2}{r_2}\right] + 2\omega(X_i\dot{Y}_i - \dot{X}_i Y_i) . \tag{2.74}$$

The first term is the velocity squared in the inertial frame, the second is twice the gravitational potential from either body, and the third is 2ω times the *Z*-component of the angular momentum. We can apply the *vis-viva* equation,

$$V_i^{\,2} = \frac{2\mu_1}{r_1} - \frac{\mu_1}{a_d} , \tag{2.75}$$

where *'a_d'* is the dimensional semimajor axis of the spacecraft, to the first term. Also, the equation for angular momentum (in the plane),

$$(X_i\dot{Y}_i - \dot{X}_i Y_i) = h = \sqrt{\mu_1 p} = \sqrt{\mu_1 a_d (1-e^2)} \tag{2.76}$$

where *p* is the semi-parameter and *e* is the eccentricity, can be applied to the third term. If it is assumed that the spacecraft is far from the secondary so that two-body dynamics dominate, we can let $r_1 = r$ and $\mu_2 \rightarrow 0$. These assumptions allow us to write

$$T_d = J_{3b,i} = \frac{\mu_1}{a_d} + 2\omega\sqrt{\mu_1 a_d (1-e^2)}\,, \tag{2.77}$$

where T_d is Tisserand's parameter (or invariant) in dimensional units, which is an approximation of the Jacobi using two-body parameters. Normalizing using Equation 2.44 we have

$$\begin{aligned} T = J_{3,i} &= \frac{(1-\mu)}{a} + 2\sqrt{(1-\mu)a(1-e^2)} \\ T &\cong \frac{1}{a} + 2\sqrt{a(1-e^2)} \end{aligned} \tag{2.78}$$

where $a = a_d/R$ and $\mu \rightarrow 0$.

Nineteenth century astronomer Francois Felix Tisserand (1896) used this application of the Jacobi integral as a criterion to identify comets. If this function is computed for two comet observations on different orbits and the results are the same, it can be concluded that the observations are of the same comet that was perturbed by a planet.

2.2.10 Normalization Parameters

As it has been shown above, it is possible to normalize a system's parameters such that the results can be applied generally to all systems that can be approximated under the same assumptions. We have outline two normalization procedures: one for the 3BP and one for Hill's problem. Both use a time unit (TU) of $1/\omega$ which is equivalent to the period (P) of the secondary divided by 2π. The two approximations differ, however, in length units (LU). The 3BP uses the semimajor axis of the secondary, whereas Hill's problem uses a derived length, l, given by Equation 2.50, which represents the radius of the Hill Sphere and is roughly 1.5 times the distance to

the first two libration points. The velocity units (VU) are then given by LU/TU for each case.

Table 2.1 below lists the normalization parameters for a few selected moons in the solar system. The table lists the gravitational parameter (μ_2), period, angular velocity, time unit, length units for each approximation, velocity units for each approximation, the reduced mass (μ), and normalized radii in each approximation. The last two columns are used to determine which orbits impact the body in a normalized system.

Table 2.1. Normalization Parameters for a Few Moons.

Body	GM (km^3/s^2)	Period (days)	ω (s^{-1})	Radius (km)	TU (days)	LU-3BP (10^5 km)	LU-Hill (km)	VU-3BP (km/s)	VU-Hill (m/s)	μ	Radius (3BP)	Radius (Hill's)
Titan	8978	15.95	4.56E-06	2575.5	2.54	12.22	75576	5.57	345	2.37E-04	0.0021	0.034
Io	5960	1.77	4.11E-05	1821.6	0.28	4.22	15227	17.33	626	4.70E-05	0.0043	0.120
Europa	3203	3.55	2.05E-05	1560.8	0.57	6.71	19696	13.74	403	2.53E-05	0.0023	0.079
Ganymede	9888	7.15	1.02E-05	2631.2	1.14	10.70	45743	10.88	465	7.80E-05	0.0025	0.058
Callisto	7179	16.69	4.36E-06	2410.3	2.66	18.83	72314	8.20	315	5.67E-05	0.0013	0.033
Enceladus	7	1.37	5.30E-05	252.1	0.22	2.38	1368	12.62	73	1.90E-07	0.0011	0.184
Rhea	154	4.52	1.61E-05	764.3	0.72	5.27	8407	8.48	135	4.06E-06	0.0015	0.091
Triton	1428	5.88	1.24E-05	1353.0	0.94	3.55	21047	4.39	260	2.09E-04	0.0038	0.064
Moon	4903	27.32	2.67E-06	1737.5	4.34	3.84	88372	1.02	236	1.22E-02	0.0045	0.020

2.3 Relationships between the Two- and Three-Body Problems

The formulation of Tisserand's parameter gives us a bridge between the two- and three-body problems. Just as the Jacobi does not change during a flyby of the secondary, likewise the magnitude of the hyperbolic excess velocity, V_∞, is unchanged by a flyby in the two-body problem.

If we apply the law of cosines to the triangle in Figure 2.5 we get

$$V_\infty^2 = V_{sc}^2 + V_{ga}^2 - 2V_{ga}V_{sc}\cos\gamma\,. \tag{2.79}$$

Next, we substitute the two-body relationships

$$\cos\gamma = \frac{h}{rV_{sc}}, \qquad V_{sc} = \sqrt{\frac{2\mu_1}{r} - \frac{\mu_1}{a}}, \quad \text{and} \quad V_{ga} = \sqrt{\frac{\mu_1}{r}} \tag{2.80}$$

to get a new expression for V_∞^2

$$V_\infty^2 = \left(\frac{2\mu_1}{r} - \frac{\mu_1}{a}\right) + \frac{\mu_1}{r} - 2V_{ga}\frac{h}{rV_{ga}}\sqrt{\frac{\mu_1}{r}} = \frac{3\mu_1}{r} - \left[\frac{\mu_1}{a} - 2\sqrt{\frac{\mu_1}{r^3}}h\right]. \tag{2.81}$$

If we use Equation 2.33 and Equation 2.76 to insert ω and replace h in the bracketed term above we find that it becomes equivalent to the expression for the Jacobi in Equation 2.77. Noting that the first term equals $3V_{ga}^2$ we have

$$V_\infty^2 = 3V_{ga}^2 - J_{3b,i}. \tag{2.82}$$

Now we have an expression for the relationship between the Jacobi and V_∞. V_{ga} is constant for a circular orbit and yields a simple quadratic relationship. We can normalize the expression by dividing each term by V_{ga}^2, noting that $V_{ga}^2 = (1-\mu)(R\omega)^2$ which is close to the term in Equation 2.44. Now we have

$$v_\infty^2 = 3 - \frac{1}{1-\mu}J_{3,i} \cong 3 - J_{3,i}, \tag{2.83}$$

where the lower-case v denotes the normalized quantity. Recall that $\mu<<1$. Solving Equations 2.82 and 2.83 for J we have

$$J_{3b,i} = 3V_{ga}^2 - V_\infty^2 \quad \text{and} \quad J_{3,i} = (1-\mu)(3-v_\infty^2). \tag{2.84}$$

V_∞ and Hill's Problem. Having derived the relationships between the PR3BP and Hill's Problem (Eqs. 2.59 and 2.60), we can now write the equivalence between V_∞ and J_H:

$$V_\infty^2 = 2J_{H,d} \quad \text{and} \quad v_\infty^2 = 2\frac{\mu^{2/3}}{1-\mu}J_H,^{13} \tag{2.85}$$

and solving for J:

$$J_{H,d} = \frac{V_\infty^2}{2} \quad \text{and} \quad J_H = \frac{1-\mu}{2\mu^{2/3}}v_\infty^2. \tag{2.86}$$

The relationships in Equations 2.84 and 2.86 indicate that V_∞ is positive when J_3 goes below 3 or when J_H is positive. These orbits are hyperbolic in the two-body formulation but are bound to the "vicinity" when third body effects are taken into account.

[13] Equation 2.54 yields the relationship $v_\infty^2 = \frac{-\mu^{2/3}}{1-\mu}\Gamma$.

3 V_∞ Leveraging

3.1 Introduction

V_∞ leveraging is the use of a deep-space maneuver to modify the V_∞ of the spacecraft upon reencounter. They are typically used in conjunction with gravity-assists in order to change the spacecraft's energy and reduce the total ΔV for a mission. The first example of such a maneuver was introduced by Hollenbeck (1975) in the form of the ΔV-EGA (Delta-V Earth-Gravity-Assist). In this maneuver a spacecraft is launched on a nearly resonant orbit with Earth, usually 2:1. A small deep-space maneuver (~ 0.5 km/s) is then performed at aphelion to lower the perihelion and reencounter Earth non-tangentially with a V_∞ greater than that at launch. As shown in Figure 3.1a, this fly-by can occur before or after the new perihelion. In this manner the Earth can be used as a gravity-assist body to bend the new V_∞ vector towards parallel with its own velocity vector in order to maximize heliocentric energy.

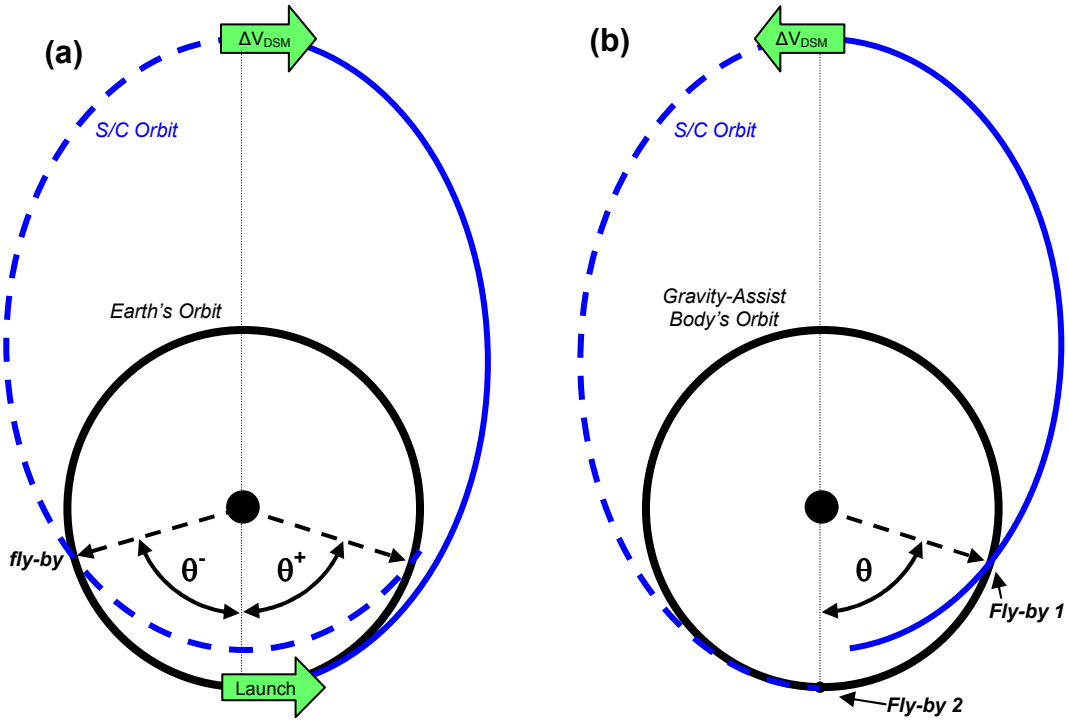

Figure 3.1. V_∞ Leveraging. (a) ΔV-EGA Trajectory - A spacecraft is launched tangentially into a nearly resonant orbit. At apoapsis a retro-burn is used to retarget the Earth at a new location with a greater V_∞. (b) V_∞ Reduction Maneuver – Fly-by 1 sets up the desired orbit where a positive burn raises periapsis to reencounter the body tangentially and minimize V_∞.

Originally the fact that slowing down at the slowest point (rather than speeding up at the fastest point) in the orbit actually led to the greatest increase in energy was chalked up to the counterintuitive nature of orbital mechanics. The conventional explanation of the ΔV-EGA was that it was easier to change the orbit when the velocity was the lowest. Altering the shape of the orbit changes the angle at which the spacecraft and planet crossed. This leads to the greatest difference in velocity possible with a close fly-by and leads to the greatest heliocentric energy. A better explanation was offered by Sweetser (1993) when he showed that the change in Jacobi's constant is maximized if a maneuver is performed when the rotating-coordinate velocity is the greatest, which is the case at apogee.

If we substitute $V_{sc}^{'} + \Delta V_{sc}^{'}$ for $V_{sc}^{'}$ in the equation for Jacobi's integral[14] and differentiate we get

$$-\Delta J = 2V_{sc}^{'}\Delta V_{sc}^{'} + (\Delta V_{sc}^{'})^2, \tag{3.1}$$

where $V_{sc}^{'}$ denotes the velocity in the rotating coordinate system. By setting Equation 3.1 equal to zero, it is possible to calculate an approximate value for the change in V_∞ for a given ΔV.

Credit is given to Sims and Longuski (1994, 1997) for coining the term "V_∞ Leveraging" and further developing its application to interplanetary missions. An analysis was done to determine the maximum aphelion radius achievable for a given total ΔV. Figure 3.2 shows the significant improvement in performance provided by a V_∞ leveraging maneuver. The numbers next to each curve indicate the resonance with the Earth and the '+' indicates that the orbits reencounter after the new periapsis.

[14] $J = 2U - V_{sc}^{'2}$, where U is the pseudo-potential in the three-body problem

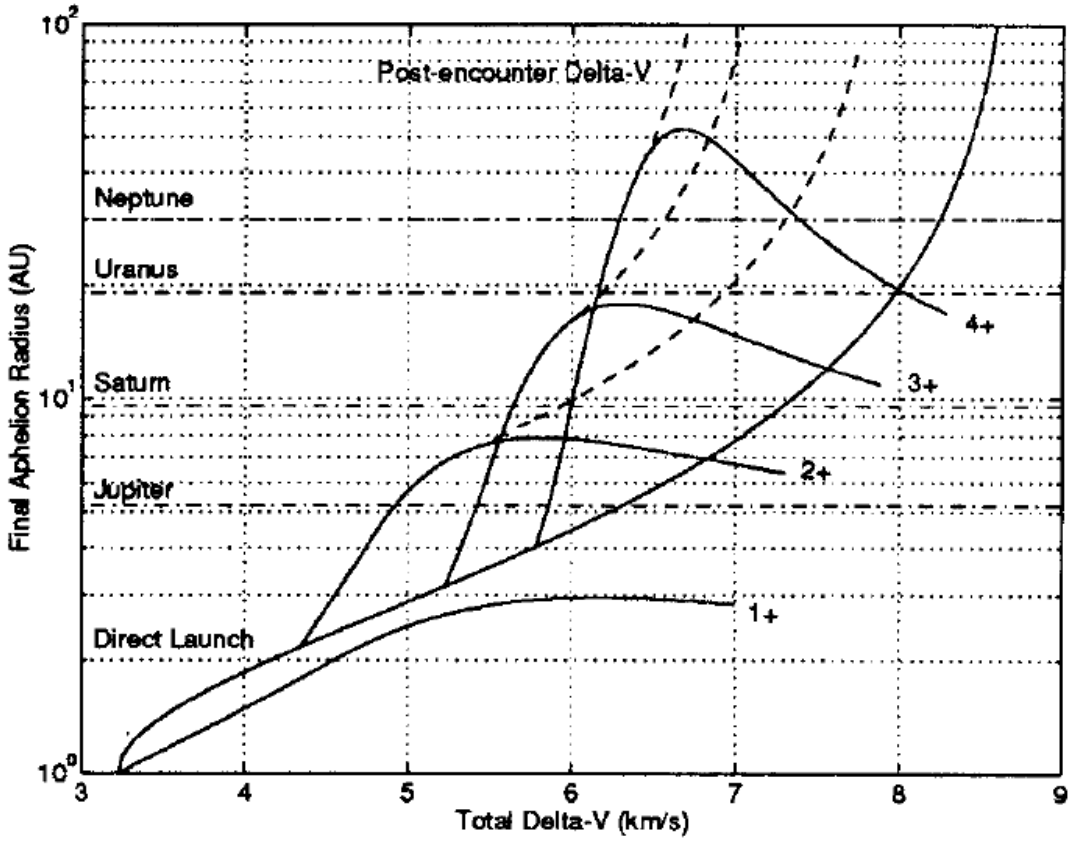

Figure 3.2. ΔV -EGA Performance (Sims, 1994). The numbers next to each curve indicate the resonance with the Earth and the '+' indicates that the orbits reencounter after the new periapsis.

The typical assumptions for ΔV-EGA trajectory analyses found in the literature are as follows: 1) Earth is in a circular orbit, 2) a zero-sphere of influence patched-conics model is used, 3) the spacecraft is launched from a 185 km Earth orbit with a hyperbolic excess velocity parallel to the velocity of the planet, 4) the initial heliocentric orbit has a period "slightly" (never quantified[15]) greater than an integer

[15] The literature never specifies what "slightly" means, nor why exactly resonant or less than resonant orbits should not be used. We will explore these assumptions later in this dissertation and quantify the results.

number of years, 5) at aphelion an instantaneous, tangential burn is applied to lower the orbit energy and reencounter the Earth either before or after periapsis, and 6) the new, greater V_∞ is rotated via fly-by with a minimum altitude of 200 km to maximize final aphelion distance.

As stated by Sims (1994): "We can infer from Sweetser's analysis that the most efficient deep space maneuver is at aphelion and parallel to the velocity at that point." However, it is noted by Casalino and Cosalurdo (1998) that this method may be suboptimal but yields sufficient accuracy and speed for preliminary mission design.

Multiple revolutions of the Earth and spacecraft on their orbits are also possible: simple ΔV-EGA trajectories are classified by means of the designation $K{:}L(M)^{\pm}$ where

K = number of Earth orbit revolutions

L = number of spacecraft orbit revolutions

M = spacecraft orbit revolution on which the ΔV is applied ($1 \leq M \leq L$)

$\pm$ = Earth encounter after/before the spacecraft orbit perihelion

A 3:2(2)+ ΔV-EGA, for example, means that the spacecraft leaves Earth on a ~1.5 year orbit, performs a negative burn at its second apoapsis, then reencounters the Earth slightly beyond the original launch location.

In a general sense, V_∞ leveraging can be performed on orbits both exterior and interior to the body's orbit, and in both forwards (see Figure 3.1b) and backwards (Figure 3.1a) directions with respect to the spacecraft velocity. Both Backward-Exterior and Forward-Interior maneuvers serve to increase V_∞ while Forward-Exterior

and Backward-Interior maneuvers decrease V_∞. In the latter two cases the spacecraft reencounters the body tangentially while the opposite is true for the former two. This is because V_∞ is minimized when $\alpha = 180°$, i.e. when V_{ga} and V_{sc} are parallel.

The ΔV-EGA we have discussed is an example of a Backward-Exterior leveraging maneuver, which increases V_∞. For the endgame problem, however, we wish to decrease the V_∞ while coming in from a larger orbit, so Forward-Exterior leveraging is in order.

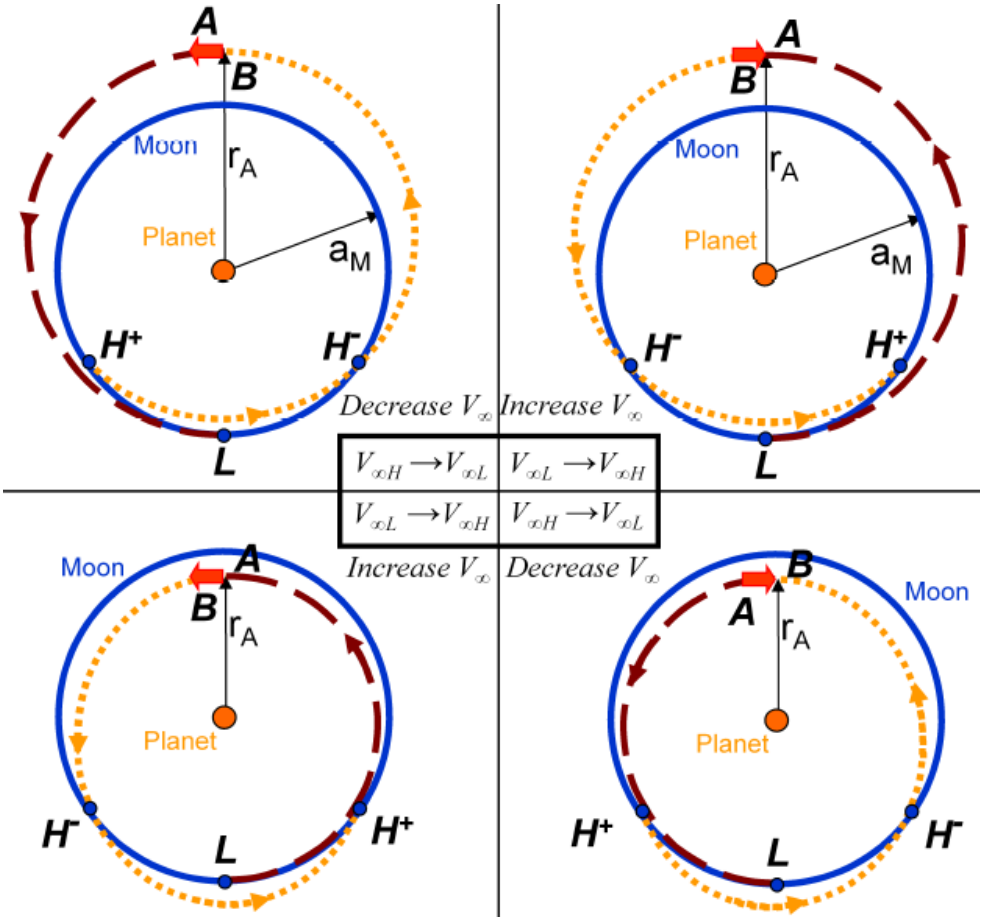

Figure 3.3. Four variations of the V_∞ leveraging maneuver (Campagnola, 2010a)

3.2 Applications to Endgame Tours

(Chains or sequences of maneuvers)

In this chapter we describe the V_∞ Sphere and the V_∞ Plane, which serve as a map for the range of all possible orbits accessible via leveraging maneuvers and fly-bys. In the next section we mathematically describe V_∞ leveraging maneuvers and present a new analysis method using a Lambert's Solver. From this, we plot contours of leveraging maneuver efficiencies and present a method using only the most efficient V_∞ leveraging maneuvers, fly-bys, and powered fly-bys[16] to calculate the theoretical minimum ΔV required to reduce V_∞ to zero given an infinite flight time. Then we explore the domain of finite tour sequences and compare the results to the theoretical minimum. As is often the case in trajectory design, a trade must be made between performance (minimizing ΔV) and time-of-flight (*TOF*).

In order to create the data to characterize this trade space, a Monte-Carlo type simulation was set up to generate random sequences of resonances[17] (not restricted to integer resonances) along with associated fly-bys and V_∞ leveraging maneuvers. Pathway sequences are created in the simulation by following a predetermined rule or set of rules. For example, a sequence may require that only integer resonances be used and that non-tangential leveraging is not allowed. Each rule can be treated like a heuristic where some trade between reduced fuel usage and increased flight time is being made. Intuitively, there is a general trend towards decreasing ΔV by increasing

---

[16] A tangential ΔV maneuver performed at periapsis of the fly-by. Powered fly-bys become more efficient than leveraging maneuvers for small values of V_∞

[17] This is similar to "resonance hopping" tours found in the literature

TOF. However, some pathway rules are not as effective as others in trading ΔV for time and lead to contradictions to this trend.

Total ΔV is plotted versus *TOF* to create a Pareto front and to reveal the trends that prove to be most efficient for V_∞ leveraging sequencing. The derived heuristics would be valuable to mission designers for both quick-look evaluations and in finding a globally optimized solution given a set of mission parameters.

3.3 Models and Normalization

In order to analyze the vast trade space of possible trajectories, we use a zero-sphere-of-influence patched conic approximation (Section 0) which allows for rapid computation with reasonable fidelity. Our simplified system consists of a large central body with a smaller body, denoted the "gravity-assist" body, in a circular orbit. A spacecraft[18] is located in a co-planar orbit about the central body and flies by the gravity-assist body with the ultimate goal of gravitational capture at that body. The spacecraft is governed by the two-body equations of motion and is perturbed instantaneously during encounters with the gravity-assist body.

The hyperbolic excess velocity with respect to the gravity-assist body, or the V_∞ vector, is constant in the absence of perturbations and can be turned via close fly-bys of the gravity-assist body up to the maximum turn angle, given by Equation 2.26. The direction of the V_∞ vector is defined by the angle α, which is the angle between V_∞ and V_{ga} and varies from 0° (parallel) and 180° (anti-parallel) (See Figure 2.5).

[18] Quantities pertaining to the spacecraft will have a subscript "sc", whereas the gravity-assist body's will be denoted with a "ga"

Because the V_∞ vectors before and after have the same length, the locus of all possible V_∞'s after fly-by lie on a sphere centered at the head of V_{ga}.

Changing α via fly-by, coined "orbit pumping" by Uphoff et. al.(1976), changes the orbital energy and period about the central body. Post-fly-by orbital parameters are controlled through suitable selection of encounter conditions such that δ_{max} given in Equation 2.26 yields a new $V_{\infty,out}$ vector that results in the desired outgoing velocity and period. The contours of all possible post-fly-by orbit parameters (inclination, period, resonance, periapsis, etc.) can be mapped onto the surface of a sphere (or V_∞ globe) as an aid to mission design (Strange et al., 2007). Sequences of same-body transfers can be mapped across the surface of this globe in steps equal to or less than δ_{max}.

The normalized units described by Section 2.2.10 are used throughout this dissertation so that the results can be applied to any system with the proper scaling. Recall that normalization is achieved by dividing length, velocity, and time by the semimajor axis (a), circular velocity (V_{ga}), and period (P) of the gravity-assist body, respectively. Table 3.1 lists these values along with the gravitational parameter (μ) and the minimum permissible fly-by radius[19] (r_{min}) for various moons in the solar system along with Mercury[20]. The last column lists the local circular velocity (V_c) at r_{min} in normalized units. V_c is indicative of how much control authority a particular moon has on bending the V_∞ vector during fly-by. Moons with a larger V_c such as

[19] Minimum fly-by altitude is 100 km for each moon except Titan, which is 500 km due to atmosphere.

[20] Mercury may not be an ideal candidate for this analysis as it has a long period and low V_c. However, it still may benefit from some reduction of ΔV for a longer flight time, as is the case with the MESSENGER spacecraft.

Titan may only require one fly-by to achieve the desired direction, whereas a smaller moon like Enceladus could require multiple fly-bys to achieve the same effect.

Table 3.1. Normalization Parameters for a Few Celestial Bodies

Body	μ (km^3/s^2)	a (10^5 km)	V (km/s)	P (days)	r_{min} (km)	V_c
Io	5960	4.2	17.3	1.8	1921	0.10
Europa	3203	6.7	13.7	3.6	1661	0.10
Ganymede	9888	10.7	10.9	7.2	2731	0.17
Callisto	7179	18.8	8.2	16.7	2510	0.21
Enceladus	7	2.4	12.6	1.4	352	0.01
Rhea	154	5.3	8.5	4.5	864	0.05
Titan	8978	12.2	5.6	16.0	2876	0.32
Triton	1428	3.5	4.4	5.9	1453	0.23
Moon	4903	3.8	1.0	27.3	1838	1.60
Mercury	22032	579.1	47.9	87.9	2540	0.06

3.4 The V_∞ Sphere

Strange et al. (2007) present a graphical method for the design of same-body transfers which they called the V_∞ Globe (see Figure 3.4). Since the asymptotic velocity relative to the body is unchanged in an unpowered fly-by maneuver, the locus of all spacecraft velocity vector tips creates a sphere with radius equal to the magnitude of V_∞. The contours of all possible post-fly-by orbit parameters (inclination, period, resonance, periapsis, etc.) can be mapped onto the surface of this sphere to aid in mission design.

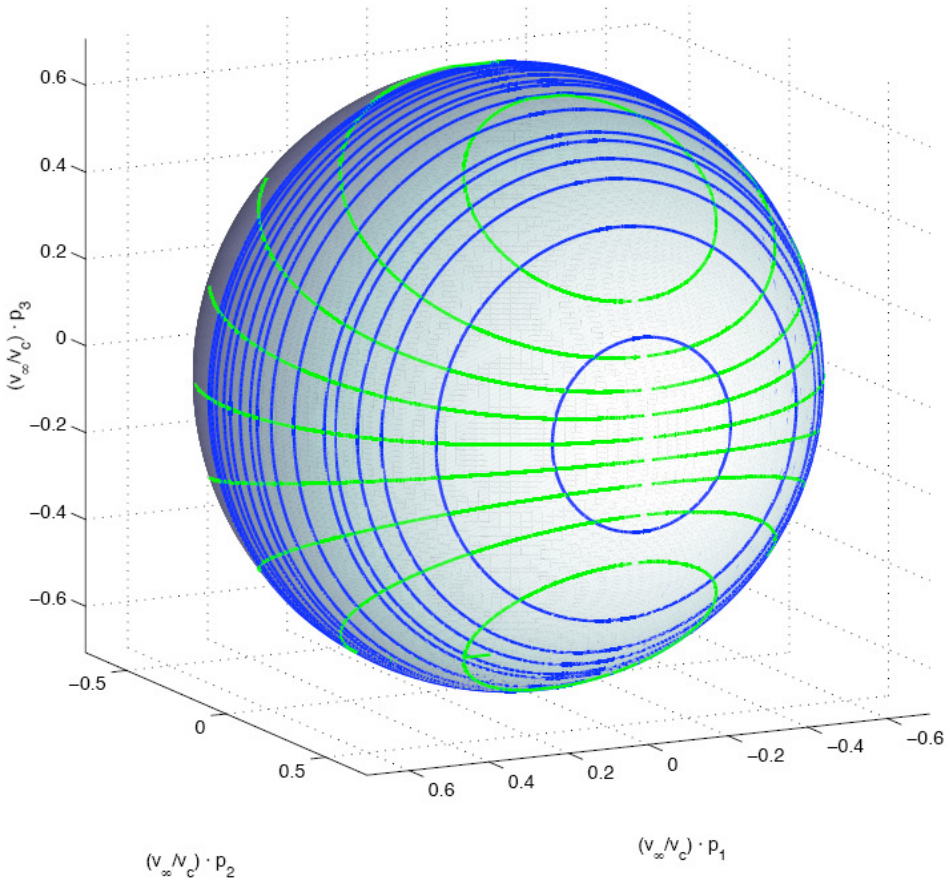

Figure 3.4. The V_∞ Globe (from Strange et al. (2007)). Represents all possible V_∞ vector tips after a fly-by. Contours of resonant orbits (blue) and inclination (green) are mapped onto the surface.

At each encounter of the fly-by body, a new orbit can be achieved via careful targeting of B-plane parameters such that the outgoing asymptote is properly turned to place the spacecraft on the desired trajectory. The magnitude of the maximum turn angle, δ_{max}, is limited by V_c and V_∞, as shown in Equation 2.26. Thus, in the absence of outside perturbations, fuel expenditures, aero-gravity-assists, etc., the maximum δ represents the angular "step" size[21] across the surface of the V_∞ Globe. The

[21] As an example, at the end of its prime mission, the Cassini probe had a V_∞ of 5.8 km/s and a maximum δ of 8°.

individual orbits of a tour can be plotted along the surface of the globe as points separated by less than the maximum turn angle.

The entire surface of the V_∞ Globe is not accessible in practice, even if an unlimited number of fly-bys are used. For example, there is a region which separates prograde and retrograde orbits that impacts the central body, making it practically impossible to reverse an orbit from retrograde to prograde using a gravity-assist. If V_∞ is great enough, there is a large area on the globe where the orbit becomes hyperbolic with respect to the central body and escapes the system.

3.4.1 Accessible Regions

Using the law of cosines for the triangle made up of the velocity vectors in Figure 2.5, we get

$$V_{sc}^2 = V_\infty^2 + V_{ga}^2 + 2V_\infty V_{ga}\cos\alpha\,. \tag{3.2}$$

If we utilize the normalized form of the *vis-viva* equation to solve for V_{ga} in terms of V_{sc} and a_{sc} we can substitute and rearrange Equation 3.2 to get an equation for the inverse semimajor axis in terms of V_∞ and α:

$$a_{sc}^{-1} = 1 - V_\infty^2 - 2V_\infty\cos\alpha\,.^{22} \tag{3.3}$$

With V_∞ fixed and α limited to 0°-180°, we now have bounds on a_{sc}:

$$1 - V_\infty^2 + 2V_\infty \le a_{sc}^{-1} \le 1 - V_\infty^2 - 2V_\infty\,. \tag{3.4}$$

Equation 3.4 is plotted in Figure 3.5 for four values of α: 180° (minimum energy), 0° (maximum energy), 90°, and α_{critical} (division between prograde and

[22] For a more detailed derivation see Strange et al. (2007)

retrograde). For values of V_∞ below 0.41 ($\sqrt{2}$ -1), all orbits are restricted to positive values of a_{sc} and therefore are elliptical and bound to the central body. Between 0.41 > V_∞ > 2.41, it is possible for a_{sc} to become negative, i.e. hyperbolic. Above 2.41 ($\sqrt{2}$ +1), all orbits are hyperbolic regardless of α and thus, they are not suitable for our purposes. If we note that semimajor axis and period[23] are related by $a_{sc}^3 = T_{sc}^2$, then these three regions give us insight into what the V_∞ globes might look like for different values of V_∞ with the relative size of their inaccessible zones.

[23] Targeting resonant orbits is critical to tour design.

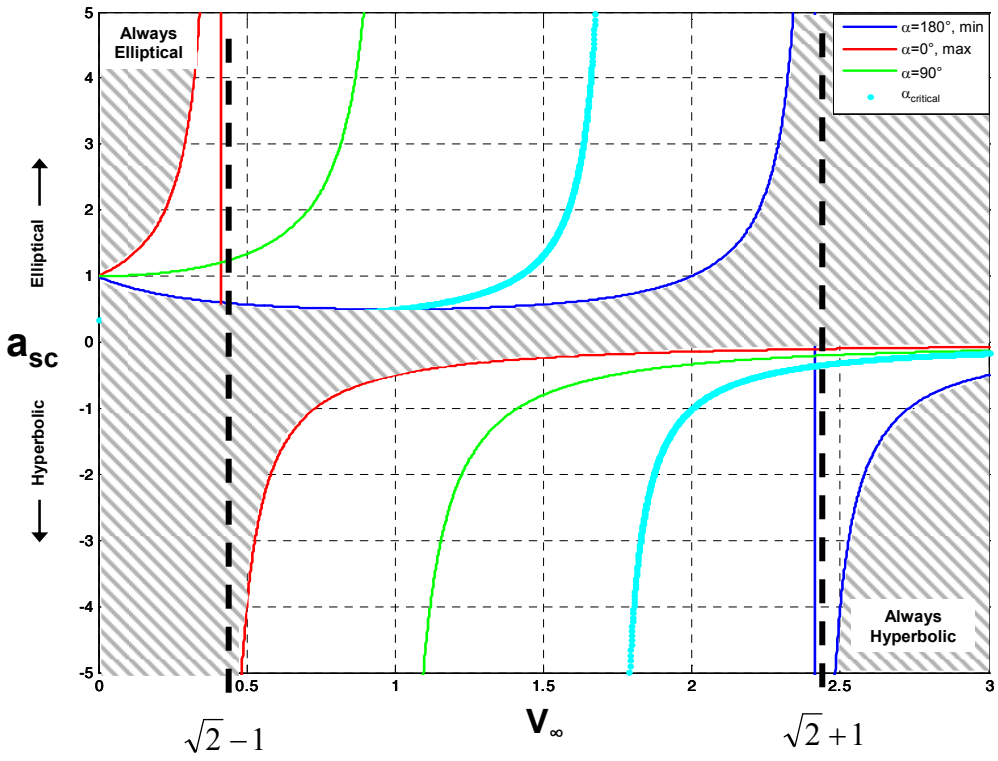

Figure 3.5. Bounds on Semimajor Axis vs. V_∞. Values of normalized V_∞ less than 0.41 are always elliptical regardless of α, and values above 2.41 are always hyperbolic.

3.4.2 Shrinking the V_∞ Sphere

In the linked-conic approximation it is impossible to change the magnitude of the V_∞ vector ballistically. This is analogous to the Jacobi constant of the restricted three-body problem. Due to the constancy of these parameters, the V_∞ Globe is, by definition, exactly the same on every encounter regardless of the location or fly-by characteristics. If we desire to reduce the relative speed of the spacecraft and become captured, nothing can be done on the fixed globe. Herein lies the *ballistic endgame paradox*.

In the absence of outside perturbations, fuel expenditure is required to reduce the magnitude of V_∞. This change brings about a new, smaller V_∞ globe with shifted

parameter contours, like the next layer of an onion. The set of all the layers is the "V_∞ Sphere". The 3-dimensional structure of the parameter contours of the whole V_∞ Sphere are difficult to visualize, let alone depict graphically. For simplicity[24] we will slice the sphere equatorially to create a 2-D map, sufficient to analyze tours that remain in the plane of the gravity-assist body, which will be the case for the remainder of this dissertation.

A planar slice of the V_∞ Sphere, shown in Figure 3.6, depicts all the V_∞ vector tips of orbits lying in the plane of the gravity-assist body. The polar angle is the pump angle (α), and the radial magnitude is V_∞. The V_∞ magnitudes, periapses (r_p), and apoapses (r_a) are in normalized units. Orbits to the left of the green line are retrograde with the dotted area around the line indicating orbits that would impact a typical central body ($R_{cb}/a_{ga} = 0.05$). The red dotted line separates the elliptical orbit region from the hyperbolic.

[24] Analyzing the nature of V_∞ leveraging maneuvers is much more straightforward when dealing with planar orbits, whose general principles can be extrapolated to all orbits. However, non-zero inclinations add a new facet to possible leveraging orbit combinations, but are beyond the scope of this dissertation.

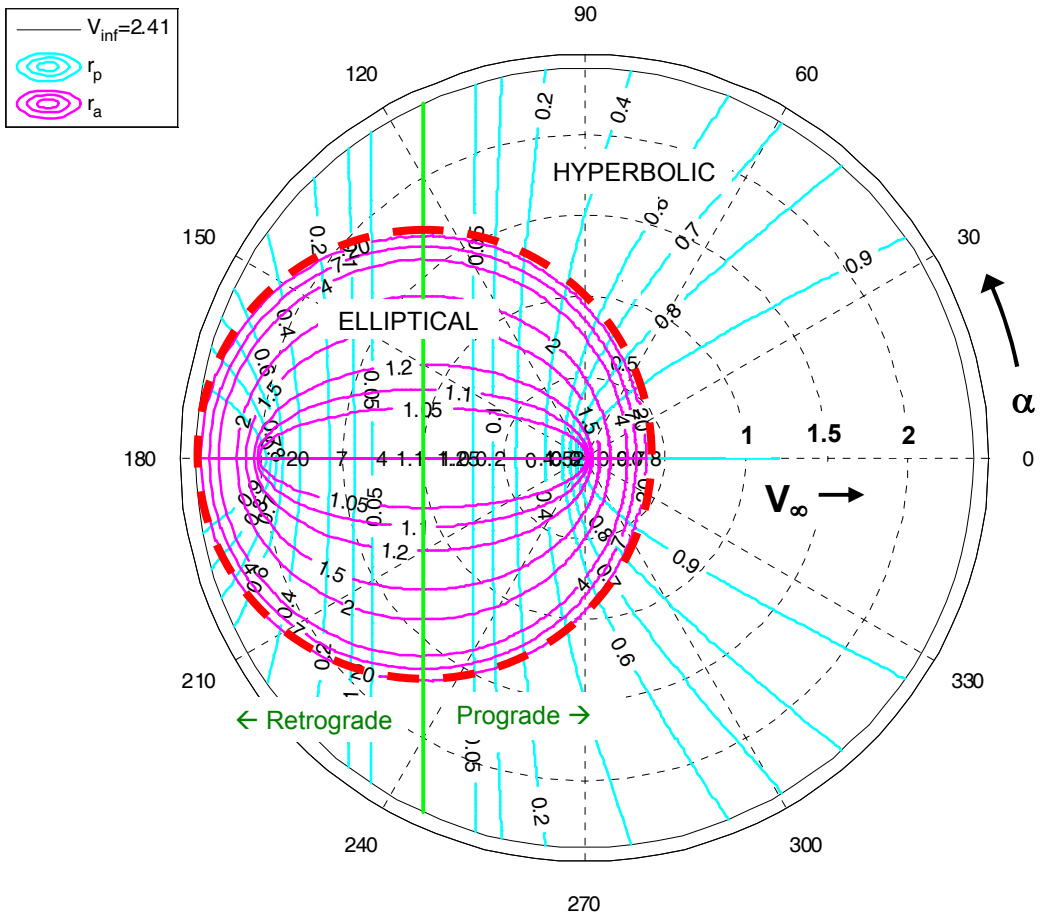

Figure 3.6. The V_∞ Plane. Represents all orbits possible after a planar fly-by. Unpowered fly-bys may change α but will remain on concentric rings. The blue lines show contours of periapsis points while the magenta ones show apoapsis points. The green solid line separates prograde and retrograde orbits and the red dashed line encompasses the elliptical orbits.

A spacecraft is constrained to a concentric ring in the absence of a ΔV maneuver. It can move along the ring in steps of δ_{max} or less for free (i.e. no fuel required) during fly-bys. Each fly-by would of necessity target a resonant orbit (contours not depicted here for clarity) in order to return in a finite amount of time. ΔVs place the spacecraft on a smaller ring which can then be traversed in steps of the new δ_{max}. An endgame tour could be represented by points creating a zigzagging path towards the center of the map, at which point V_∞ would equal zero and the spacecraft

would be at the limit of gravitational capture. The object now is to find the path that requires the minimum total ΔV.

The same planar map in a Cartesian projection is shown in Figure 3.7. In this projection the spacecraft can move left and right (changing α) on horizontal lines for free, or expend fuel in order to move lower (lowering V_∞). Prograde, elliptical orbits are those found below the green and red lines, respectively. It can be seen why retrograde orbits are not used in tours as they cannot reach $V_\infty = 0$ without becoming prograde first, which is prohibitively expensive, fuel-wise. In addition to the apses, contours for eccentricity and resonance (T_{sc}/T_{ga}) given by

$$T_{sc}/T_{ga} = R = \left(1 - V_\infty^2 - 2V_\infty \cos\alpha\right)^{-3/2}, \tag{3.5}$$

are plotted on this map.

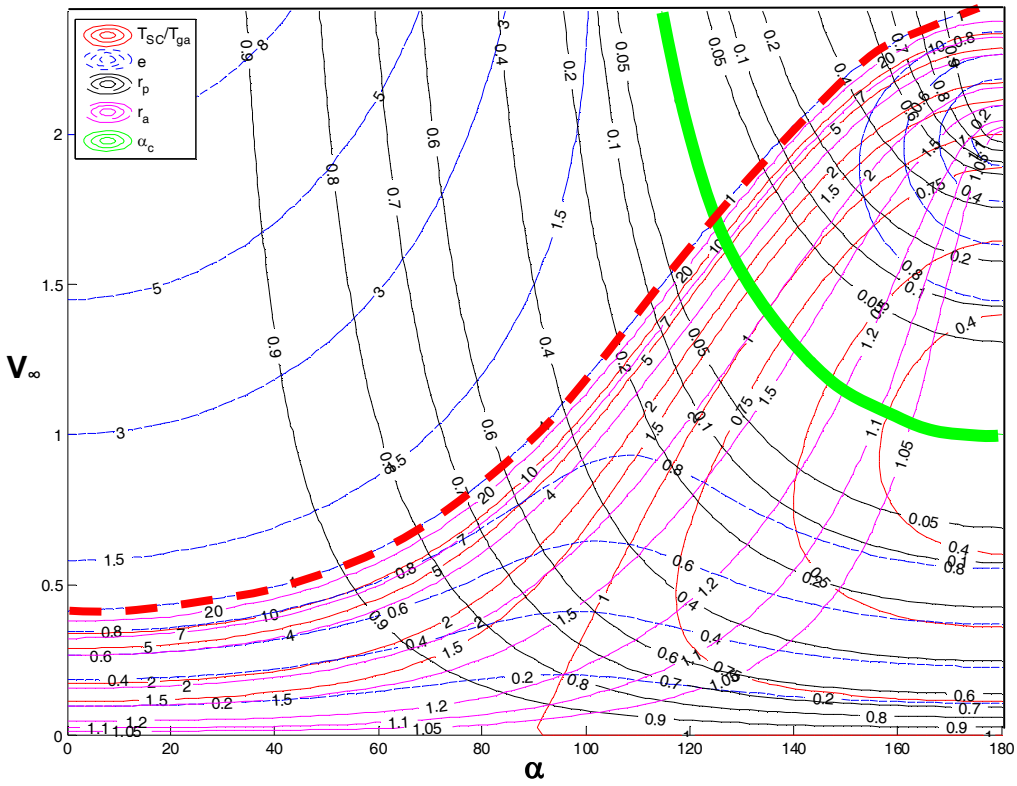

Figure 3.7. Cartesian Projection of V_∞ Plane. Similar to the previous figure but with contours for resonant orbits (red) and eccentricity (blue dashed) as well. Elliptical orbits are located below the red dashed line and retrograde orbits are above the green line.

The plot in Figure 3.8 is a blow up of the lower left-hand corner of Figure 3.7. Plotted on this map are contours for resonance (T_{sc}/T_{ga}) and $\delta_{\max}$ for various values of V_c. As we seek to reduce the magnitude of V_∞ from some initial value to zero (capture), this map is used to plot potential pathways. One such pathway is represented by arrows on the plot. See Table 3.2 and the associated discussion for more details on how this sequence was constructed.

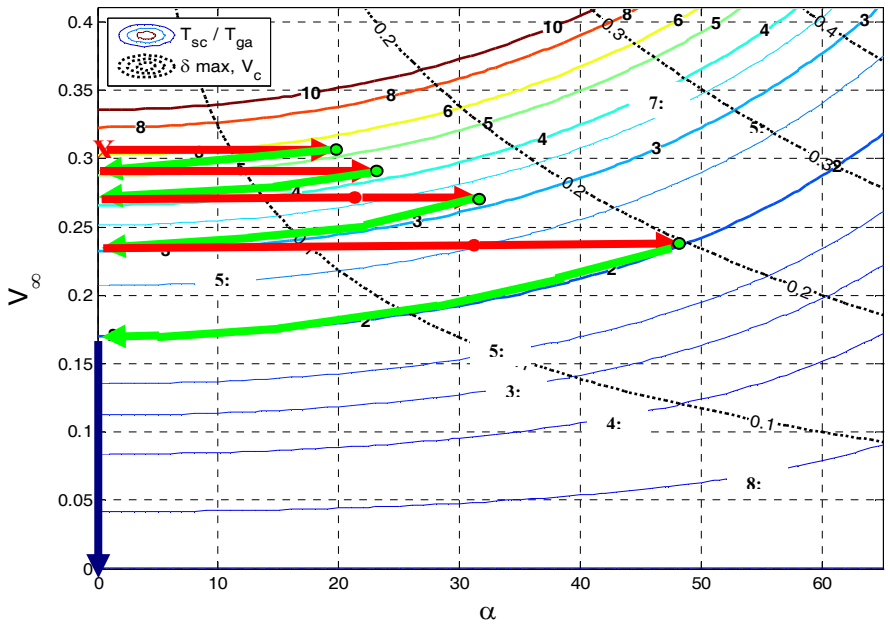

Figure 3.8. The V_∞ Resonance Plane with an Example. Colored contours represent lines of resonance for orbits of a given V_∞ and α. The dashed black lines show the maximum turn angle, δmax, as a function of local circular velocity, V_c, and V_∞. One potential pathway is illustrated with fly-bys, leveraging maneuvers and powered fly-bys represented by red, green, and blue arrows, respectively.

3.5 Designing V_∞ Leveraging Maneuvers

Since each type of maneuver consists of a known, tangential encounter and an (initially) unknown, non-tangential encounter, it is easier to begin with the known and target the unknown, as is the case with the ΔV-EGA trajectory. The beauty of the patched-conic approximation is that all trajectories are symmetric with respect to time, so we can find solutions for the more intuitive ΔV-EGA and then apply the results in reverse to the endgame problem.

The standard method for calculating V_∞ leveraging maneuvers is an iterative one due to the transcendental nature of the set of two-body equations used (see

Hollenbeck, 1975). After the spacecraft is launched to a slightly longer than resonant orbit, a guess is made at the value of a burn (ΔV_{DSM}) performed anti-parallel at aphelion. The trajectory is then propagated to where it intersects Earth's orbit, both before and after perihelion. The Earth is then propagated to see if a reencounter occurs at either point. If not then ΔV_{DSM} is modified, and the process is repeated until they converge. See Sims (1997) for a more detailed description.

V_∞ leveraging analyses found in the literature focus on tangential transfers where the orbits of the spacecraft and gravity-assist body are tangent to begin or end the maneuver. This is because a tangential transfer results in the greatest change in V_∞ for a given transfer orbit size. However, occasionally it is more desirable to perform a non-tangential transfer ($\alpha \neq 0$ at either end), particularly in sequences of leveraging maneuvers where V_c of the moon is low, which makes it difficult to bend α back to zero without requiring multiple fly-bys and a long *TOF*.

3.5.1 The Lambert Solution Technique

In order to more completely explore the trade space, a different approach to leveraging design was used. We desired to free the constraints on the location and direction of ΔV_{DSM}. To do so a universal variables solution to Lambert's Problem was implemented in MATLAB (Bate, Mueller, and White, 1971; Vallado, 2001) This was done by first propagating the orbits of the gravity-assist body and the spacecraft to produce a specified number of ephemeris points per orbit (nominally 360). Next, the program loops through every combination of starting points on the spacecraft orbit and targets points on the gravity-assist body's orbit using the Lambert Solver to find the ΔV direction and magnitude required to complete the transfer.

The true anomaly of the starting point on the spacecraft's orbit is denoted ν, while the true anomaly of the reencounter is θ. Both start at zero as the spacecraft leaves tangentially. Positive values of θ (θ^+) refer to long transfers past periapsis, and negative values (θ^-) designate short transfers (see Figure 3.9), where θ is between -180° and 180°. In practice ν had to be constrained to less than ~220° because larger values had difficulty converging and values below 70° (yellow region below) did not show much gain. Arrival θ was also generally restricted to +/-65° (pink region) due to difficulties in targeting higher values.

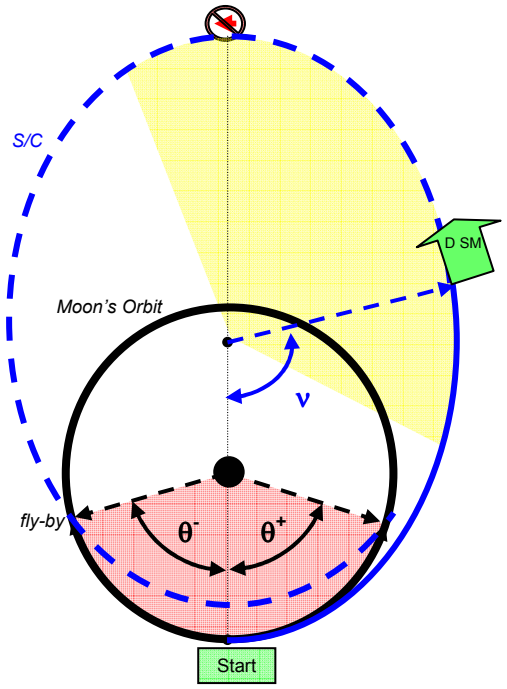

Figure 3.9. Lambert Solution Technique for V∞ Leveraging. A deep-space maneuver is performed at any true anomaly (ν) and a Lambert's solver is used to determine the direction and magnitude to retarget the body at any location (θ).

3.5.2 V_∞ Leveraging Efficiency

The efficiency of the leveraging maneuver is defined to be the ratio between the change in V_∞ and the magnitude of the deep-space burn:

$$Eff = \frac{V_{\infty,final} - V_{\infty,initial}}{\Delta V_{DSM}} = \frac{\Delta V_\infty}{\Delta V_{DSM}}. \tag{3.6}$$

Contour plots were then created to illustrate the locations of the ν-θ pairs with the greatest efficiency. Figure 3.10a shows the efficiencies of leveraging maneuvers from a 2:1 exact resonance orbit ($V_\infty \cong 0.17$). Note that there are two regions of higher efficiency – one each for positive and negative values of θ, with efficiencies going to

zero around θ = 0 (which would be the nominal trajectory). Efficiency is generally greater

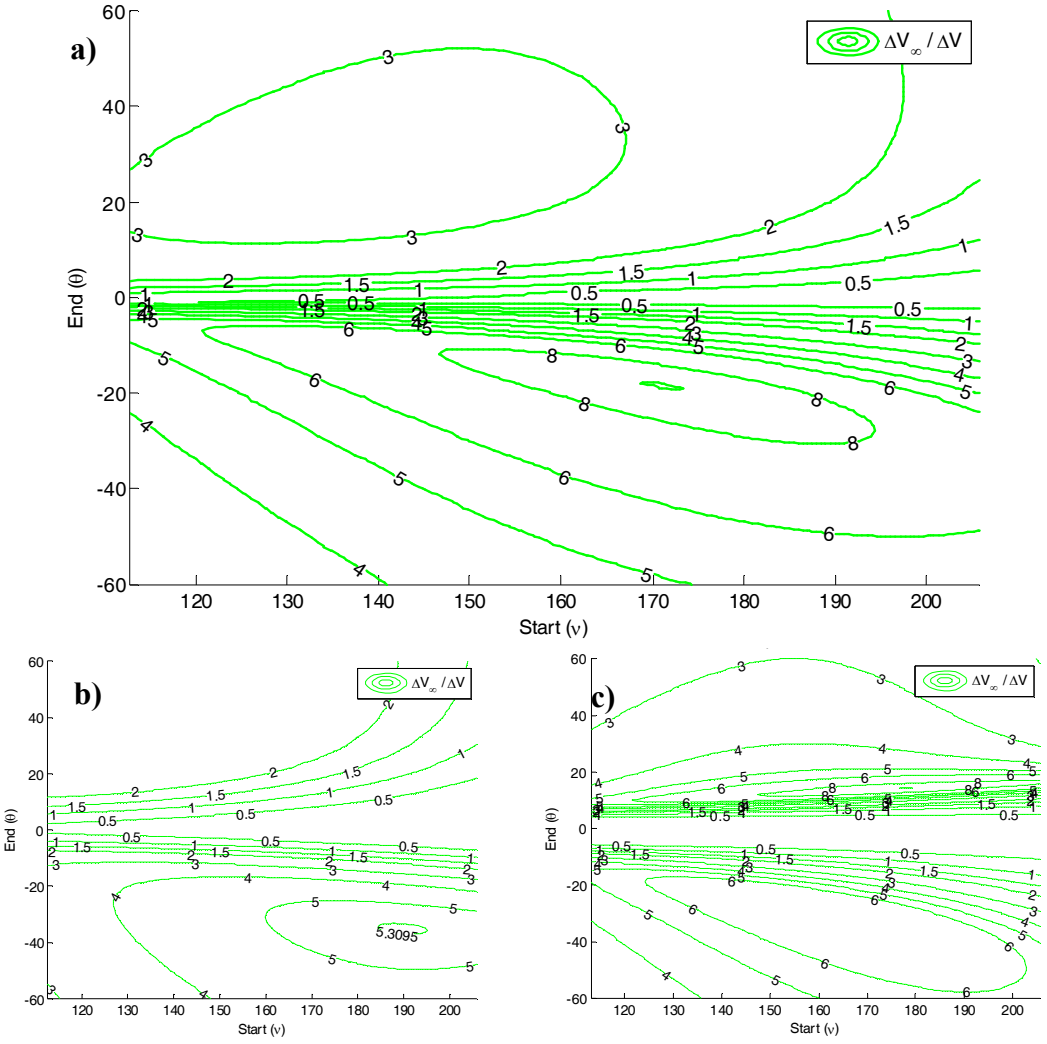

Figure 3.10. Efficiency of V∞ Leveraging near 2:1 Resonance. ν is the location of the burn and θ is the location of reencounter. a) Efficiencies for 2:1 – note that there are two peaks, with the largest being for -θ. b) Efficiencies for 1.99:1. c) Efficiencies for 2.01:1

for the short transfers and has a peak of 8.86 at ν = 172° and θ = -19°. This result is interesting in that the maximum efficiency does not occur at the apoapsis (θ = 180°).

The location of the point of maximum efficiency is very sensitive to the initial resonance[25]. If it is slightly off of integer resonance, the efficiency and location can change dramatically. The bottom left plot in Figure 3.10 shows the efficiency contours for a 1.99:1[26] orbit. The maximum efficiency has now shifted to 5.32 at ν = 189° and θ = -35°. Long transfers (positive θ) are not very efficient at all. The bottom right plot shows the 2.01:1 contours. Note that now the most efficient location is a long transfer at θ = 14° with an efficiency of 9.25. At a 2.1:1 orbit the most efficient location moves out further still to (170°, 49°) with the peak efficiency falling to 6.9.

With all the sensitivity to initial orbit resonance, the question arises as to where the peak efficiency actually occurs. Figure 3.11a shows the maximum efficiency for any ν-θ combination of orbits with resonances from 1.8:1 to 2.4:1 in steps of 0.01. In this plot the maximum occurs at 2.01:1 with efficiencies falling off much more rapidly for the resonances less than 2:1 than those greater, illustrating that orbits greater than integer resonance are preferable.

---

[25] The term "resonance" is used loosely to denote the ratio of the orbit periods, regardless of rationality

[26] It is not necessary to be in an integer resonance with the gravity-assist body in order to return since the leveraging maneuver makes up the difference. If no maneuver will be performed after a fly-by, then it is crucial to use the gravity –assist to target a resonance.

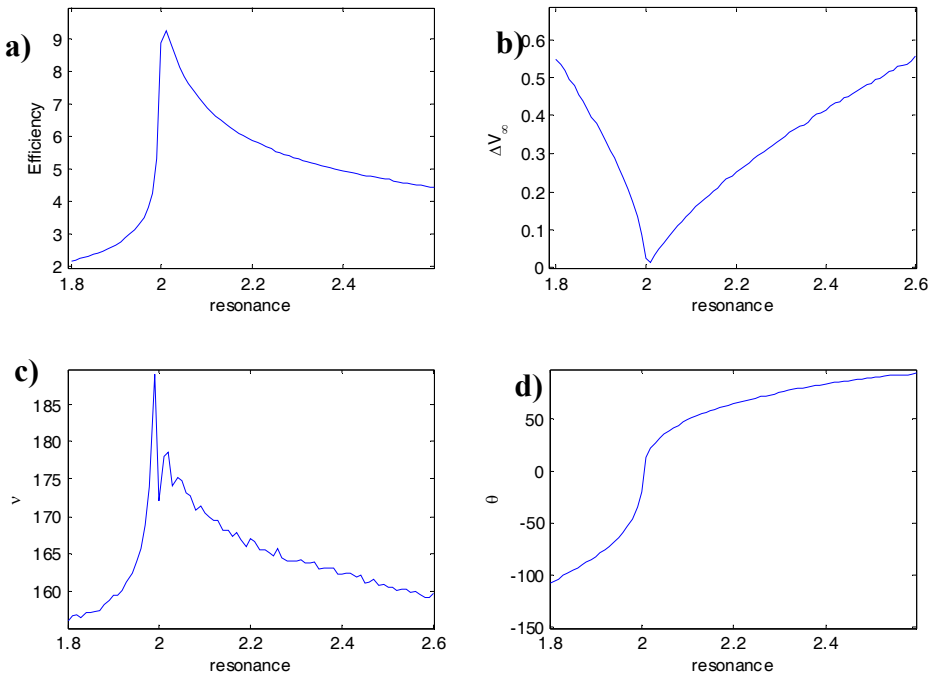

Figure 3.11. (a) Leveraging efficiencies around 2:1 resonance, (b)-(d) The ΔV_∞'s, ν's, and θ's associated with the peak efficiencies in (a).

Figure 3.11c and Figure 3.11d show the ν and θ, respectively, of the reencounter locations for the points of maximum efficiency in Figure 3.11a. The maneuvers mostly take place before apoapsis but tend towards it for those orbits near 2:1 (although they never occur exactly at apoapsis). The reason for this pre-apoapsis burn is the constraint of targeting both the position and time of the reencounter. It is easier to do this targeting earlier in the orbit, but the change in Jacobi is greatest at apoapsis. This interplay leads to optimal burn locations in the ~170° range.

The maximum efficiency also switches from favoring short transfers to long transfers (θ goes from negative to positive) as the spacecraft orbit increases. It should also be noted that near 2:1 the values of θ are quite small, which implies only a small change off of the nominal orbits. This means that although the ratio between ΔV_∞ and ΔV_{DSM} (i.e. efficiency) is large (Figure 3.11a), the absolute values of these parameters

tend toward zero, as can be seen in Figure 3.11b. The implication of this is that despite the efficiency, many maneuvers would be necessary to achieve the desired total ΔV_∞, which add flight time.

In order to more accurately determine the characteristics of orbits very close to 2:1, we ran the program again with ephemeris steps of 0.1° and resonance steps of 10^{-4} (Figure 3.12). For values very close to exact resonance, the magnitude of ΔV_∞ goes towards zero and efficiency becomes ill-defined. For this reason the peak efficiency jumps to a lower region and gains two orders of magnitude in ΔV_∞. This trade between efficiency and ΔV_∞ magnitude (which leads to shorter flight times) is discuss later and illustrated in Figure 3.18.

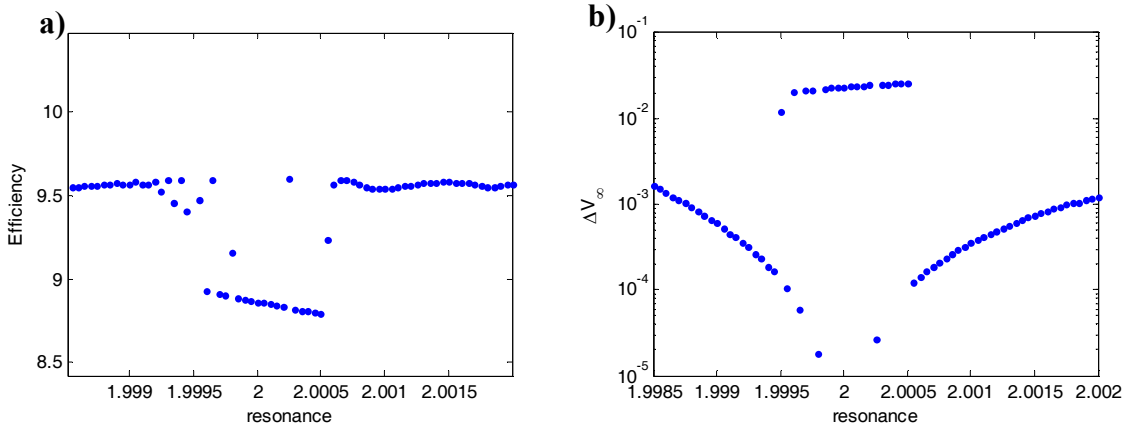

Figure 3.12. Expanded view of efficiencies (a) and ΔV∞ (b) near 2:1. Numerical difficulties occur around the integer resonance, causing the location of the efficiencies to jump to another region.

For resonances around 3:1, 4:1, etc., the trends are very similar to those in Figure 3.11 but with higher peak efficiencies. Figure 3.13 and the corresponding table shows the increase in efficiency with higher resonances. This illustrates the reason to perform leveraging maneuvers at the highest resonance possible and close to the integer.

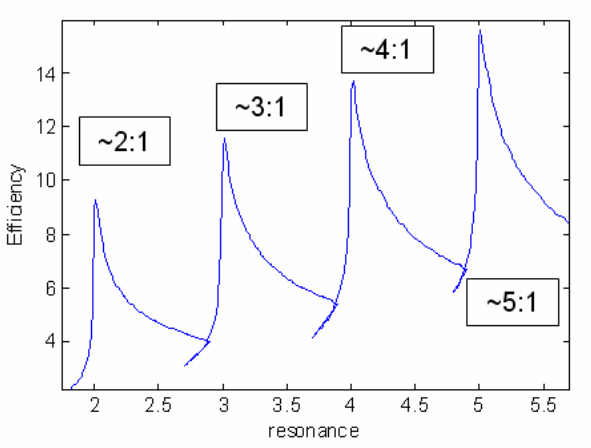

Resonance	Max Efficiency
2:1	9.55
3:1	11.80
4:1	13.95
5:1	15.98

Figure 3.13. Efficiencies of orbits with K:1 resonances along with their peak values.

Multi-Revolution Solutions

As we recall, it is possible to perform leveraging maneuvers when the spacecraft completes multiple orbits before the reencounter. The decision must then be made as to where to execute the targeting burn. The left plot in Figure 3.14 shows that orbits with $M = 1$ have higher peak efficiencies than those with $M = 2$. With the conventional method of doing leveraging maneuvers (anti-parallel at apoapsis), it is most efficient to perform maneuvers on the last orbit before rendezvous ($M = L$). This is consistent with our analysis because the first orbit of our V_∞-increasing maneuver corresponds to the last orbit of the one decreasing V_∞.

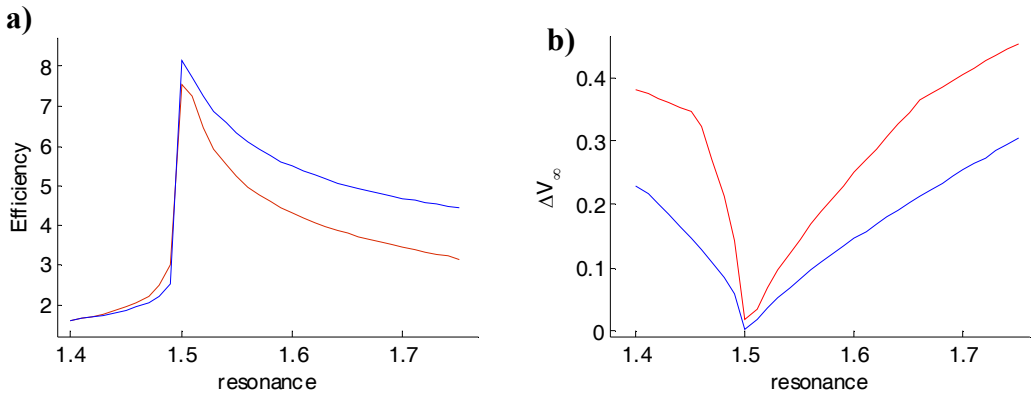

Figure 3.14. Leveraging Efficiencies around 3:2. The blue lines are 3:2(1) and red are 3:2(2). While it appears that maneuvers performed on the first orbit are more efficient (a), 2nd orbit maneuvers have a greater change in V∞ (b) and may be preferable in some instances.

The peak efficiency curves for all *K*:1, *K*:2, and *K*:3 orbits are plotted in Figure 3.15. Notice that the location of the peaks fall on a straight line.[27] We would expect that all *K*:*L* (where *K* and *L* are integers) orbits would fall on this line. If *K* and *L* are allowed to go to infinity (infinite flight time), then this peak efficiency line would be achievable for any spacecraft orbit size. The slope of the efficiency vs. resonance line gives us a tool to calculate the theoretical minimum ΔV required to reduce V_∞ to zero given infinite time, which is the topic of the next section.

[27] Due to limited resolution, the peaks must first be extrapolated to where ΔV_∞ goes to zero. It is with these values that their locations become truly linear.

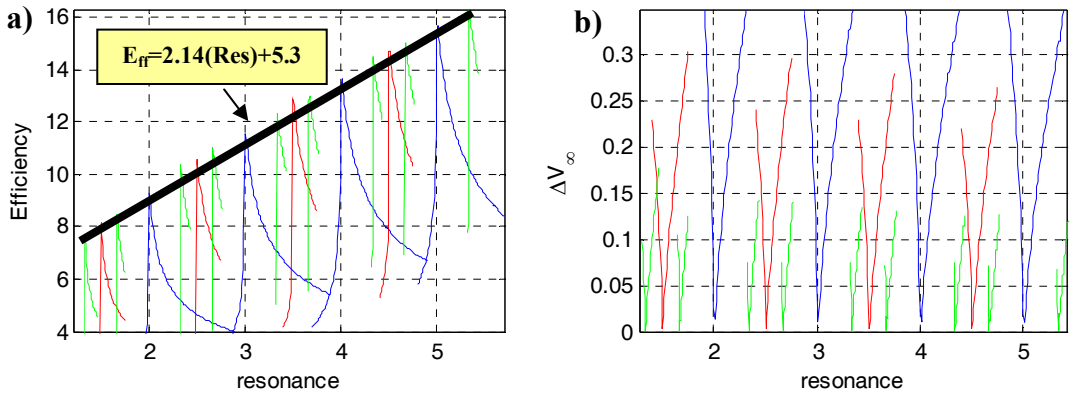

Figure 3.15. a) Efficiencies for K:1 (blue), K:2 (red), and K:3 (green) resonances. The peak efficiencies fall on a line indicating the relationship between resonance and efficiency, given by linear fit. b) ΔV_∞ goes towards zero at each point of maximum efficiency.

3.6 Theoretical Minimum ΔV

In order to calculate the minimum ΔV we first rearrange Equation 3.6 to get

$$\partial V = \frac{\partial V_\infty}{\partial Eff_{\max}}, \tag{3.7}$$

which can be integrated over $[V_{\infty,\mathrm{i}}, 0]$ (where $V_{\infty,\mathrm{i}}$ is the initial V_∞) to get the total ΔV. To do so we need an expression for the maximum efficiency ($Eff_{\max}$) in terms of a given V_∞. The line passing through the extrapolated peak efficiencies has an equation of

$$Eff_{\max} = 2.14 * \mathrm{Res} + 5.32. \tag{3.8}$$

Each value of V_∞ has a range of achievable resonances (illustrated by Figure 3.7), which can be selected by changing α. Since efficiency increases with resonance, we desire the maximum resonance, which occurs at

$$\mathrm{Re}s_{\max} = \sqrt{a_{\max}^3} = \sqrt{\left(\frac{1}{2-V^2}\right)^3} = \left[2-(1+V_\infty)^2\right]^{-3/2}. \tag{3.9}$$

Now we can write an expression for $Eff_{\max}(V_\infty)$ by substituting Equation 3.9[28] into Equation 3.8 and by defining the equation

$$Eff_{\max} = 2.14\left[2-(1+V_\infty)^2\right]^{-3/2} + 5.32. \tag{3.10}$$

The integral for the minimum ΔV can now be expressed as

$$\Delta V_{\min} = \int_0^{V_{\infty,i}} \frac{1}{Eff_{\max}} dV_\infty. \tag{3.11}$$

The integral above can be solved numerically and is depicted by the blue line in Figure 3.16. We would begin to create the trajectory to achieve this minimum ΔV by using fly-bys to bring α to zero and to maximize the resonance for the initial V_∞. The maximum resonance could be something like 186:37, but that is inconsequential since time is not restricted. On one of the 37 orbits, an infinitesimal ΔV would be applied to bring about a reduction in V_∞ as efficiently as possible. This process would then continue in infinitesimal steps until V_∞ goes to zero. The total ΔV required to reduce any V_∞ above 0.41 (but below 2.41) is 0.034. This is because the orbits above $V_\infty = 0.41$ can be made to perform their leveraging maneuvers at infinity for zero fuel.

[28] Note that $\mathrm{Res}_{\max}$ and $Eff_{\max}$ go to infinity as V_∞ approaches $\sqrt{2}$ -1 (~0.41).

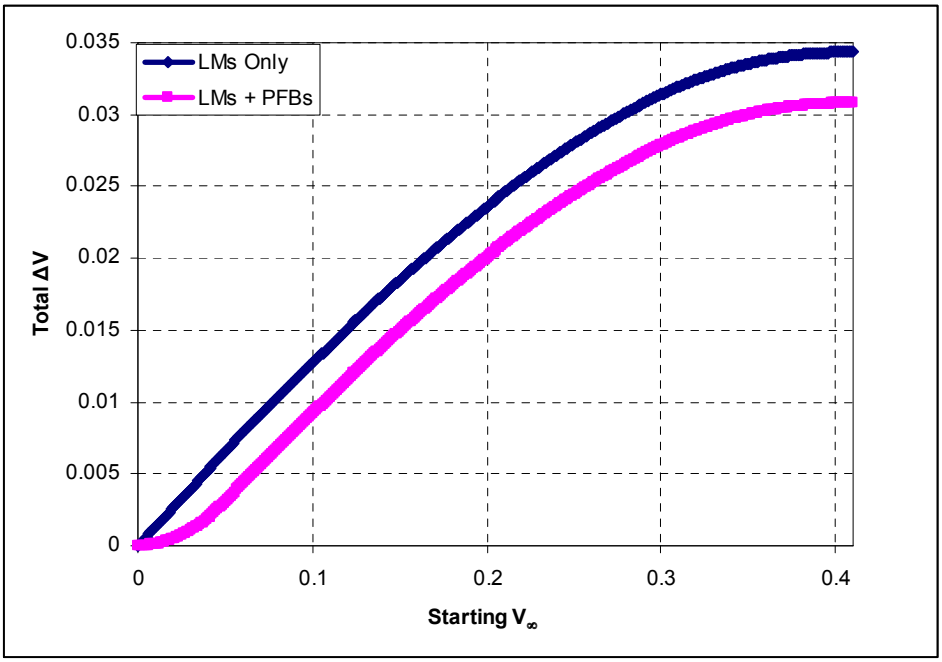

Figure 3.16. Theoretical Minimum ΔV required to reduce V_∞ to zero. The blue line uses leveraging maneuvers (LMs) only, whereas the magenta line additionally makes use of powered fly-bys (PFBs) when they become more efficient for low values of V_∞.

When V_∞ leveraging is not used, it is possible to reduce V_∞ with some efficiency by using powered fly-bys (e.g. performing a retro-burn during closest approach). We can compute the efficiency of these fly-bys (Eff_{fb}) by recalling that $V_\text{p}^2 = V_\infty^2 + 2V_\text{c}^2$, where V_p is the velocity at fly-by periapsis and V_c is the local circular velocity. If we differentiate and rearrange, we find

$$Eff_{fb} = \sqrt{\frac{V_\infty^2 + 2V_c^2}{V_\infty^2}} \,. \tag{3.12}$$

If we assume a typical value of $V_\text{c} = 0.3$ (for Titan $V_\text{c} = 1.8$ km/s = 0.32), we can plot Eff_{fb} and the efficiency of leveraging maneuvers (Eff_{LM}), as seen in Figure 3.17a. Below $V_\infty = 0.058$, powered fly-bys become more efficient. The location of this crossover point is shown in Figure 3.17b for various values of V_c, which was obtained

by setting $Eff_{LM} = Eff_{fb}$. The magenta (lower) line in Figure 3.16 uses the combined maximum efficiencies to compute the absolute minimum ΔV.

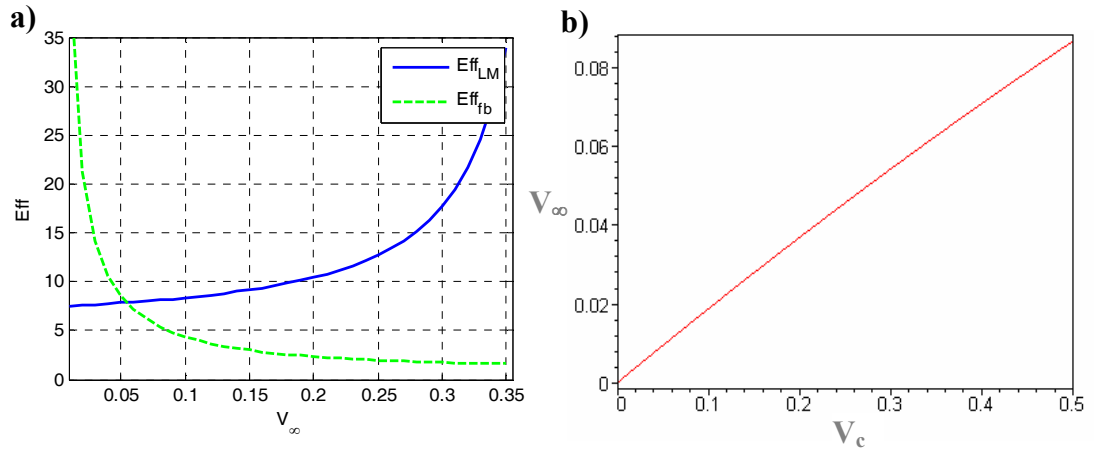

Figure 3.17. a) Maximum efficiency of leveraging maneuvers (LM) and powered fly-bys (fb) vs. V_∞ for Vc = 0.3. b) Minimum values of V_∞ required for leveraging maneuvers to be more efficient.

3.6.1 Practical Considerations

The practical application of leveraging maneuvers requires that ΔV_∞ be non-infinitesimal at the expense of lower efficiency in order to limit the total *TOF*. As demonstrated in Figure 3.11, efficiency decreases away from integer resonances as ΔV_∞ increases. This trend is depicted for various resonances in Figure 3.18. Larger ΔV_∞ steps than those corresponding to the points of maximum efficiency are required to complete a capture in a reasonable number of orbits and limit the total *TOF*. For this reason it is not always practical to perform a maneuver at the peak ν-θ pair found on the efficiency plot. A maneuver must be used that is as efficient as possible while still meeting the minimum ΔV_∞ required to achieve the next resonance desired in the tour sequence.

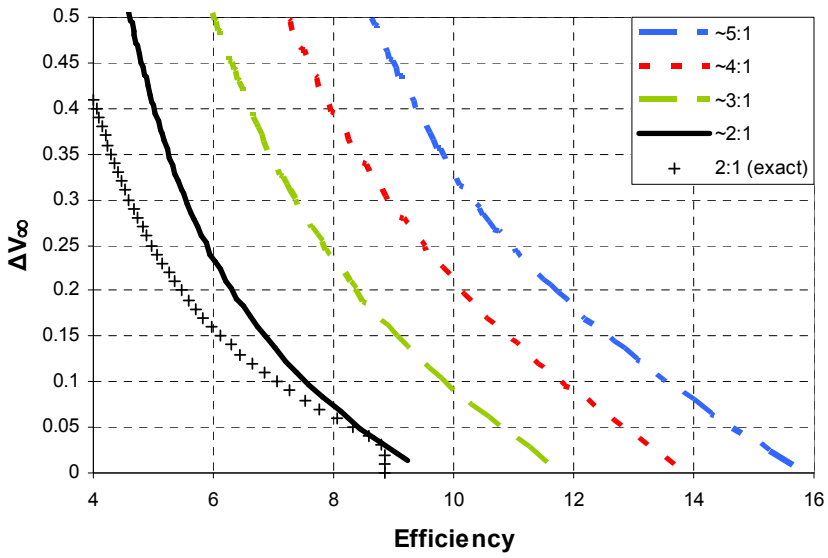

Figure 3.18. ΔV_∞ vs. Efficiency. In practice a trade must be made between efficiency and TOF. To reduce TOF, larger $\Delta V\infty$ steps must be used. This plot can be used to determine the degradation of efficiency vs. step size for various resonances.

There are two ways to increase the ΔV_∞ of a maneuver. The first is to move off the peak on the same resonance efficiency plot (Figure 3.10a) by targeting a larger θ, thus decreasing efficiency and increasing ΔV_∞ by increasing α of the encounter. The second way is to increase the resonance (which is targeted during the previous fly-by) until the peak efficiency point of the new plot also meets the required ΔV_∞. The second method leads to a greater efficiency for the same ΔV_∞ but is much more complex to simulate. The efficiency curves in Figure 3.18 were computed using the second method. If the first method is used for a 2:1 orbit the efficiency falls off at a greater rate as shown by curve delineated by '+'s on the left side of the plot.

The total *TOF* of a tour is calculated by adding all the *K* values (from the *K:L* maneuvers) and multiplying by the period of the gravity-assist body. The actual *TOF* would vary slightly due to the maneuvers' effect on K, but for simplicity we sum the

integer values. With this in mind, it is preferable to use *K*:1 resonances as much as possible since they are ~50% more efficient than *K*:2 resonances of equivalent duration and even more efficient than for larger L values.

3.7 Global Search Methodology

An endgame tour sequence begins with a spacecraft in an elliptical orbit about the central body and in some (usually large) resonance with the gravity-assist body. A series of reducing resonances are targeted using alternating fly-bys (both un-powered and powered) and V_∞ leveraging maneuvers until $V_\infty = 0$. For our purposes we reverse the process by beginning with $V_\infty = 0$ and work outwards towards the large resonance. As an arbitrary metric, we chose an end point of a 6:1 orbit with $V_\infty = 0.3027$ and $\alpha = 0$. The total ΔV and *TOF* for the tour sequence is accumulated for comparisons.

To begin, a powered fly-by (more efficient for low V_∞'s) is used to boost the spacecraft to a starting resonant orbit. Then a leveraging maneuver is performed around apoapsis to target the next fly-by at a new location with a new, higher V_∞ corresponding to the next resonance in the desired sequence. The value of the V_∞ being targeted is calculated by

$$V_{\infty,new} = \sqrt{2 - R_{new}^{-2/3}} - 1. \tag{3.13}$$

The act of performing the leveraging maneuver also brings the orbits out of tangency, increasing α at the new encounter which can be approximated[29] by

$$\alpha = \cos^{-1}\left[\frac{1 - V_{\infty,new}^2 - R_{new}^{-2/3}}{2V_{\infty,new}}\right]. \tag{3.14}$$

Equations 3.13 and 3.14 are each just rearrangements of Equation 3.5 except that Equation 3.5 has α set to zero. We bring these equations into agreement and achieve the new resonance by using the fly-by to bend the V_∞ vector and to rotate α back to zero. If α is greater than δ_{max}, an intermediate α and R must be chosen as a "phasing orbit" until α can be reduced to zero on a subsequent fly-by. Phasing orbits increase the tour duration but not the total ΔV. Sometimes multiple phasing orbits may be required. Once the orbits are again tangent, the process is repeated to target the next resonance until the desired end point is achieved.

3.7.1 Simulations

Endgame tours can be constructed by a limitless number of combinations of resonance orbits, leveraging maneuvers, fly-bys, phasing orbits, etc. One such sequence constructed "by hand" is depicted in Table 3.2 below and on the V_∞ Plane in Figure 3.8, (which is repeated as Figure 3.19 below for convenience). This tour uses the following resonant orbits: 2:1, 3:1, 4:1, 5:1, 6:1. The tour begins with a powered fly-by to boost the spacecraft to a 2:1 orbit. Around apoapsis a leveraging maneuver is applied to change the V_∞ of the next encounter from 0.171 to 0.233. The maneuver

[29] This is an approximation because the leveraging maneuver also changes the resonance by a few percent thus making R not a constant in the derivation. During our simulations we calculate the true value of α numerically.

also causes α to go from 0° to 48.6°. This is illustrated by following the 2:1 resonance line in Figure 3.19 starting at α = 0° and $V_\infty = 0.17$ up until the line crosses $V_\infty = 0.233$ (which corresponds to a 3:1 orbit when α = 0) at α = 48.6°.

Table 3.2. Maneuver Sequence for an Example Tour. This tour has a resonance sequence of 2:1, 3:1, 4:1, 5:1, 6:1. Maneuvers consist of Δ*V*'s (DV), which are performed during fly-by (PFB) or as a leveraging maneuver (VILM), and fly-bys (FB). Values for V_∞ (initial and final), resonance (initial and final), efficiency, Δ*V*, times, α, and δ_{max} are given for each maneuver.

Maneuver	Method	$V_{\infty,i}$	$V_{\infty,f}$	ΔV_∞	R_i	R_f	*Eff*	**ΔV**	**Time**	α	δ_{max}
DV1	PFB	0	0.171	0.171	-	2	5.17	**0.0330**	**0**	0	98.2
DV2	VILM	0.171	0.233	0.062	2	1.96	8.00	**0.0078**	**1**	48.6	77.3
FB1	FB	0.233	0.233	0	1.96	3	0	**0**	**1**	0	77.3
DV3	VILM	0.233	0.266	0.034	3	2.97	11.11	**0.0030**	**1.5**	33.1	68.1
FB3	FB	0.266	0.266	0	2.97	4	0	**0**	**1.5**	0	68.1
DV4	VILM	0.266	0.288	0.021	4	3.98	13.34	**0.0016**	**2**	26.1	62.8
FB5	FB	0.288	0.288	0	3.98	5	0	**0**	**2**	0	62.8
DV5	VILM	0.288	0.303	0.015	5	4.98	15.28	**0.0010**	**2.5**	24.2	59.4
FB6	FB	0.303	0.303	0	4.98	6	0	**0**	**2.5**	0	59.4
TOTALS								**0.04638**	**14**		

For this V_∞ level, $\delta_{max} = 77.3°$, which means that a single fly-by is sufficient to return α to zero and to enter the 3:1 orbit. Another V_∞ leveraging maneuver is performed near apoapsis (optimized using an efficiency plot) to pump V_∞ up to 0.266 (which is equivalent to a 4:1orbit when α = 0). This causes α to increase to 33.1°, which is again less than the new δ_{max} of 68.1°. Therefore, a phasing orbit is not required before the 4:1 orbit is achieved during the next fly-by. This process is repeated to reach 5:1, and likewise 6:1. The total time to reach the end point is found by adding the K values, excluding 6:1, to give 14 time units (e.g. 223 days for Titan). The total Δ*V* for all the maneuvers is 0.0464 velocity units (e.g. 260 m/s for Titan) to go from $V_\infty = 0$ to 0.3027.

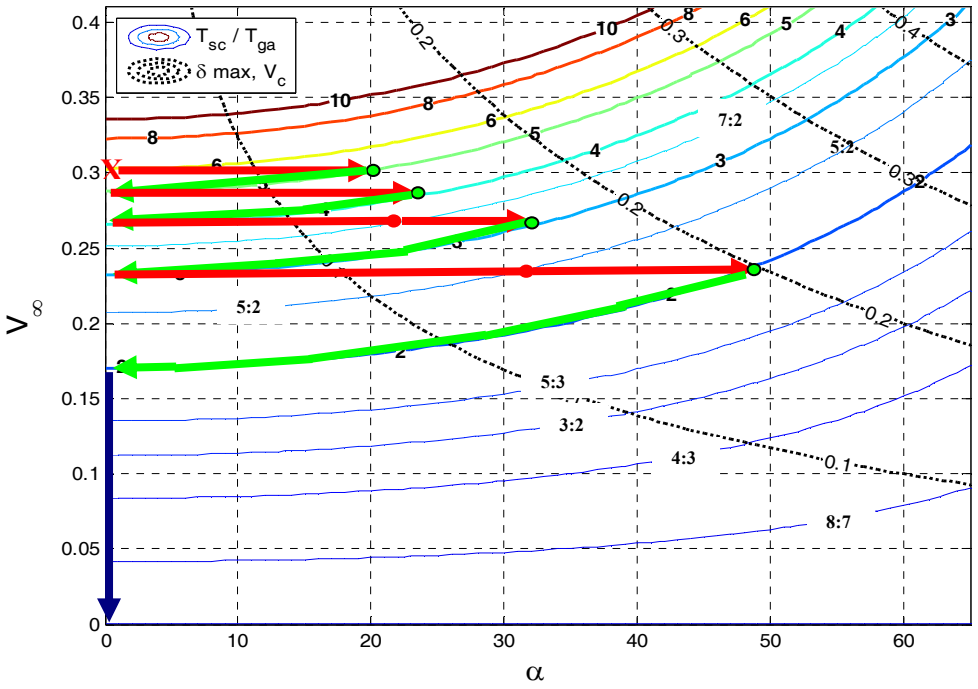

Figure 3.19. The V_∞ Resonance Plane. Colored contours represent lines of resonance for orbits of a given V_∞ and α. The dashed black lines show the maximum turn angle, δ_{max}, as a function of local circular velocity, V_c, and V_∞. One potential pathway is illustrated with fly-bys, leveraging maneuvers and powered fly-bys represented by red, green, and blue arrows, respectively.

Using different sequences from the infinite possibilities of resonances and maneuvers result in new combinations of ΔV and *TOF*. Sequences that increase *TOF* do not necessarily decrease ΔV because some resonances and combinations are not as efficient as others. However, it is reasonable to suspect that the most efficient sequences would follow a general trend of decreasing ΔV as *TOF* increases.

In order to determine the sequences that are most efficient for a given *TOF*, we set up a pseudo-global search for all the combinations that result in increasing V_∞ from zero to 0.3027 (6:1). The reason that it is not a true global search is that resonances used need not be rational numbers leading to an infinite number of

pathways. To thoroughly explore the trade space, we set up a Monte Carlo-like algorithm that uses random number generators to select the next maneuver of a sequence from a range or set of possibilities.

The algorithm begins by assuming that $V_\infty = 0$ (parabolic orbit) and $V_c = 0.3$ (Titan-like). A random number generator selects K and L values such that $K/L = R > 6$. They are also restricted to values less than 24, with lower values being more heavily weighted in order to favor shorter flight times. The required ΔV is then calculated for a powered fly-by to reach the generated R.

Next the number generator selects a resonance and associated V_∞ to target. A V_∞ leveraging efficiency plot such as the one in Figure 3.10a is generated for the initial resonance. The most efficient ν-θ pair that also results in the desired ΔV_∞ is then selected as the next leveraging maneuver. The associated ΔV and duration (~K) is added to the totals, and α for the next encounter is calculated. If α is less than δ_{max}, then the fly-by is used to bend α back to zero, and the process is repeated. If α is greater than δ_{max}, then a choice is made whether to target a phasing orbit, use a powered fly-by, or to begin the next leveraging maneuver from a non-tangential orbit (using the smallest α achievable with the one fly-by).

If a phasing orbit is used, then a script is called that selects the intermediate resonance to use from the range dictated by α and δ_{max}. A heavier weight is placed on resonances with lower K values as well as those that use a larger δ so that α can reach zero in as few phasing orbits as possible. This sequence selection and calculation process continues until $R = 6$ and $\alpha = 0$. The total ΔV, TOF, and resonance sequence are output for each iteration.

The algorithm just described can be tailored to obey one of three overarching rules: (1) No Crossing δ_{max} (NX) - the use of phasing orbits is disallowed by requiring that next target resonance in a sequence does not cause α to cross the δ_{max} line for the given value of V_c on the plot shown in Figure 3.19. This means that the orbits can always return to tangency at the cost of smaller ΔV_∞ steps and more leveraging maneuvers. (2) Phasing Orbits (PH) - crossing of the δ_{max} line is allowed but requires that phasing orbits be used until α returns to zero before another leveraging maneuver can be performed. The sequence given in Table 3.2 is an example of this rule. (3) Non-Tangential (NT) - the third overarching rule is opposite from the second one in that no phasing orbits are allowed and leveraging maneuvers are performed from orbits that begin from a non-tangential state.

3.8 Results

Our Monte-Carlo simulations generated tens of thousands of unique paths, most of which are not useful for practical tours as they are either extremely long in duration, less effective than a direct powered fly-by, or are much less efficient than an alternate sequence of an equivalent duration. Figure 3.20 is a plot of ΔV vs. *TOF* for all the simulated cases with $V_c = 0.3$. The lowest total ΔV across the range of *TOF*s creates a Pareto front indicated by the solid line. This front represents the trade between fuel and duration in the tour design process.

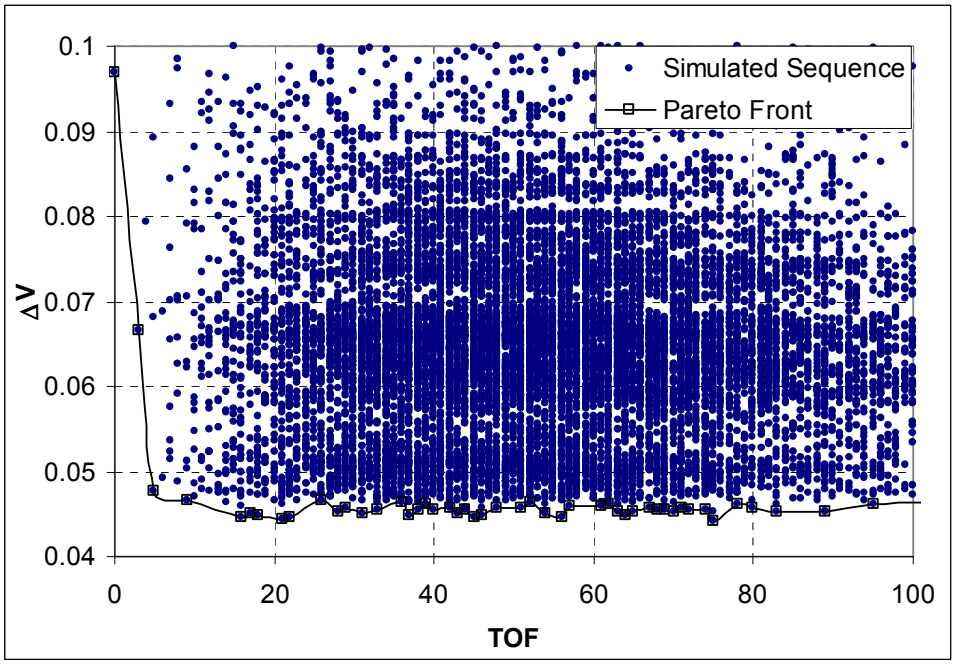

Figure 3.20. ΔV vs. TOF from global search for Vc = 0.3. Each point represents a sequence generated from Monte Carlo simulations. The black line represents a Pareto front comprised of the most efficient sequences. Note the rapid drop in ΔV for the shorter TOFs followed by a flattening after about 5 time units.

The shortest *TOF* sequences and their associated ΔV's are listed in Table 3.3. The quickest method is to perform no tour at all and boost directly to a 6:1 orbit using a large ΔV burn at the beginning. Recall that powered fly-bys are only more efficient than leveraging maneuvers for small values of V_∞ (and hence, resonances). Therefore, it is possible to increase overall efficiency by using a smaller powered fly-by first, followed by a series of leveraging maneuvers. To keep the *TOF* low, it is best to boost to an intermediate resonance with L = 1 (e.g. 2:1, 4:1). From there higher resonances with L = 1 only are targeted until 6:1 is reached. Various permutations of this strategy lead to the 7 fastest sequences.

Table 3.3. The 10 Shortest TOF Sequences for $V_c = 0.3$. Parentheses represent phasing orbits and 'NT' indicates a resonance that started out non-tangentially (i.e. $\alpha > 0$).

TOF	ΔV	Sequence
0	0.0969	Direct Powered Fly-by
3	0.0665	3:1, 6:1
4	0.0794	4:1, 6:1
5	0.0477	2:1, 3:1, 6:1
5	0.0682	5:2, 6:1
6	0.0493	2:1, 4:1, 6:1
6	0.0687	3:2, 3:1, 6:1
7	0.0515	2:1, 5:1, 6:1
7	0.0522	2:1, 5:1 NT, 6:1
7	0.0537	2:1, (5:1), 6:1

The 10 lowest total ΔV sequences found in the Monte-Carlo simulations are shown in Table 3.4. The resonances that comprise each sequence are listed with leveraging maneuvers occurring on each. The lowest ΔV sequence found requires 0.0442 velocity units, or 55% less than the direct boost. It does, however, take 75 time units (e.g. ~4 years @ Titan). It makes use of long-duration resonances, including 15:4 and 23:4. The other sequences in the table have similar total ΔV's with flight times ranging from 16 to 64 time units. Note that none of the sequences required the use of a phasing orbit or non-tangential maneuver. This is due to the relatively large V_c value. For lower values more and more phasing orbits and non-tangential leveraging are required as α often crosses the δ_{max} line.

Table 3.4. The 10 Lowest Total ΔV Sequences for $V_c = 0.3$. Each resonance in the sequence includes a leveraging maneuver.

Time	ΔV	Sequence
75	0.0442	5:3, 7:4, 2:1, 3:1, 15:4, 4:1, 5:1, 11:2,
21	0.0445	7:4, 2:1, 3:1, 4:1, 5:1, 6:1
45	0.0446	7:4, 2:1, 3:1, 4:1, 24:5, 5:1, 6:1
22	0.0446	5:3, 7:4, 2:1, 3:1, 5:1, 6:1
56	0.0447	7:4, 2:1, 3:1, 4:1, 24:5, 5:1, 11:2, 6:1
16	0.0447	7:4, 2:1, 3:1, 4:1, 6:1
18	0.0448	9:5, 2:1, 3:1, 4:1, 6:1
37	0.0449	9:5, 2:1, 3:1, 19:5, 4:1, 6:1
46	0.0449	7:4, 9:5, 2:1, 21:8, 3:1, 4:1, 6:1
64	0.0449	7:4, 2:1, 19:7, 3:1, 4:1, 24:5, 5:1, 6:1

The most significant trend in the Pareto front is that the minimum ΔV is reached quickly and is followed by a flattening where increasing *TOF* does little to affect the fuel requirement. This rapid decrease followed by a flat line creates an "elbow" in the curve where the most appealing sequences lie. It is possible to reduce the ΔV requirements by around 50% for a relatively small increase in *TOF* at this "elbow". Increasing duration beyond this point results in little to no gain, contrary to intuition. One would expect the total ΔV to continue to approach the theoretical minimum (about 20% lower in this case), but this does not occur. In fact, simulated sequences that take 100-300+ time units actually started to increase in total ΔV. One possible explanation for this trend is the decreasing width of the efficiency peaks (see Figure 3.13) with increasing K and L values. This means that leveraging maneuvers that do not fall exactly on the peak (which is the norm in practice) have efficiency far below the theoretical maximum for long duration sequences.

To this point we have primarily discussed simulation results for V_c = 0.3 because this work is especially meant to be applicable to the Titan-Saturn system, where there is only one significant body available for gravity assists and $V_{c,Titan}$ = 0.32. Changing V_c dramatically alters the control the gravity-assist body has on the V_∞ vector and hence, limits (or enables) orbital parameters after a single fly-by. The points and Pareto front in Figure 3.20 are a conglomeration of all the sequences generated, allowing for all three of the overarching rules described in the previous section. In this case, where V_c = 0.3, the first rule, NX (or no crossing of the δ_{max} line), is almost always the most beneficial as α rarely approaches the δmax line. However, if we break the front into those sequences that use phasing (PH), non-tangential maneuvers (NT), and a mix for V_c = 0.2, we can see in Figure 3.21 that each strategy can be equally beneficial for reducing the total ΔV and creating an efficient sequence with none being clearly better than the others.

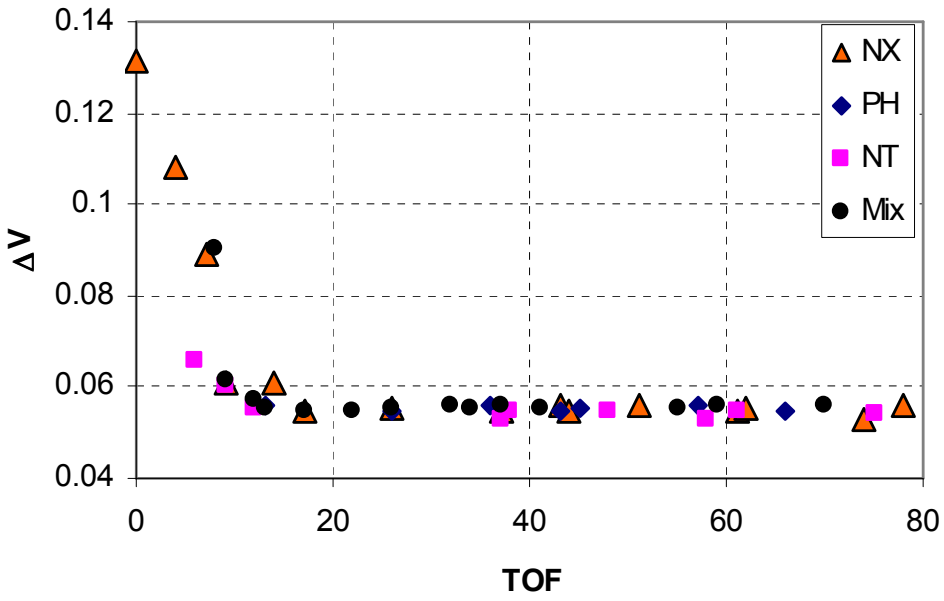

Figure 3.21. Pareto front broken into the 3 overarching rules for $V_c = 0.2$: NX – Sequences do not cross the δ_{max} line (α always returns to zero), PH – Phasing orbits are used when $\alpha > \delta_{max}$, NT – Non-tangent orbits are used when $\alpha > \delta_{max}$.

For lower values of V_c, phasing and non-tangential sequences become dominant. For example, a sequence that is not permitted to cross the δ_{max} for $V_c = 0.1$ would have to take many small steps and "zigzag" close to the $\alpha = 0$ line, whereas phasing or non-tangent maneuvers would allow much more freedom for more efficient sequences. Increasing V_c also raises the crossover point where powered fly-bys are more efficient than leveraging maneuvers, making them more useful to higher values of V_∞. Figure 3.22 plots the Pareto fronts for V_c's of 0.1 (e.g. Europa), 0.2 (e.g. Callisto), 0.3, and 1.6 (e.g. the Moon). Note the common trend to fall to a near minimum ΔV sharply and then plateau. For $V_c = 1.6$, the decrease is only around 10% and occurs very quickly, whereas the drop is almost 50% for the others with the "elbow" moving to longer *TOF*s for decreasing V_c's.

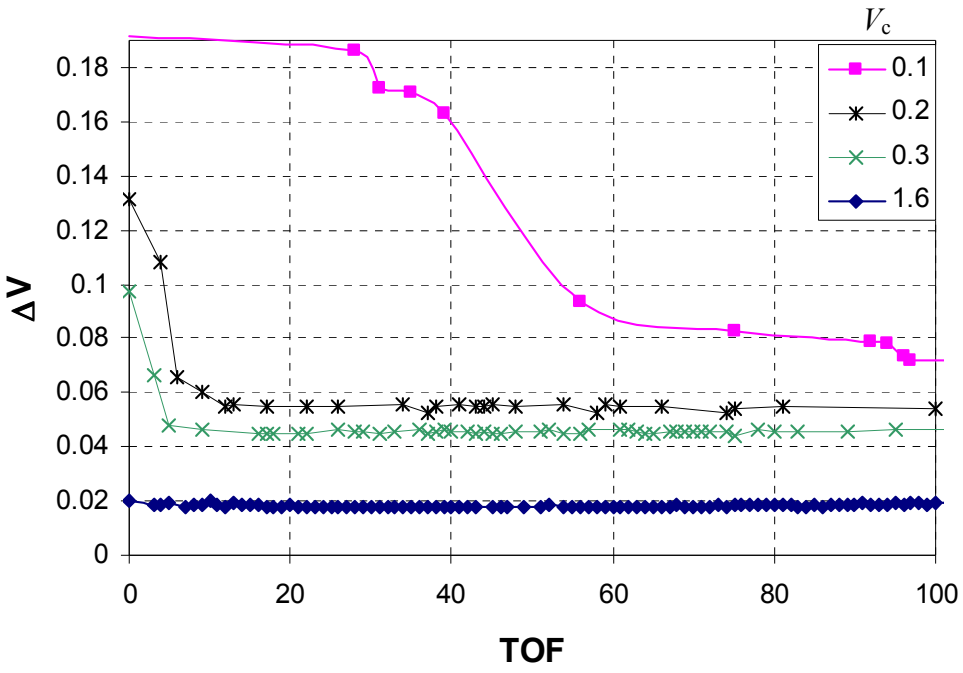

Figure 3.22. Pareto fronts for various values of Vc.

The Monte-Carlo algorithm also allowed for the use of powered fly-by's at any point in the sequence if they proved to be beneficial. For example, they can be used to raise a resonance from 8:3 to 3:1 or to help bend α beyond the δ_{max} of an unpowered fly-by. As it turned out, these types of maneuvers were very costly and resulted in sequences that fell well above the Pareto front. Theoretically, a powered fly-by should not be used above V_∞ = 0.06 (6:5 resonance) for V_c = 0.3, as this is where leveraging becomes more efficient. But in practice, sequences that started off below V_∞ = 0.17 (2:1) were required to use many large L-value orbits (e.g. 9:7, 7:5). This is because the resonance curves on the V_∞ Plane are relatively flat in that region and many intermediate resonances are required to achieve the sufficient ΔV_∞. As was noted previously, orbits with large L values have narrow efficiency peaks and result in sub-optimal efficiencies in practice.

3.9 Conclusion and Future Work

V_∞ leveraging is a useful tool in the design of planetary moon endgame strategies. If applied properly it is possible to significantly reduce the total ΔV required to send an orbiter to a planetary moon such as Titan. In this dissertation we present theoretical calculations that show that the total ΔV required can be up to 10 times or more the change in ΔV_∞. While the theoretical minima require infinite durations, they do serve to illustrate a lower bound on the fuel required to place a spacecraft into a captured orbit. As the V_∞ decreases, leveraging maneuvers become less and less efficient. Below a certain point, it was shown that powered fly-bys become a more efficient means of V_∞ reduction.

In addition, we have developed tools to construct, map, and analyze sequences of leveraging maneuvers and to compare them to the theoretical minimum. The reduction in fuel requirements comes at the expense of added flight time. Tens of thousands of sequences were generated using a Monte-Carlo type simulation and the total ΔV and *TOF* pairs were accumulated. By plotting these pairs we were able to generate a Pareto front of most efficient sequences for a given flight time.

Reducing a 6:1 orbit to $V_\infty = 0$ using a direct burn during fly-by would require 0.097 velocity units, whereas an infinite series of fly-bys and leveraging maneuvers (theoretical minimum) would reduce the total ΔV required to 0.028, a savings of over 70%. Since infinite missions are not possible, it is helpful to the mission designer to know that it is possible to reduce the total ΔV by 50% with a TOF of only 5-10 time units. Increasing the mission duration further does not result in significant reductions.

The V_∞ Sphere and V_∞ Plane are useful design tools in that they allow the designer to quickly see what types of orbits are possible given a set of input parameters. Post fly-by orbits can be targeted by noting the change of α required on the V_∞ Plane. Sequences of leveraging maneuvers and fly-bys can be plotted as points on the map.

The maneuver sequences detailed in this dissertation are restricted to orbits confined to the plane of the gravity-assist body and are very theoretical in nature. In practice planetary tours make use of inclined orbits, fly by other moons, and must take into account many other factors. Because of this, the more "optimal" tour sequences generated here are not necessarily what would be used in true mission design. However, the tools and results are instructive for preliminary analyses and for understanding the trends that lead to optimal tour design.

4 Hyperbolic Periodic Orbits

4.1 Introduction

Following the success of the Galileo and Cassini missions to the Jovian and Saturnian system, respectively, there has been much talk and planning for a dedicated orbiter mission to one of the moons of interest, such as Titan, Europa, or Enceladus. Trajectories of such orbiters typically employ multiple gravity assists during interplanetary flight and elaborate and lengthy tours in the planetary system in order to reduce fuel requirements before the final orbital insertion. Such tour design is a complicated and time consuming process. However, recent studies have shown the usefulness of V_∞ leveraging maneuvers in the reduction of fuel requirements, and as a result, tools for rapid implementation have been developed (Campagnola et al., 2010; Woolley and Scheeres, 2010). Endgame tours typically make use of alternating leveraging maneuvers and gravity assists at the target moon to decrease resonance towards unity and ultimately capture (Ross and Scheeres, 2007). However, while leveraging is very efficient for higher resonances, it becomes less so at lower resonances and can require long flight times.

In the previous chapter, sequences of leveraging maneuvers were designed using linked-conics for rapid calculations with reasonable accuracy. In the 2-body problem (2BP), hyperbolic excess velocity (V_∞) at the target moon is a constant in the

absence of perturbations or leveraging maneuvers, much like the Jacobi constant in the 3-body problem (3BP). In the first section, we review the mathematical relationships between integrals of motion in the 2BP, planar restricted 3BP (PR3BP), and Hill's problem.

Since gravity assists and the transition to gravitational capture are essentially expressions of third body effects, it makes more sense to analyze them using three-body techniques. Our previous work on leveraging sequences ended when $V_\infty = 0$, which corresponds to a parabolic orbit or the limit of gravitational capture in the patched 2BP. However, relationships between the Jacobi and V_∞ yield the possibility of bound, periodic, or quasi-periodic orbits with a positive V_∞. If such orbits exist, then they would amount to hyperbolic orbits in the 2-body sense yet be bound to the vicinity of the secondary. Targeting a "hyperbolic periodic" orbit during the final phase of a leveraging maneuver sequence would result in a lower required insertion ΔV.

In a series of papers, Hénon (1965, 1969, 1970) classified families of planar periodic orbits in the restricted 3BP and explored their limits as the Jacobi goes to $\pm \infty$. A few families continue to exist well into the realm of positive V_∞'s. Distant retrograde orbits exist for all values of V_∞ in Hill's approximation, but they grow ever distant from the primary, they do not exhibit stable and unstable manifolds, and they are difficult to target. Lyapunov and direct quasi-periodic orbits also exhibit positive V_∞'s, but the radius of closest approach goes towards zero as energy increases. Depending on the normalized radius of target body, minimum allowable altitude orbits still yield relatively high V_∞ values.

In this chapter the limits and usefulness of hyperbolic periodic orbits are explored along with their application to the endgame problem. Orbits are generated using a single shooting method in the PR3BP and integrated into the final phase of leveraging sequences found in Chapter 3. Results are scaled as to be applicable to most systems, but are applied to the Titan-Saturn system where appropriate.

4.2 Families of planar periodic orbits with positive V_∞'s

Placing an orbiter directly into a scientific[30] orbit about a planetary moon can be prohibitively expensive fuel-wise, often requiring thousands of m/s in ΔV. That is why typical orbiter mission designs usually include an extensive (months to years) tour about the planet, making use of gravity-assists and strategically placed maneuvers in order to reduce the V_∞ at the target body (Campagnola and Russell, 2010a; Ross and Scheeres, 2007; Johannesen and D'Amario, 1999). When V_∞ is sufficiently low, a capture maneuver is performed to place the spacecraft in an orbit (often loosely) bound to the target moon. Using patched 2BP dynamics, V_∞ must, by definition be reduced below zero. However, if third-body perturbations are taken into account, periodic orbits exist which exhibit positive V_∞'s in the 2-body sense. These orbits arise from the 3BP approximation and can be related to the 2BP using the relationships detailed in the previous section. These "hyperbolic periodic" orbits have higher energies than traditional capture orbits and therefore require less fuel to achieve.

[30] Usually low, circular, and near-polar.

Periodic orbits in the 3BP have been studied extensively by many researchers, more notably Poincare (ed. 1993), Szebehely (1967), and Hénon (1969). There are a number of methods to find periodic orbits, both specific solutions and continuous families. One common approach involves systematically scanning the phase space immediately surrounding a known solution. Initial conditions are propagated, and the trajectory is checked for conditions of symmetry which indicate periodicity. If conditions are nearly met, a differential corrector method is used to converge on the exact solution. The new solution is then used as the seed, and the process is repeated to find all the solutions of one family within a specified range. Often times families intersect at bifurcation point and care must be taken to distinguish between the two. A second approach to finding periodic orbits makes use of a brute force global scan over a grid of parameters to find those initial conditions that result in conditions of periodicity (Russell, 2005). This second method is much more computationally expensive, but modern computers have made it practical and fruitful.

In this dissertation we are interested in finding those periodic orbits which have higher energies so as to be hyperbolic in the 2BP and require less fuel to achieve. Hénon found five families of simple periodic (crossing the *x*-axis only twice) planar orbits which he denotes: *a, c, f, g*, and *g'*. Families *a* and *c* are Lyapunov orbits about the libration points L2 and L1, respectively. Family *f* represents retrograde orbits about the secondary, while *g* and *g'* originate as simple prograde orbits and evolve to more complex ones with four x-axis crossings as energy

increases. Each of these families can be extended to Γ[31] = -∞, where $\Gamma < 0$ corresponds to a positive V_∞. However, for families *a, c, g,* and *g'*, the minimum approach radius, r_p, goes to zero as this limit is realized. For the moons listed in Table 2.1, Γ becomes negative before the normalized radius is reached, indicating the existence of positive V_∞ periodic orbits.

In order to generate these periodic orbits, we set up a simple grid search for orbits which originate on the *x*-axis close to the secondary with $\dot{x}_0 = 0$. A single shooting method (Howell, 1984) was employed to vary $\dot{y}_0$ until the subsequent *x*-axis crossing was again perpendicular, indicating a symmetric periodic orbit (see Section 2.2.8). The equations of motion of the PR3BP (Equation 2.40) were used with the value of μ from Titan.[32] The *x* value was increased until the orbits no longer had positive V_∞ values. Retrograde orbits, which comprise family *f*, increase in V_∞ as the distance from the moon increases. However, because these orbits are highly stable, it can be difficult to transfer from them to a science orbit. Lam and Whiffen (2005) and Demeyer and Gurfil (2007) describe of the use of Lyapunov orbits as a transfer mechanism.

Orbits generated are characterized by their family and by the point of closest approach which is given in Titan radii (TR) so as to readily illustrate the actual flyby distance and to indicate if a collision occurs. One Titan radius is equal to 0.0021 LU, which is very similar to the scaled radii of Europa and Ganymede. Other moons'

---

[31] Recall that $\Gamma = -2*J_H$, which is the Jacobi constant in Hill's Problem

[32] All the plots throughout this dissertation will use $\mu_{\text{Titan}} = 2.37\text{e-}4$, but the results will be similar for nearly all of the outer-planetary moons as $\mu << 1$.

radii can be deduced from the data in Table 2.1. In practice, a radius of around 1.1 TR approximates the minimum allowable flyby distance.

Low-Jacobi, high-energy Lyapunov orbits are roughly kidney-bean shaped with a hyperbolic component near the secondary and with a distant component similar to a large prograde or retrograde orbit. Family *a*, L2-centered orbits, and family *c*, L1-centered orbits, for a few energy levels are shown in Figure 4.1a and b. Note that L2 orbits are prograde at the point of closest approach and retrograde at the opposite *x*-axis crossing, whereas the reverse is true for L1 orbits. Also note that L1 orbits are larger for equivalent TR levels. The orbits in family *g* in Figure 4.1c start out as a prograde orbit close to the secondary, but there is twist in the orbit both above and below which causes the direction to be retrograde for the majority of the orbit. These orbits may be of interest since a close fly-by occurs on both the near and far sides of the moon.

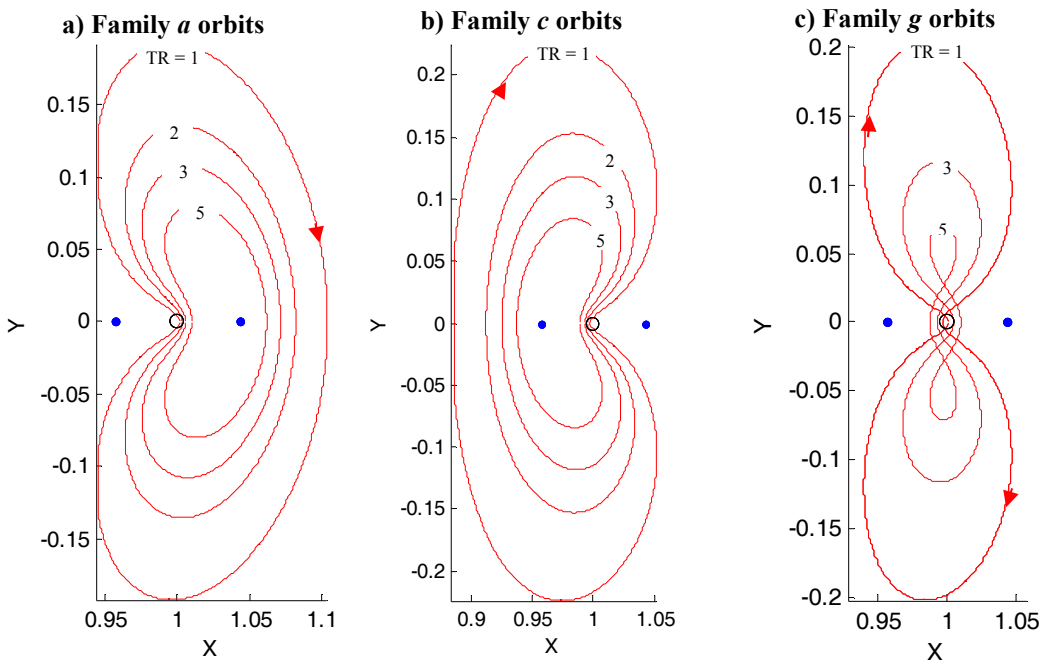

Figure 4.1. Plots of planar periodic orbits with close fly-by's of the secondary and positive V_∞'s. a) Orbits in the *a* family – L2 Lyapunov, b) *c* family orbits – L1 Lyapunov, c) Family of *g* orbits which originate as prograde orbits about the secondary. TR = Titan Radii.

Family *g'* bifurcates from *g* near the Jacobi value for L1 and L2. At high energy levels these orbits have a prograde (*g'2*) or retrograde (*g'1*) close passage of the secondary and behave similarly to families *a* and *c*, with the exception of an extra loop around m_2. They are depicted in Figure 4.2a and b. The distant retrograde orbits, as they are most commonly called, of family *f* are show in Figure 4.2c. They are very stable and increase in V_∞ as they increase in size. In the PR3BP approximation they exist to infinity, however, they become less useful as capture orbits as they grow to be very far from the secondary.

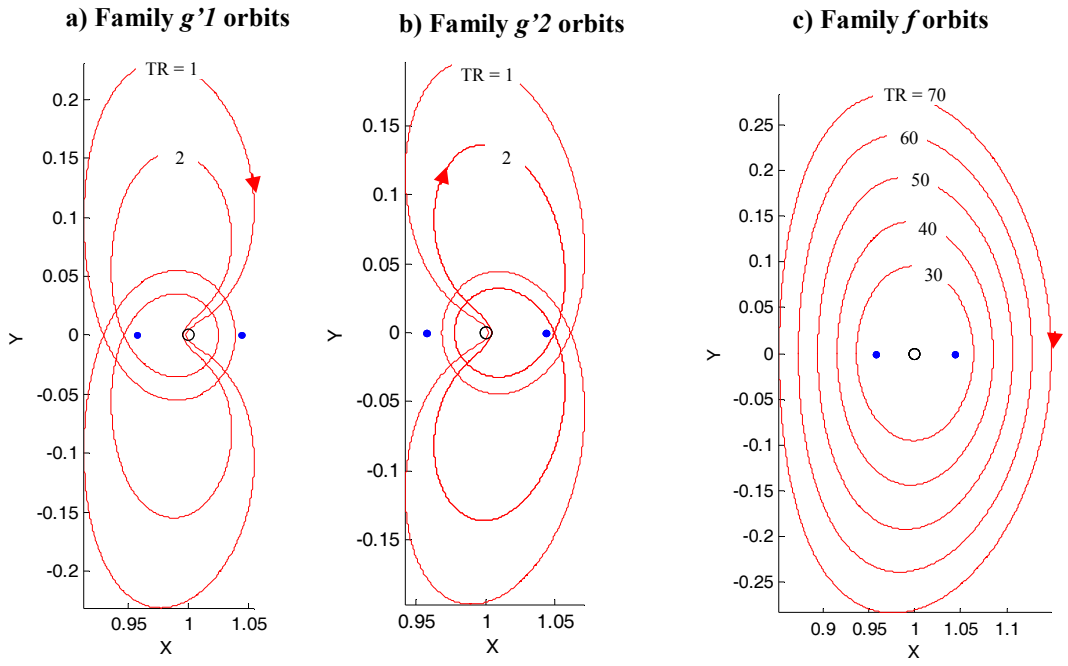

Figure 4.2. Planar periodic orbits with positive V_∞'s. a) Orbits in the g'1 family – similar to family c about L1 with two extra x-axis crossings, b) g'2 family orbits – L2 version of g'1, c) Family of f orbits which are retrograde, stable, and increase in V_∞ as distance from m_2 increases.

Parameters for a few hyperbolic periodic orbits are given in Table 4.1. The ephemeredes of these orbits, generated in the 3BP, can be converted to inertial 2BP values using Equation 2.72. This allows us to calculate the V_∞ in the 2-body sense throughout the orbit and then compare it to the approximation derived in Equation 2.83. The normalized V_∞ in the 2BP is given by

$$v_{\infty,2b} = \sqrt{\dot{x}_{i,2}^2 + \dot{y}_{i,2}^2 - \frac{2\mu}{\sqrt{x_{i,2}^2 + y_{i,2}^2}}}\,. \tag{4.1}$$

Table 4.1 gives the parameters for periodic orbits that just graze Titan's surface, ten percent above the surface (corresponding to closest allowable approach), and for a few Titan radii out until the orbits are no longer hyperbolic. This is true for all the orbits except the distant retrograde orbits of family f, which do not pass near Titan and are increasingly hyperbolic. Notice that the point where $V_{\infty,3b}$ goes to zero

occurs at different distances for each family. The V_∞ value for grazing (TR = 1) orbits varies as well. This is illustrated by the plot in Figure 4.4. This plot is comparable to figure 1 in (Hénon, 1969), zooming in around the origin and replacing ξ with x and Γ with J. Each family curve would approach $x = 0$ as J decreases except that the curves end where a collision occurs. The vertical line corresponds to $V_\infty = 0$ at $J = 3/(1-\mu)$. Note that the Lyapunov orbits (a and c) have the lowest Jacobi (highest V_∞) when x = 1 TR and the greatest x when $V_\infty = 0$. This suggests that they would make the good candidates for a capture orbit.

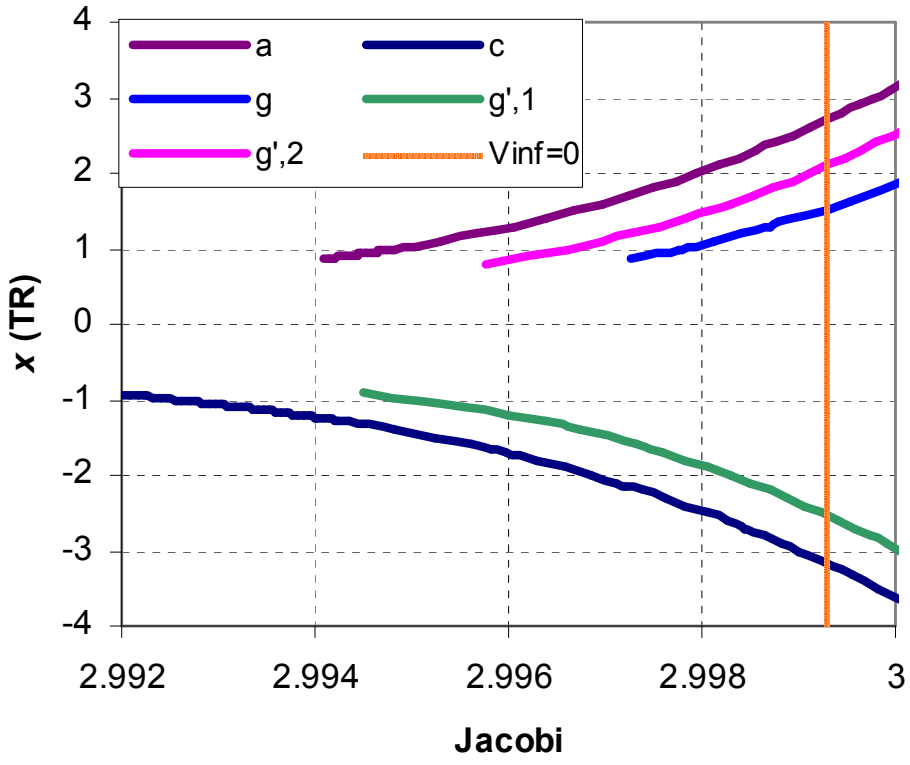

Figure 4.3. General map of periodic orbits in the (J, x) plane. The curves of various families impact the surface (TR = 1) as Jacobi decreases and V_∞ increases.

Table 4.1. Selected Hyperbolic Periodic Orbits at Titan (μ = 2.366e-4). Values given are for the point of closest approach. r_p is given in Titan radii (negative values correspond to passage on the Saturn side of Titan) and the other parameters are normalized using the conventions of the 3BP. $\boldsymbol{x_r}$ and $\dot{y}_r$ are in the rotating frame with respect to the barycenter. P is the orbit period. $\boldsymbol{x_{i,2}}$ and $\dot{y}_{i,2}$ are inertial with respect to Titan. V_∞ (3-body) is calculated using the approximation in Equation 2.83 whereas V_∞ (2-body) is calculated using Equation 4.1.

Family	r_p (TR)	J_3	x_r	$\dot{y}_r$	P	$x_{i,2}$	$\dot{y}_{i,2}$	$V_{\infty,3b}$	$V_{\infty,2b}$
a	1	2.9948	1.0019	0.4783	7.1670	0.0021	0.4804	0.0668	0.0791
a	1.1	2.9953	1.0021	0.4560	7.0441	0.0023	0.4583	0.0633	0.0769
a	1.5	2.9967	1.0029	0.3900	6.5909	0.0032	0.3931	0.0510	0.0698
a	2	2.9979	1.0040	0.3368	6.1039	0.0042	0.3410	0.0366	0.0634
a	3	2.9998	1.0061	0.2725	5.3545	0.0063	0.278	-	0.0537
a	5	3.0025	1.0103	0.2044	4.4497	0.0105	0.2149	-	0.0360
a	7	3.0049	1.0145	0.1641	3.9549	0.0148	0.1788	-	-
c	-1	2.9925	0.9977	-0.4807	7.3526	-0.0021	-0.4828	0.0821	0.0925
c	-1.1	2.9932	0.9974	-0.4582	7.2495	-0.0023	-0.4605	0.0779	0.0893
c	-1.5	2.9952	0.9966	-0.3918	6.8474	-0.0032	-0.3950	0.0637	0.0796
c	-2	2.9969	0.9955	-0.3384	6.3777	-0.0042	-0.3426	0.0493	0.0715
c	-3	2.9990	0.9934	-0.2739	5.5871	-0.0063	-0.2802	0.0169	0.0606
c	-5	3.0019	0.9892	-0.2058	4.5514	-0.0105	-0.2163	-	0.0435
c	-7	3.0044	0.9850	-0.1655	3.9606	-0.0148	-0.1802	-	0.0201
f	-30	2.9953	0.9365	0.1543	4.0658	-0.0632	0.0910	0.0634	0.0284
f	-40	2.9919	0.9154	0.1881	5.0170	-0.0843	0.1039	0.0900	0.0719
f	-50	2.9878	0.8944	0.2273	5.5451	-0.1054	0.1219	0.1072	0.1018
f	-70	2.9770	0.8522	0.3131	5.9891	-0.1475	0.1656	0.1492	0.1556
g	1	2.9978	1.0019	0.4752	9.1907	0.0021	0.4773	0.0387	0.0573
g	1.1	2.9981	1.0021	0.4528	9.0096	0.0023	0.4552	0.0342	0.0553
g	1.6	2.9995	1.0032	0.3695	8.1148	0.0035	0.3729	-	0.0462
g	2.6	3.0014	1.0053	0.2894	6.8253	0.0055	0.2949	-	0.0317
g'1	-1	2.9951	0.9977	-0.4780	11.0724	-0.0021	-0.4801	0.0649	0.0775
g'1	-1.1	2.9955	0.9974	-0.4571	10.8048	-0.0023	-0.4594	0.0611	0.0832
g'1	-1.6	2.9973	0.9964	-0.3770	9.6612	-0.0034	-0.3803	0.0443	0.0657
g'1	-2	2.9983	0.9955	-0.3363	8.9415	-0.0042	-0.3405	0.0317	0.0606
g'1	-2.7	2.9996	0.9941	-0.2876	7.9255	-0.0057	-0.2933	-	0.0537
g'2	1	2.9966	1.0019	0.4764	10.2643	0.0021	0.4785	0.0517	0.0668
g'2	1.1	2.9970	1.0021	0.4541	10.0176	0.0023	0.4564	0.0482	0.0649
g'2	1.5	2.9981	1.0029	0.3882	9.1730	0.0032	0.3914	0.0348	0.0589
g'2	2	2.9991	1.0040	0.3350	8.3332	0.0042	0.3393	0.0132	0.0532
g'2	3	3.0007	1.0061	0.2708	7.1071	0.0063	0.2771	-	0.0440

Inspection of the last two columns of Table 4.1 shows that the 2-body V_∞ at the point of closest approach differs from the 3-body value. This is due to the 3-body approximation assumption that the spacecraft be far from the second body. With the exception of the distant retrograde orbits, the 2-body values are greater than the 3-body values and those positive V_∞'s extend to greater distances from m_2. However,

this relationship does not hold true over the entire orbit. If the instantaneous $V_{\infty,2b}$ is calculated over the whole 3-body orbit, we can see that it varies widely. Figure 4.4 shows the V_∞ values over three *a*-type orbits with r_p = 1.1, 1.6, and 2 TR. For lower energy orbits, the $V_{\infty,2b}$ curve actually goes to zero for those times that the spacecraft is far from the secondary, indicating that the periodic orbit is hyperbolic near closest approach and gravitationally bound elsewhere. The fact that $V_{\infty,2b} > V_{\infty,3b}$ at t = 0 is true for all orbits (excluding *f*) where $V_{\infty,3b} > 0$, further bolstering the rationale to use hyperbolic periodic orbits as a capture mechanism.

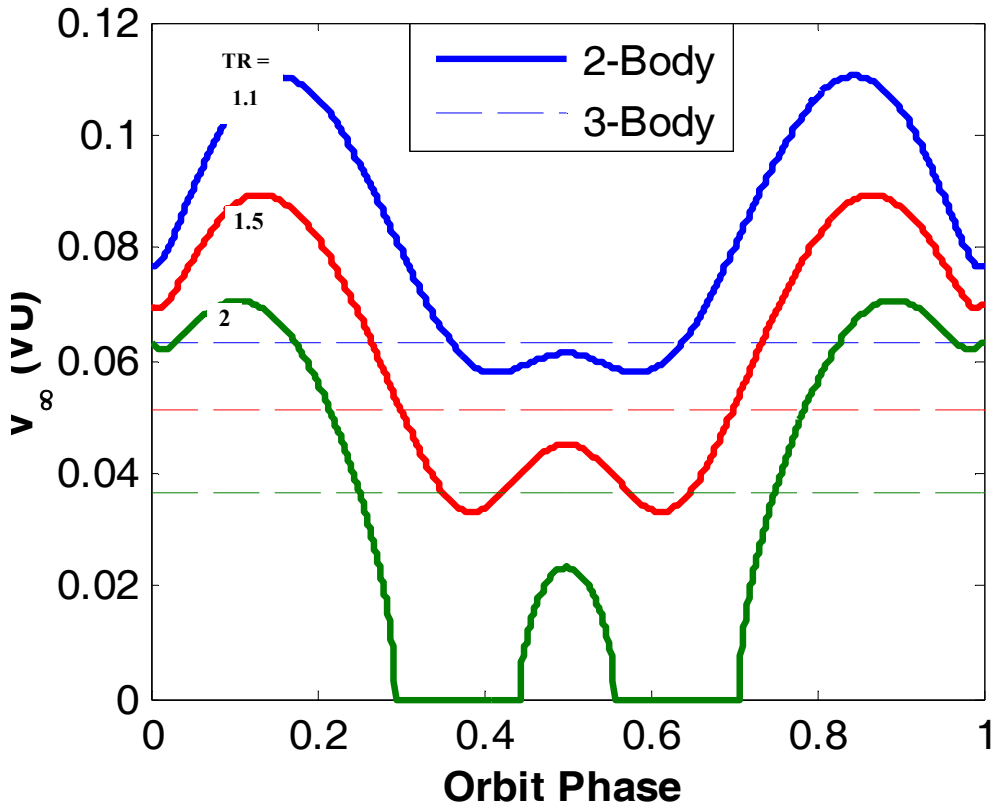

Figure 4.4. Instantaneous V_∞ values over one orbital period for family *a* orbits with r_p = 1.1 TR(blue), 1.5 TR(red), and 2 TR(green). Phase = 0 corresponds to the point of closest approach.

The relationship between Jacobi and V_∞ while in close proximity to the secondary is further examined in Figure 4.5. The solid blue line is the simple quadratic relationship approximated in the 3BP from Equation 2.83. The other curves represent the actual 2-body calculated relationship for families of periodic orbits. They approach the 3-body approximation as V_∞ gets large, but they vary at $V_\infty = 0$. The curves for families *a, c*, and *g'* (*g* is very similar to *g'* and was not included in the plot for clarity) terminate when TR = 1 (collision) at much higher Jacobi values than the 3-body estimate, which means that they have an even greater relative velocity at that point and require less ΔV to achieve from a hyperbolic passage.

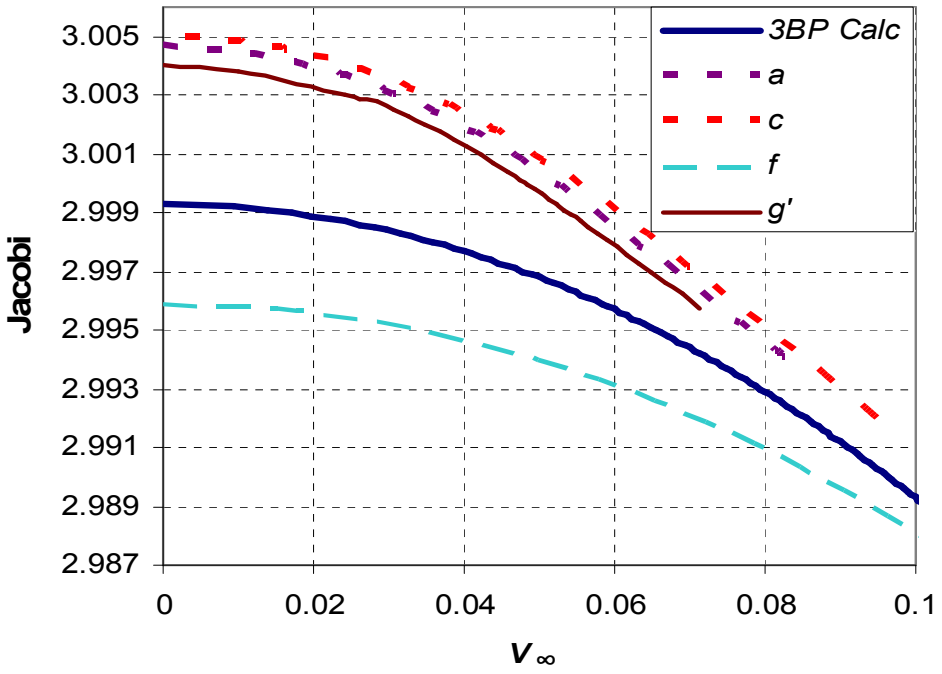

Figure 4.5. Jacobi vs. V_∞. The solid blue line is the simple quadratic relationship approximated in the 3BP from Equation 2.83. The other curves represent the actual 2-body calculated relationship for families of periodic orbits.

In the previous chapter we studied endgame tour sequences that consisted of ever decreasing resonant orbits until gravitational capture at the target moon could be achieved. Gravitational capture was defined as $V_\infty = 0$, which corresponds to a parabolic orbit centered on the moon. The relative velocity at periapsis (which would be the location of the insertion burn) is just $\sqrt{2}$ times the local circular velocity, V_c. Hyperbolic periodic orbits have a greater relative velocity than parabolic orbits at the same distance. The difference between the velocity for *a*-type and parabolic orbits (ΔV_p) versus periapsis distance is show by the dashed line in Figure 4.6. However, a parabolic orbit is not a true capture orbit as it does not return to the target body. In practice, long-period elliptical orbits are used for the initial insertion, and then later

adjustments bring the orbit down to the desired level. If we wish to compare the true usefulness of periodic capture orbits, we must calculate the required periapsis velocity of an elliptical orbit with a period equal to the period of a periodic orbit with the same periapsis. The difference in velocity in normalized units is given by

$$\Delta V_e = \left|\dot{y}_{i,2}\right| - \sqrt{\frac{2\mu}{\left|x_{i,2}\right|} - \mu\left(\frac{\mu P^2}{1-\mu}\right)^{-1/3}} \quad . \tag{4.2}$$

where $x_{i,2}$ and $\dot{y}_{i,2}$, and P are the characterizing parameters of the periodic orbit. This quantity is shown by the solid red line in Figure 4.6. For near-grazing orbits the maximum benefit of a Lyapunov capture orbit is 0.0077 velocity units, which for Titan corresponds to a savings of 43 m/s. This is significant when considering that it requires 190 m/s to capture to a highly elliptical orbit from a 2:1 resonance with Titan.

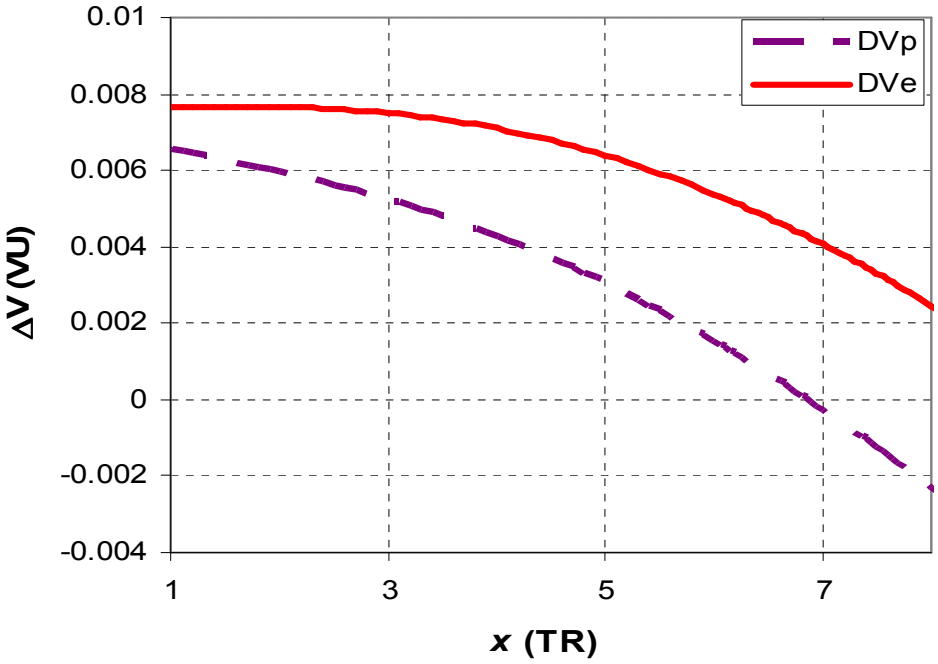

Figure 4.6. The difference in velocity at periapsis between a-type periodic orbits and a parabolic orbit (ΔV_p) or an elliptical orbit with an equivalent period (ΔV_e).

4.2.1 Hyperbolic Periodic Orbits as Capture Mechanisms

In the 2BP, the location of the insertion maneuver is inconsequential as long as the desired periapsis radius is achieved. Targeting periodic orbits in the 3BP, however, requires that the angle with respect to the line of syzygy be specified as well. For resonant orbits greater than one, the y-component of the V_∞ vector during a fly-by will be positive, regardless of whether the x crossing is positive or negative. This means that $\dot{y}$ of a target periodic orbit should be positive as well, eliminating families *c* and *g'1* as potential candidates.[33] Also, since the x-axis crossing must be perpendicular, the orientation of V_∞ (designated by α as depicted in Figure 2.5)

[33] Families *c* and *g'1* can still be targeted at their second x-axis crossing, but at a significant loss in efficiency.

should be such that half the bending of the trajectory during fly-by, δ, leads to the desired condition at periapsis. Specifically, δ must equal twice α, where δ is given by

$$\delta = 2\sin^{-1}\left(\frac{\mu_2}{\mu_2 + r_p V_\infty^2}\right), \tag{4.3}$$

where μ_2 may be replaced with μ if r_p and V_∞ are given in normalized values. The bending angle must equal 2α because of the fact that only half of the bending will be achieved before periapsis, at which point a retro-maneuver is performed to match the velocity with that of the targeted periodic orbit. The geometry of the desired fly-by and maneuver is depicted in Figure 4.7.

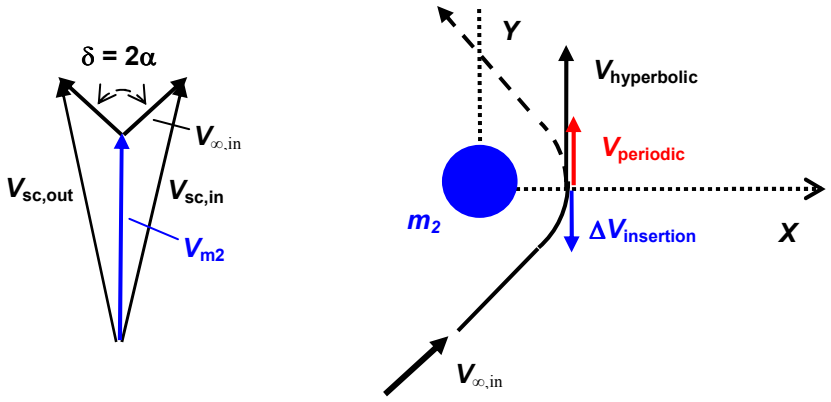

Figure 4.7. Hyperbolic passage and periodic orbit targeting. In order to have a perpendicular crossing of the x-axis and perform a $\Delta V_{insertion}$ to target a periodic orbit, the turn angle, δ, must be equal to 2α of the hyperbolic orbit.

Endgame sequences of resonant orbits can be plotted on a "V_∞ Resonance Plane", which is a map of lines of resonances and maximum turn angles as a function of V_∞ and α. Figure 4.8 shows the zig-zag pattern of the example sequence plotted on the V_∞ Resonance Plane. The goal of any endgame sequence is reduce V_∞ to zero, which corresponds to the bottom of this map. Since fly-bys cannot change V_∞, the

only way to move downwards is through the use of ΔV maneuvers. Fly-bys change α while V_∞ remains constant and are represented in Figure 4.8 by horizontal lines. V_∞ leveraging maneuvers modify both α and V_∞ and roughly follow the lines of resonance.

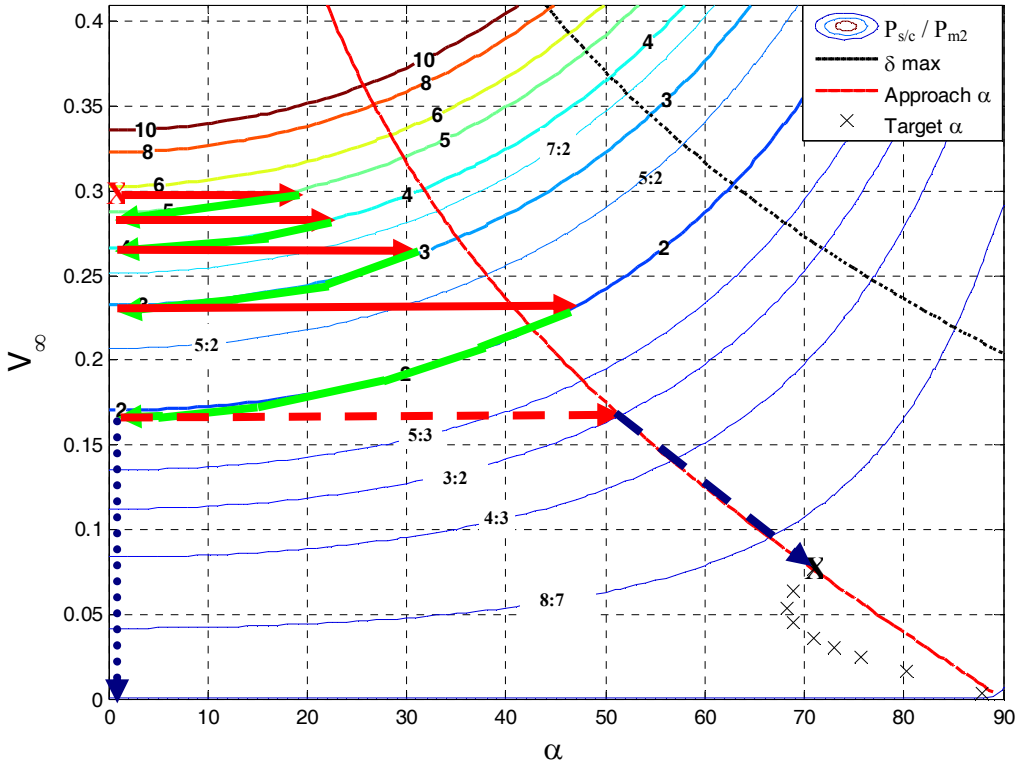

Figure 4.8. The V_∞ Resonance Plane. Colored contours represent lines of resonance for orbits of a given V_∞ and α. The dotted black line shows the maximum turn angle, δ, as a function of V_∞. The red contour shows the location of approach α's that lead to periodic orbit capture conditions. The black X's are the 2-body representations of a few periodic orbits from family *a*. One potential resonance tour is illustrated with fly-bys, leveraging maneuvers and powered fly-bys represented by red, green, and blue arrows, respectively. The dotted blue arrow shows a direct insertion maneuver to a parabolic orbit, whereas the dashed red and blue arrows show an alternative approach and capture to a hyperbolic periodic orbit.

An example sequence of leveraging maneuvers and fly-bys of 6:1, 5:1, 4:1, 3:1, and 2:1 is drawn on the V_∞ resonance plane. At its conclusion, a powered fly-by

maneuver is performed to reduce V_∞ to zero. This sequence requires 0.046 VU (258 m/s @ Titan) in ΔV, of which 0.033 (190 m/s) are needed for the final maneuver, and 88 TU (223 days) to perform. This result can be compared to a direct insertion maneuver from the 6:1 resonance (V_∞ = 0.3048) to V_∞ = 0, which requires 0.097 VU (540 m/s). The added flight time of the resonance tour buys over 50% in ΔV savings.

There are hundreds of possible resonance sequences that result in up to 60% ΔV savings for only a modest increase in total flight time (Woolley and Scheeres, 2010). The problem is that the final insertion maneuver in each sequence typically uses around 75% of the total sequence ΔV requirement. If a hyperbolic periodic orbit is targeted at the end of the sequence then about 0.007 VU (~40 m/s) can be saved. This is about 25% of the final insertion maneuver, or an additional 8% savings versus the direct insertion approach.

The sequence plotted on Figure 4.8 concludes at V_∞ = 0, shown by the vertical, blue dotted arrow. An alternate conclusion to a periodic orbit is shown by the red and blue dashed arrows. The red one represents a fly-by designed to set up the final insertion approach geometry by targeting the $\alpha = \frac{1}{2}\delta_{max}$ line depicted by the red contour. Halfway through the subsequent fly-by, an insertion maneuver matches the velocity to that of the periodic orbit and capture occurs. This is represented by the blue dashed arrow that terminates at the bold **X**, which still has a positive V_∞.

The δ_{max} and approach α lines are calculated for a specific radius of periapsis, in this case r_p = 1.1 TR. Capture can take place at greater distances, but this is usually at a loss in efficiency, as ΔV maneuvers are most efficient were velocity is the greatest. The other X's near the bottom right-hand corner of the plot represent the

target conditions for other periodic orbits with increasing periapses. They are each the termination point of a corresponding approach α line and represent the 2-body conditions that result in a 3-body "exit" from the V_∞ Resonance Plane.

4.3 Conclusion

Periodic orbits in the PR3BP that exist near the secondary and are hyperbolic in the 2BP are useful as capture mechanisms at planetary moons. We have shown that most families of simple periodic orbits have increasingly positive V_∞'s as their periapses approach the radius of the target moon. Lyapunov orbits (families *a* and *c*) have the highest V_∞ for a given periapsis distance, and family *a* is the most suitable for capture from resonance orbits greater than one due to its approach geometry conditions. Targeting a "hyperbolic periodic" orbit during the final phase of a leveraging maneuver sequence results in a lower required insertion ΔV, on the order of 20-25%.

This dissertation explores the limits and usefulness of hyperbolic periodic orbits and their application to the endgame problem. Orbits were generated using a single shooting method in the planar restricted problem and integrated into the final phase of leveraging sequences found in Section 3.7. We showed that using a hyperbolic periodic orbit to capture to the vicinity of a target moon following an optimized sequence of leveraging maneuvers and fly-bys yields significant fuel savings (60-70%) over direct trajectories.

We have only presented simple planar periodic orbits, yet an infinite number of more complex periodic and quasi-periodic orbits exist. It is unlikely that higher

order planar orbits will result in higher V_∞'s at the same distances as Lyapunov orbits, however, they may exhibit properties that are much more desirable from a mission design standpoint. Depending on a mission's requirements (ΔV, duration, science objectives, lighting angles, communications, etc.), any of the 3-body periodic orbits may exhibit both pros and cons for mission optimization. There also exist 3-dimensional periodic orbits that can be used as efficient capture and transfer mechanisms for orbiters wishing to achieve low, highly-inclined science orbits about a planetary moon.

5 Discussion

5.1 Overview of Findings

V_∞ leveraging is a useful tool in the design of planetary moon endgame strategies. If applied properly it is possible to significantly reduce the total ΔV required to send an orbiter to a planetary moon such as Titan. In this dissertation we present theoretical calculations that show that the total ΔV required can be up to 10 times or more the change in ΔV_∞. While the theoretical minima require infinite durations, they do serve to illustrate a lower bound on the fuel required to place a spacecraft into a captured orbit. As the V_∞ decreases, leveraging maneuvers become less and less efficient. Below a certain point, it was shown that powered fly-bys become a more efficient means of V_∞ reduction.

In addition, we have developed tools to construct, map, and analyze sequences of leveraging maneuvers and to compare them to the theoretical minimum. The reduction in fuel requirements comes at the expense of added flight time. Tens of thousands of sequences were generated using a Monte-Carlo type simulation and the total ΔV and *TOF* pairs were accumulated. By plotting these pairs we were able to generate a Pareto front of most efficient sequences for a given flight time.

Reducing a 6:1 orbit to $V_\infty = 0$ using a direct burn during fly-by would require 0.097 velocity units, whereas an infinite series of fly-bys and leveraging maneuvers

(theoretical minimum) would reduce the total ΔV required to 0.028, a savings of over 70%. Since infinite missions are not possible, it is helpful to the mission designer to know that it is possible to reduce the total ΔV by 50% with a TOF of only 5-10 time units. Increasing the mission duration further does not result in significant reductions.

Periodic orbits in the PR3BP that exist near the secondary and are hyperbolic in the 2BP are useful as capture mechanisms at planetary moons. We have shown that most families of simple periodic orbits have increasingly positive V_∞'s as their periapses approach the radius of the target moon. Lyapunov orbits (families *a* and *c*) have the highest V_∞ for a given periapsis distance, and family *a* is the most suitable for capture from resonance orbits greater than one due to its approach geometry conditions. Targeting a "hyperbolic periodic" orbit during the final phase of a leveraging maneuver sequence results in a lower required insertion ΔV, on the order of 20-25%.

5.1.1 Contributions to the Field

The V_∞ Sphere and V_∞ Plane are useful design tools in that they allow the designer to quickly see what types of orbits are possible given a set of input parameters. Post fly-by orbits can be targeted by noting the change of α required on the V_∞ Plane. Sequences of leveraging maneuvers and fly-bys can be plotted as points on the map.

5.1.2 Areas of Future Research

The maneuver sequences detailed in this dissertation are restricted to orbits confined to the plane of the gravity-assist body and are very theoretical in nature. In practice planetary tours make use of inclined orbits, fly by other moons, and must take into account many other factors. Because of this, the more "optimal" tour sequences generated here are not necessarily what would be used in true mission design. However, the tools and results are instructive for preliminary analyses and for understanding the trends that lead to optimal tour design.

We have only presented simple planar periodic orbits, yet an infinite number of more complex periodic and quasi-periodic orbits exist. It is unlikely that higher order planar orbits will result in higher V_∞'s at the same distances as Lyapunov orbits, however, they may exhibit properties that are much more desirable from a mission design standpoint. Depending on a mission's requirements (ΔV, duration, science objectives, lighting angles, communications, etc.), any of the 3-body periodic orbits may exhibit both pros and cons for mission optimization. There also exist 3-dimensional periodic orbits that can be used as efficient capture and transfer mechanisms for orbiters wishing to achieve low, highly-inclined science orbits about a planetary moon.

6 Bibliography

Anderson, R.L., *Low Thrust Trajectory Design for Resonant Flybys and Captures Using Invariant Manifolds*. PhD, University of Colorado, 2005.

Barrow-Green, J. *Poincaré and the Three Body Problem*. American Mathematical Society - London Mathematical Society, Providence, Rhode Island, 1997.

Bate, R., D. Mueller, and J. White, *Fundamentals of Astrodynamics*, New Dover Publications, New York, 1971, pp. 198-233.

Battin, R.H., An Introduction to the Mathematics and Methods of Astrodynamics, AIAA Education Series, AIAA, New York, 1987.

Boutonnet, A., P. d. Pascale, and E. Canalias, "Desing of the Laplace Mission," Paper IAC-08-C1.6, 59th IAC, Glasgow, Scottland, 2008.

Breakwell, J.V. and J.V. Brown, "The 'Halo' Family of 3-Dimensional Periodic Orbits in the Earth-Moon Restricted 3-Body Problem," *Celestial Mechanics*, vol. 20, p. 389, 1979.

Brinckerhoff, A.T. and R.P. Russell, "Pathfinding and V_∞ Leveraging for Planetary Moon Tour Missions," *AIAA/AAS Space Flight Mechanics Meeting*, AAS Paper 09-222, Savannah, Georgia, February 2009.

Campagnola, S. and R.P. Russell, "Endgame Problem Part 1: V_∞-Leveraging Technique and the Leveraging Graph," *Journal of Guidance, Control, and Dynamics*, Vol. 33, No. 2, pp. 463-475, March-April 2010a.

Campagnola, S. and R.P. Russell, "Endgame Problem Part 2: Multi-body Technique and the Tisserand-Poincaré Graph," *Journal of Guidance, Control, and Dynamics*, Vol. 33, No. 2, pp. 476-486, March-April 2010b.

Campagnola, S., N.J. Strange, and R.P. Russell, "A Fast Tour Design Method Using Non-Tangent V-Infinity Leveraging Transfers," *AAS/AIAA Spaceflight Mechanics Meeting,* AAS Paper 10-164, San Diego, CA, February 2010c.

Casalino, L., G. Colasurdo, and D. Pastrone, "Optimization of Delta-V Earth-Gravity-Assist Trajectories," *Journal of Guidance, Control, and Dynamics*, Vol. 21, No. 6, November 1998.

Chobotov, V., "Orbital Mechanics", AIAA Education Series, 1991.

Clark, K. C., R. Greeley, R. Pappalardo, and C. Jones, "2007 Europa Explorer Mission Study: Final Report," Task Order #NMO710851, JPL D-41283, November 1, 2007.

Colasurdo, G., L. Casalino, and E. Fantino, "Minimum-fuel Escape from Two-Body Sun-Earth System." *Journal of Guidance, Control, and Dynamics*, Vol. 22, No. 5, September 1999.

Curtis, H. D., *Orbital Mechanics for Engineering Students*, Elsevier, 2005.

Danby, J.M.A., *Fundamentals of Celestial Mechanics*, Willmann-Bell, Inc., Richmond, VA, 1992.

Darwin, G. H., "Periodic Orbits," *Acta Mathematica*, Vol. 21, pp. 99–242, 1897.

Darwin, G. H., "Periodic Orbits," *Scientific Papers*, Vol. 4, Cambridge University Press, Cambridge, Mass., 1911.

Demeyer, J. and P. Gurfil, "Transfer to Small Distant Retrograde Orbits," in *New Trends in Astrodynamics and Applications III*, E. Belbruno, Ed., vol. 886, pp. 20-31, Princeton, New Jersey 2007.

Edwards, W. et al., "Titan Explorer: The Next Step in the Exploration of a Mysterious World," *Final Report for NASA Vision Mission Study*, NRA-03-OSS-01, Presented at the Outer Planets Assessment Group, October 6-7, 2005.

Euler, L., *Theoria Motuum Planetarum et Cometarum*, Berlin, 1744.

Farquhar, R. W. "The Flight of ISEE-3/ICE: Origins, Mission History, and a Legacy." AIAA Paper 98-4464, *AIAA/AAS Astrodynamics Specialist Conference and Exhibit*, Boston, Massachusetts, August 1998.

Gomez, G., M. Lara, and R. Russell, "A Dynamical Systems Approach to the Design of the Science Orbit Around Europa," *ISTS*, 2006.

Heaton, A.F., N. J. Strange, J. M. Longuski, and E. P. Bonfiglio, "Automated Design of the Europa Orbiter Tour," AIAA Paper 2000-4034, 2000.

Hénon, M., "Exploration Numérique du Probléme des Trois Corps, I. Masses égales, Orbites Périodiques," *Ann. d'Astrophys.* Vol. 28, pp. 499-511, 1965a.

Hénon, M., “Exploration Numérique du Probléme des Trois Corps, II. Masses égales, stabilité des orbites périodiques,” *Ann. d'Astrophys.* Vol. 28, pp. 992-1000, 1965b.

Hénon, M., “Exploration Numérique du Probléme des Trois Corps, III. Masses Egales, Orbites Non Périodiques,” *Bull. Astron*., Volume 1(1), pp. 57–80, 1966a.

Hénon, M., “Exploration Numérique du Probléme des Trois Corps, IV. Masses Egales, Orbites Non Périodiques,” *Bull. Astron*., Volume 1(2), pp. 49–66, 1966b.

Hénon, M., “Generating Families in the Restricted Three-Body Problem,” *Lecture Notes in Physics*, Vol. 52, Springer, Berlin, 1997.

Hénon, M., “New Families of Periodic Orbits in Hill’s Problem of Three Bodies,” *Celestial Mechanics and Dynamical Astronomy*, Vol. 85, pp. 223-246, 2003.

Hénon, M., “Numerical Exploration of the Restricted Problem. VI. Hill's Case: Non-Periodic Orbits.” *Astronomy and Astrophysics.* Vol. 1, pp. 24-36, 1970.

Hénon, M., “Numerical Exploration of the Restricted Problem.V. Hill’s Case: Periodic Orbits and Their Stability.” *Astronomy and Astrophysics*, Vol. 1, pp. 223–238, 1969.

Hill, G.W., “Researches in the Lunar Theory,” *American Journal of Mathematics*, Vol. 1, No. 1, 1878, pp. 5–26.

Hollenbeck, G.R., “New Flight Techniques for Outer Planet Missions,” *AAS/AIAA Astrodynamics Specialist Conference*, AAS Paper 75-087. July 1975.

Howell, K.C., “Three-Dimensional, Periodic, ‘Halo’ Orbits,” *Celestial Mechanics*, vol. 32, pp. 53-71, 1984.

Johannesen, J.L. and L.A. D'Amario, “Europa Orbiter Mission Trajectory Design,” *AAS/AIAA Astrodynamics Specialist Conference*, AAS Paper 99-360, Girdwood, Alaska, August 1999.

Lagrange, J., “Essai sur le probléme des trois corps,” *Gallica,* Volume 6, pp. 272–292, 1867-1892.

Lam, T. and G. J. Whiffen, "Exploration of Distant Retrograde Orbits around Europa," *AAS/AIAA Space Flight Mechanics Meeting,* AAS Paper 05-110, January 2005.

Lyapunov, A. M., "The General Problem of the Stability of Motion," *Comm. Soc. Math.* Kharkow, 1892.

Nakamiya, M., D.J. Scheeres, H. Yamakawa, and M. Yoshikawa, "Analysis of Capture Trajectories into Periodic Orbits about Libration Points," *AAS/AIAA Spaceflight Mechanics Meeting*, AAS Paper 07-228, Sedona, Arizona, 2007.

Newton, I., *Philosophiae Naturalis Principia Mathematica*, Londoni, 1687.

Poincaré, H., "Sur le probléme des trois corps et les équations de la dynamique," *Acta Math.*, Volume 13,, pp. 1–27, 1890.

Poincaré, H., *New Methods of Celestial Mechanics, 1. Periodic and Asymptotic Solutions*, edited by F. Goroff, D. L., American Institute of Physics, USA, 1993.

Prussing, J.E. and B.A. Conway, *Orbital Mechanics*, Oxford University Press, 1993.

Ross, S.D. and D.J. Scheeres, "Multiple Gravity Assists, Capture, and Escape in the Restricted Three-Body Problem," *SIAM Journal on Applied Dynamical Systems*, Vol. 6, No. 3, pp. 576-596, 2007a.

Ross, S.D. and P. Grover, "Fuel-optimal Trajectories in a Planet-Moon Environment using Multiple Gravity Assists," *International Symposium on Space Flight Dynamics*, 2007b.

Russell, R.P. and T. Lam, "Designing Capture Trajectories to Unstable Periodic Orbits Around Europa," *AAS/AIAA Space Flight Mechanics Meeting*, AAS Paper 06-189, Tampa, Florida, 2006.

Russell, R.P., "Global Search for Planar and Three-Dimensional Periodic Orbits Near Europa," *AAS/AIAA Astrodynamics Specialist Conference*, AAS Paper 05-290, Lake Tahoe, California, August 2005.

Schaub, H.P. and J.L. Junkins, Analytical Mechanics of Space Sytems, AIAA Education Series, AIAA, Virginia, 2003.

Scheeres, D.J. and M.D. Guman, "Stability Analysis of the Europa Orbiter," *Spaceflight Mechanics 2000, Part II, Advances in the Astronautical Sciences Series*, vol. 105, pp. 855-868. Univelt, 2000.

Scheeres, D.J., M.D. Guman, and B. F. Villac, "Stability Analysis of Planetary Satellite Orbiters: Application to the Europa Orbiter," *Journal of Guidance, Control, and Dynamics,* vol. 24, no. 4, pp. 778–787, 2001.

Sims, J.A. and J.M. Longuski, “Analysis of V-infinity Leveraging for Interplanetary Missions,” *AIAA/AAS Astrodynamics Conference*, AAS Paper 94-3769, Scottsdale, AZ, 1994.

Sims, J.A., J.M. Longuski, and A.J. Staugler, “V_∞ Leveraging for Interplanetary Missions: Multiple-Revolution Orbit Techniques,” *Journal of Guidance Control and Dynamics*, Vol. 20, No. 3, pp. 409-415, 1997.

Strange, N. J. and J. M. Longuski, "Graphical Method for Gravity-Assist Trajectory Design," *Journal of Spacecraft and Rockets*, vol. 39, no. 1, pp. 9-16, 2002.

Strange, N.J., R. Russell, and B. Buffington, “Mapping the V_∞ Globe,” *AIAA/AAS Space Flight Mechanics Meeting*, AAS Paper 07-277, 2007.

Strange, N.J., S. Campagnola, and R. Russell, "Leveraging Flybys of Low Mass Moons to Enable an Enceladus Orbiter," *AAS/AIAA Astrodynamics Specialist Conference*, AAS Paper 09-435, August 2009a.

Strange, N.J., T.R. Spilker, D.F. Landau, T. Lam, D.T. Lyons, and J.J. Guzman, “Mission Design for the Titan Saturn System Mission Concept," *AAS/AIAA Astrodynamics Conference*, AAS Paper 09-356, Pittsburgh, PA, Aug. 2009b.

Strömgren, E., “Connaissance actuelle des orbites dans le probléme des trios corps,” *Bulletin Astronomica*. Vol. 9, No. 87, 1935.

Sundman, K., “Nouvelle Recherches sur le Probléme des Trois Corps,” *Acta Societatis Scientiarum Fennicae*, Volume 35, 1909.

Sweetser, T.H., “Jacobi's Integral and Delta-V-Earth-Gravity-Assist Trajectories,” *AAS/AIAA Astrodynamics Specialist Conference*, AAS Paper 93-635, Victoria, BC, Canada, August 1993.

Sweetser, T.H., R. Maddock, J. Johannesen, J. Bell, P. A. Penzo, A. Wolf, S. N. Williams, S. Matousek, and S. Weinstein, "Trajectory Design for a Europa Orbiter Mission: A Plethora of Astrodynamic Challenges," *Advances in the Astronautical Sciences*, vol. 95, pp. 901-920, 1997.

Szebehely, V., *Theory of Orbits.* The Restricted Problem of Three Bodies, Academic Press, New York, 1967.

Tisserand, F.F, *Traite’ de Mechanique Celeste*, Vol. 4. Gauthier-Villars et fils, 1896.

Uphoff, C., P. H. Roberts, and L. D. Friedman, “Orbit Design Concepts for Jupiter Orbiter Missions,” Journal of Spacecraft and Rockets, Vol. 13, No. 6, 1976, pp. 348-355.

Vallado, D.A. *Fundamentals of Astrodynamics and Applications*, Space Technology Library, Microcosm Press, El Segundo, California, 2001.

Villac, B. F. and D. J. Scheeres, "Escaping trajectories in the Hill Three Body Problem and Applications," *Journal of Guidance, Control, and Dynamics*, vol. 26, no. 2, pp. 224-232, 2003.

Villac, B. F., "Dynamics in the Hill Problem with Applications to Spacecraft Maneuvers," PhD, University of Michigan, 2003.

Wertz, J., *Mission Geometry; Orbit and Constellation Design and Management*, Space Technology Library, Microcosm Press, El Segundo, California, 2001.

Wiesel, W. E.. *Modern Astrodynamics*. Aphelion Press, Beavercreek, Ohio, 2004.

Woolley, R.C. and D.J. Scheeres, "Hyperbolic Periodic Orbits in the Three-Body Problem and Their Application to Orbital Capture," AAS George H. Born Symposium, Boulder, CO, May 13-14, 2010.

Woolley, R.C. and D.J. Scheeres, "Optimal Pathways for Sequences of V-infinity Leveraging Maneuevers," *AAS/AIAA Spaceflight Mechanics Meeting,* AAS Paper 10-219, San Diego, CA, February 2010.

Woolley, R.C. and D.J. Scheeres, "Shrinking the V-infinity Sphere: Endgame Strategies for Planetary Moon Orbiters," *AAS/AIAA Astrodynamics Specialist Conference,* AAS Paper 09-377, Pittsburgh, Pennsylvania, August 2009.

7 Appendix A: Nomenclature

δ	Turn angle of the V_∞ vector during a fly-by
ω	Angular velocity of secondary body about the primary
τ	One time unit, defined by $1/\omega$
γ	Flight path angle between V_{ga} and V_{sc}
Γ	Hénon's notation for Jacobi constant in Hill's Problem
δ_{max}	The maximum turn angle of a fly-by when r_{min} is used
E	Energy of the spacecraft
G	Universal gravitation constant
J_{3b}, J_H	Jacobi constant expressed in the 3BP or Hill's problem, respectively
l	Length unit in Hill's problem
L1, L2	Referring to the 1st and 2nd collinear Lagrangian or Libration points
LU,TU,VU	Abbrev. for normalized Length Unit, Time Unit, and Velocity Unit
m_1, m_2, m_3	Referring to the primary, secondary, or spacecraft, respectively
P, P_{sc}, P_{ga}	Period of the spacecraft/gravity-assist body
R	Distance between the primary, m_1, and secondary, m_2.
r, r_1, r_2	Distance from the barycenter, primary, or secondary, respectively
r_{ga}, a_{ga}	Radius and semimajor axis of the gravity-assist body, which are equivalent

r_{min}	Minimum allowable fly-by radius of the gravity-assist body
r_p	Radius of closest approach to the gravity-assist body
S_i, S_r	Inertial or rotational state vector, respectively
T, T_d	Non-dimensional and dimensional Tisserand's Parameter, respectively
TR	Periapsis distance equal to one Titan radius
V_∞	Hyperbolic excess velocity of the spacecraft with respect to m_2
V_c	The local circular velocity at r_p around m_2
V_{ga}	Velocity of the gravity-assist body (circular)
V_p	S/C Velocity at periapsis during a fly-by
V_{sc}	Spacecraft velocity with respect to the central body
α	The angle between V_∞ and V_{ga}
ΔV	The change in velocity during a maneuver
μ	Reduced mass of the system - $m_2/(m_1+m_2)$
μ_1, μ_2	Gravitational parameter (GM) of the primary (1) and secondary (2)

8 Appendix B: Coordinate Transformations

The state of a space craft in the rotating frame is given by

$$S_r = \begin{bmatrix} X \\ Y \\ \dot{X} \\ \dot{Y} \end{bmatrix} = T_d^n s_r = T_d^n \begin{bmatrix} x \\ y \\ \dot{x} \\ \dot{y} \end{bmatrix} \tag{8.1}$$

where s_r is the state in nondimensional units and T_d^n is the transformational matrix

$$T_d^n = \begin{bmatrix} R & 0 & 0 & 0 \\ 0 & R & 0 & 0 \\ 0 & 0 & \omega R & 0 \\ 0 & 0 & 0 & \omega R \end{bmatrix} \tag{8.2}$$

To transform the state from the rotational (or synodic) frame to the inertial (or sidereal) frame we must take into account the rotational offset, θ, and the angular rate, $\omega = \dot{\theta}$. Here we will assume the offset is zero (see Anderson (2005) for non-zero θ transformations). Since the Z axes are aligned in both frames we can write

$$S_i = \begin{bmatrix} X_i \\ Y_i \\ \dot{X}_i \\ \dot{Y}_i \end{bmatrix} = \begin{bmatrix} X \\ Y \\ \dot{X} - \omega Y \\ \dot{Y} + \omega X \end{bmatrix} \quad \text{and} \quad s_i = \begin{bmatrix} x_i \\ y_i \\ \dot{x}_i \\ \dot{y}_i \end{bmatrix} = \begin{bmatrix} x \\ y \\ \dot{x} - y \\ \dot{y} + x \end{bmatrix} \tag{8.3}$$

where the subscript 'i' denotes the inertial frame. (A subscript 'r' has been omitted from the rotational quantities for clarity and redundancy). Notice that $\omega = 1$ in the nondimensional frame. The relations in (2.72) can be reversed:

$$S_r = \begin{bmatrix} X_i \\ Y_i \\ \dot{X}_i + \omega Y_i \\ \dot{Y}_i - \omega X_i \end{bmatrix} \quad \text{and} \quad s_r = \begin{bmatrix} x_i \\ y_i \\ \dot{x}_i + y_i \\ \dot{y}_i - x_i \end{bmatrix} \tag{8.4}$$

Recall that the rotating frame is centered at the barycenter of m_1 and m_2. However, most inertial frames are centered on either of the bodies. As such we must shift the state vectors to the new center.

$$S_{i,1} = \begin{bmatrix} X + R_1 \\ Y \\ \dot{X} - \omega Y \\ \dot{Y} + \omega(X + R_1) \end{bmatrix}, \quad S_{i,2} = \begin{bmatrix} X - R_2 \\ Y \\ \dot{X} - \omega Y \\ \dot{Y} + \omega(X - R_2) \end{bmatrix}$$

and

$$s_{i,1} = \begin{bmatrix} x + \mu \\ y \\ \dot{x} - y \\ \dot{y} + x + \mu \end{bmatrix}, \quad s_{i,2} = \begin{bmatrix} x - (1 - \mu) \\ y \\ \dot{x} - y \\ \dot{y} + x - (1 - \mu) \end{bmatrix} \tag{8.5}$$

Where states with the added subscript ‘1’ refer to states centered at the primary and likewise, ‘2’, for the secondary.

9 Appendix C: Notes on Lambert's Problem

Lambert's problem is concerned with the determination of an orbit that passes between two positions within a specified time-of-flight. This classic astrodynamic problem is also known as the orbital two-point boundary value problem (TPBVP) or the flyby and rendezvous problems.

9.1 Lambert's Theorem

The theorem states that the time to traverse a trajectory depends only upon the length of the semimajor axis a of the transfer trajectory, the sum $r_i + r_f$ of the distances of the initial and final positions relative to a central body, and the length c of the chord joining these two positions. This relationship can be stated as follows:

$$tof = tof(r_i + r_f, c, a) \tag{9.1}$$

Using a geometrical approach starting from Kepler's second law (orbits sweep out equal areas in equal times), we can derive the following form of Kepler's equation

$$t - t_0 = \sqrt{\frac{a^3}{\mu}}(E - e\sin E) \tag{9.2}$$

from which we can write

$$\Delta t = \sqrt{\frac{a^3}{\mu}}[E - E_0 - e(\sin E - \sin E_0)] \tag{9.3}$$

where E is the eccentric anomaly associated with radius r, E_0 is the eccentric anomaly at r_0, and $t = 0$ when $r = r_0$. At this point we introduce the following trigonometric sum and difference identities:

$$\begin{aligned}
\sin\alpha - \sin\beta &= 2\sin\frac{\alpha-\beta}{2}\cos\frac{\alpha+\beta}{2} \\
\cos\alpha - \cos\beta &= -2\sin\frac{\alpha-\beta}{2}\sin\frac{\alpha+\beta}{2} \\
\cos\alpha + \cos\beta &= 2\cos\frac{\alpha-\beta}{2}\cos\frac{\alpha+\beta}{2}
\end{aligned} \tag{9.4}$$

If we let $E = \alpha$ and $E_0 = \beta$ and substitute the first trig identity into Equation 9.3, we have the following equation:

$$\Delta t = \sqrt{\frac{a^3}{\mu}}\left[E - E_0 - 2\sin\frac{E-E_0}{2}e\cos\frac{E+E_0}{2}\right] \tag{9.5}$$

If we manipulate the elliptic relationships given by

$$\begin{aligned}
r &= a(1 - e\cos E) \\
x &= a(\cos E - e) \\
y &= a\sin E\sqrt{1-e^2}
\end{aligned} \tag{9.6}$$

we obtain:

$$\begin{aligned}
\cos E &= \left(1 - \frac{r+r_0}{2a}\right) - \frac{c}{2a} \\
\sin E_0 &= \left(1 - \frac{r+r_0}{2a}\right) + \frac{c}{2a}
\end{aligned} \tag{9.7}$$

Next, we make use of the following three relationships:

$$\cos\frac{E-E_0}{2}\cos\frac{E+E_0}{2}=1-\frac{r+r_0}{2}$$
$$\sin\frac{E-E_0}{2}\sin\frac{E+E_0}{2}=\sin\frac{E-E_0}{2}\sqrt{1-\left(e\cos\frac{E+E_0}{2}\right)^2} \tag{9.8}$$
$$\left(\sin\frac{E-E_0}{2}\sin\frac{E+E_0}{2}\right)^2=\left(\frac{x-x_0}{2a}\right)^2+\left(\frac{y-y_0}{2a}\right)^2=\left(\frac{c}{2a}\right)^2$$

along with the trigonometric half angle formulas and several additional substitutions to derive the time-of-flight form of Lambert's theorem

$$\Delta t=\sqrt{\frac{a^3}{\mu}}\left[E-E_0-e(\sin E-\sin E_0)\right]. \tag{9.9}$$

If we wish to take into account multiple revolutions the time is given by

$$\Delta t=\sqrt{\frac{a^3}{\mu}}\left[2k\pi+E-E_0-e(\sin E-\sin E_0)\right] \tag{9.10}$$

where k is the number of complete revolutions and E is given in radians. The process of solving Lambert's theorem for any two position vectors and transfer time is done using iterations on a universal variable formulation (Vallado, 1997; Prussing and Conway, 1993).

9.2 Multi-Revolution Solutions to Lambert's Problem

The universal variables solution to Lambert's problem, as discussed in Section 2.1.3, only admits hyperbolic and elliptical solutions of less than one full revolution. This is due to the omission of the $2k\pi$ term of Equation 2.8. The parameter z increases monotonically with total TOF until $z = (2\pi)^2$ and TOF $\rightarrow \infty$. This is shown in Figure 9.1. When z is negative the solution is hyperbolic and elliptical when it is greater than zero. However, for long transfer times, it is possible to complete

multiple revolutions of the transfer ellipse before rendezvous occurs. This happens when $z > (2\pi)^2$. Above this value, TOF decreases as z increases up to some minimum TOF, and then begins increasing to infinity again at $z = (4\pi)^2$. These solutions correspond to a type III trajectory of up to 1.5 revolutions.[34]

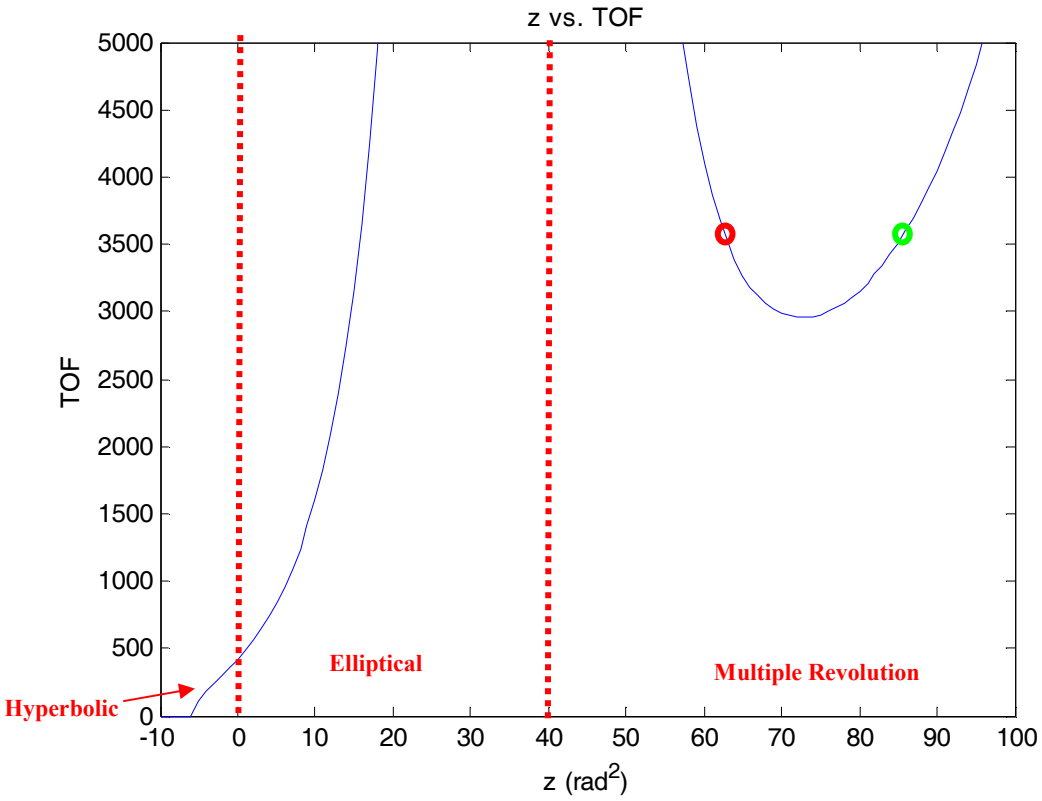

Figure 9.1. Universal variables solution regions for Lambert's problem.

Except for the minimum TOF (around $z = 73$ in Figure 9.1), type III trajectories have both an inbound and outbound solution for a given TOF. This is shown by the red and green ellipses in Figure 9.2. Both have the same transfer time and are followed for ~1.5 revolutions before the transfer is complete. Specifying that

[34] Type I and II trajectories have transfers of less than 180 degrees and greater than 180 degrees, respectively.

a multi-revolution solution be used requires that a proper initial guess and bounds be given for z before the iteration scheme takes place. It is also important to use a method that considers solutions that are both increasing and decreasing. For this reason it is not recommended to use a bisection technique that only finds solutions with positive slope. However, both secant and Newton iteration schemes work quite well.

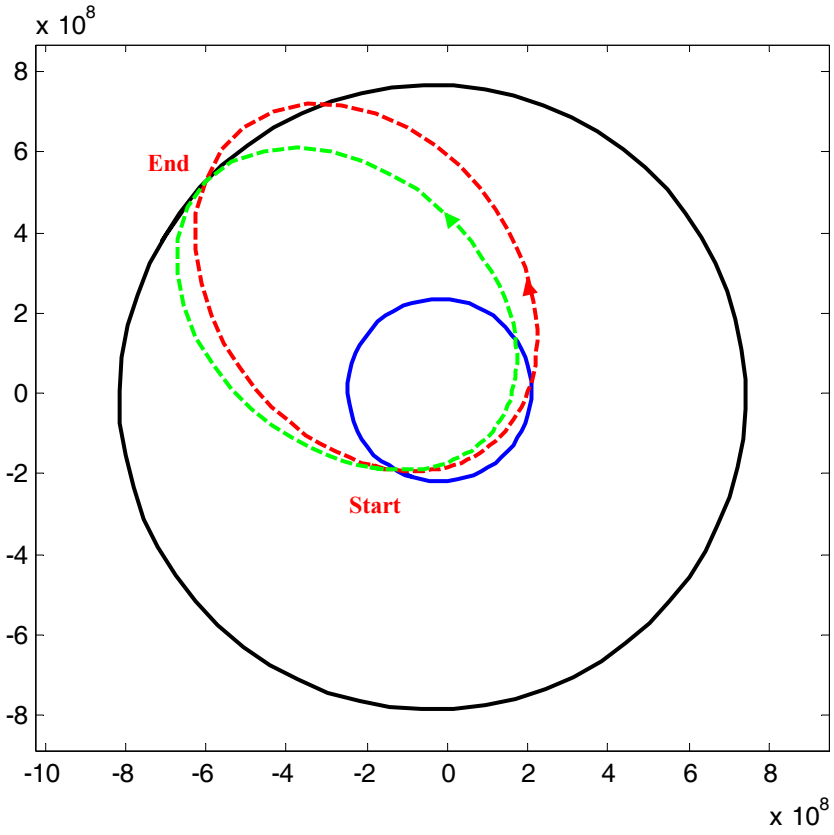

Figure 9.2. Type III inbound (red) and outbound (green) transfer trajectories.

For type III trajectories, the bounds on z must be set to $(2\pi)^2$ and $(4\pi)^2$. Above this region the z vs. TOF plot makes another dip between $(4\pi)^2$ and $(8\pi)^2$, corresponding to type IV trajectories, which have greater than 540° transfers. This

trend continues with asymptotes at $(16\pi)^2$, $(32\pi)^2$, and so on, marking the boundaries for higher revolution transfers.

10 Appendix D: Tables of V_∞ Leveraging Sequences

These tables contain some of the most efficient sequences found during the Monte Carlo simulations. In each table the total time (in TU[35]), total ΔV (in VU[36]), and resonance sequence are listed. The resonances are listed in decimal form. For example, "2" is 2:1, "3.75" is 15:4, etc. The sequences begin at $V_\infty = 0$ and progress outward until a 6:1 resonance with $\alpha = 0$ is achieved. The zeros after the "6" are merely place holders in the output.

The sequences where a zero is listed before 6:1 is reached indicates that a phasing orbit was required. The resonance immediately preceding that zero is a phasing resonance where no leveraging maneuver is performed. Sequences with values less than one indicate that a non-tangential maneuver was used. This is where α does not return to zero after a flyby, and a leveraging maneuver is performed on the subsequent resonance. The value that is less than one is the magnitude of α in degrees, divided by 100, for the resonance immediately following.

[35] The time units here are the period of the gravity-assist body (P), not $P/2\pi$ as used in the 3BP.

[36] One velocity unit is equal to the circular velocity of the gravity-assist body.

Table 10.1. Top Sequences with $V_c = 0.3$ and no crossing of the δmax line (NX). (See preceding paragraphs for column descriptions).

T	ΔV	Sequence									
75	0.0442	1.67	1.75	2	3	3.75	4	5	5.5	5.75	6
21	0.0445	1.75	2	3	4	5	6	0	0	0	0
45	0.0446	1.75	2	3	4	4.8	5	6	0	0	0
22	0.0446	1.67	1.75	2	3	5	6	0	0	0	0
56	0.0447	1.75	2	3	4	4.8	5	5.5	6	0	0
16	0.0447	1.75	2	3	4	6	0	0	0	0	0
18	0.0448	1.8	2	3	4	6	0	0	0	0	0
37	0.0449	1.8	2	3	3.8	4	6	0	0	0	0
46	0.0449	1.75	1.8	2	2.63	3	4	6	0	0	0
64	0.0449	1.75	2	2.71	3	4	4.8	5	6	0	0
43	0.0450	1.75	2	3	4.25	4.5	5	6	0	0	0
31	0.0451	1.75	2	3	4.67	5	6	0	0	0	0
54	0.0451	1.75	2	3	4.67	5	5.75	6	0	0	0
17	0.0451	1.75	2	3	5	6	0	0	0	0	0
65	0.0452	1.67	1.71	2	2.83	3	4.2	5	6	0	0
89	0.0452	1.67	1.71	2	2.83	3	4.8	5	5.25	6	0
28	0.0452	1.75	2	3	5	5.5	6	0	0	0	0
63	0.0453	1.83	2	3	4.67	5	5.5	5.67	6	0	0
89	0.0453	1.75	2	3	4.17	4.8	5	5.75	6	0	0
54	0.0453	1.75	2	3	4	4.67	4.8	6	0	0	0
83	0.0454	1.75	2	3	4.17	4.8	5	5.67	6	0	0
70	0.0454	1.75	2	2.71	3	4	4.8	5.5	6	0	0
75	0.0454	1.8	2	3	4.6	5	5.33	5.67	6	0	0
68	0.0454	1.8	2	3	3.8	4.2	4.5	5	6	0	0
33	0.0454	1.75	2	3	5	5.33	6	0	0	0	0
72	0.0455	1.75	2	3	4.25	4.5	5.5	5.75	6	0	0
69	0.0455	1.75	2	3	4.4	4.5	5.2	6	0	0	0
74	0.0455	1.8	2	3	3.8	4	4.67	5.75	6	0	0
38	0.0456	1.75	2	3	4.5	5.67	6	0	0	0	0
40	0.0456	1.75	2	3	5.5	5.67	6	0	0	0	0
44	0.0456	1.75	2	3	4.5	5.75	6	0	0	0	0
48	0.0456	1.8	2	3	5.5	5.75	6	0	0	0	0
44	0.0456	1.75	2	2.8	3	4	4.67	6	0	0	0
80	0.0457	1.6	1.83	2	3	4	4.2	5	5.2	6	0
51	0.0457	1.8	2	2.75	3	4.2	5	6	0	0	0
29	0.0457	1.75	2	3	5.67	6	0	0	0	0	0
67	0.0457	1.75	2	3	3.33	3.43	4	5.67	6	0	0
71	0.0458	1.75	2	3	4.4	5.25	5.33	6	0	0	0
46	0.0458	1.83	2	3	4	4.25	4.5	6	0	0	0
42	0.0458	1.75	2	3	4.2	4.5	6	0	0	0	0
42	0.0459	1.67	2	3	5	5.33	5.5	6	0	0	0
69	0.0459	1.67	1.86	2	3.13	3.75	4	5	6	0	0
16	0.0460	1.83	2	3	6	0	0	0	0	0	0
57	0.0460	1.75	2	3	4.2	4.8	6	0	0	0	0

61	0.0460	1.75	2	3	4.2	5.5	5.67	6	0	0	0
83	0.0460	1.75	2	3	3.6	3.67	4.6	4.67	5	6	0
39	0.0461	1.75	2	3	3.29	4	6	0	0	0	0
63	0.0462	1.5	1.71	2	3	4.75	4.8	6	0	0	0
54	0.0462	1.75	2	2.8	3	3.83	5	6	0	0	0
21	0.0462	1.67	2	3	5.5	6	0	0	0	0	0
62	0.0462	1.5	1.63	2	2.8	3	3.5	4	5	5.5	6
39	0.0462	1.67	2	3	3.33	3.75	4	6	0	0	0
95	0.0462	1.75	2	2.8	2.88	3	3.5	3.8	4.5	5.5	6
78	0.0463	1.75	2	3	3.83	4.4	5.25	6	0	0	0
65	0.0463	1.8	2	2.75	3	4.2	4.75	6	0	0	0
14	0.0464	2	3	4	5	6	0	0	0	0	0
61	0.0464	1.75	2	3	3.33	4	4.33	5	5.67	6	0
62	0.0464	1.83	1.88	2	3.57	4	5	6	0	0	0
37	0.0464	1.67	2	2.6	3	4.5	5	6	0	0	0
52	0.0464	1.83	2	3	3.5	4.8	5	6	0	0	0
70	0.0464	1.8	2	3	3.8	4.2	5.33	6	0	0	0
37	0.0465	2	3	4	5	5.75	6	0	0	0	0
38	0.0465	2	3	4	4.8	5	6	0	0	0	0
33	0.0465	1.67	2	2.8	3	4.5	6	0	0	0	0
36	0.0465	1.75	2	2.6	3	5.5	6	0	0	0	0
42	0.0465	2	3	4	5	5.5	5.67	6	0	0	0
31	0.0465	2	3	4	5	5.67	6	0	0	0	0
48	0.0465	1.75	2	2.67	3	4.25	5.5	6	0	0	0
26	0.0465	1.8	2	3	3.5	5	6	0	0	0	0
43	0.0465	2	3	4	5.5	5.75	6	0	0	0	0
37	0.0465	2	3	4	4.5	4.67	5	6	0	0	0
20	0.0466	2	3	4	5.5	6	0	0	0	0	0
69	0.0466	1.8	2	3.5	4	4.75	5	5.75	6	0	0
9	0.0466	2	3	4	6	0	0	0	0	0	0
80	0.0466	1.83	1.88	2	3.57	4	5.75	6	0	0	0
88	0.0466	1.75	2	3	3.33	4	4.33	5	5.25	5.75	6
94	0.0466	1.83	1.88	2	3.57	4	5	5.25	5.5	6	0
37	0.0466	2	3	4	4.6	5	6	0	0	0	0
23	0.0466	1.67	1.75	2	4	5	6	0	0	0	0
46	0.0466	1.75	2	3.6	3.75	4	6	0	0	0	0
56	0.0466	1.75	2	2.63	3	4.6	6	0	0	0	0
65	0.0467	1.75	2	3.25	3.67	4	4.6	5	6	0	0
34	0.0467	2	3	4	4.5	5	5.5	6	0	0	0
64	0.0467	1.75	1.8	2	2.5	3	3.6	3.75	5	6	0
49	0.0467	1.5	1.6	2	3	5	5.5	5.67	6	0	0
85	0.0467	1.75	2	2.71	3	3.8	4.8	5.5	6	0	0
30	0.0467	2	3	4	5	5.33	6	0	0	0	0
67	0.0467	1.6	2	3	4	4.4	5	5.75	6	0	0
66	0.0467	1.8	2	2.75	3	3.5	4.17	4.5	6	0	0
21	0.0468	1.5	1.86	2	3	6	0	0	0	0	0
44	0.0468	1.75	1.8	2	4	5	5.67	6	0	0	0
53	0.0468	1.67	2	3	3.2	3.83	4	6	0	0	0
60	0.0468	1.67	2	2.5	2.8	3	4.4	4.5	6	0	0
38	0.0468	1.75	2	3.57	4	6	0	0	0	0	0

Table 10.2. Top Sequences with $V_c = 0.3$ and phasing (PH). (See preceding paragraphs for column descriptions).

T	ΔV	Sequence									
52	0.0500	1.67	1.75	2	5	0	5.33	5.67	6	0	0
53	0.0502	1.67	1.86	2	5	0	5.5	5.67	6	0	0
36	0.0503	1.67	1.86	2	5	0	5.5	6	0	0	0
36	0.0507	1.67	1.75	2	5	0	5.67	6	0	0	0
42	0.0509	1.75	2	5	0	5.5	5.67	6	0	0	0
25	0.0509	1.75	2	5	0	5.5	6	0	0	0	0
31	0.0512	1.75	2	5	0	5.67	6	0	0	0	0
29	0.0518	1.67	2	5	0	5.67	6	0	0	0	0
14	0.0518	1.75	2	5	0	6	0	0	0	0	0
35	0.0519	1.67	2	5	0	5.75	6	0	0	0	0
18	0.0520	1.83	2	5	0	6	0	0	0	0	0
17	0.0521	1.5	1.75	2	5	0	6	0	0	0	0
12	0.0524	1.67	2	5	0	6	0	0	0	0	0
34	0.0524	2	5	0	5.33	5.5	6	0	0	0	0
45	0.0524	2	5	0	5.25	5.67	6	0	0	0	0
44	0.0525	2	5	0	5.25	5.33	6	0	0	0	0
28	0.0525	2	5	0	5.25	6	0	0	0	0	0
23	0.0526	2	5	0	5.33	6	0	0	0	0	0
18	0.0528	2	5	0	5.5	6	0	0	0	0	0
24	0.0531	2	5	0	5.67	6	0	0	0	0	0
42	0.0534	1.5	2	5	0	5.25	5.5	6	0	0	0
37	0.0534	1.5	2	5	0	5.33	5.5	6	0	0	0
36	0.0535	1.5	2	5	0	5.2	6	0	0	0	0
15	0.0535	1.6	2	5	0	6	0	0	0	0	0
7	0.0537	2	5	0	6	0	0	0	0	0	0
21	0.0538	1.5	2	5	0	5.5	6	0	0	0	0
27	0.0541	1.5	2	5	0	5.67	6	0	0	0	0
33	0.0542	1.5	2	5	0	5.75	6	0	0	0	0
10	0.0547	1.5	2	5	0	6	0	0	0	0	0
14	0.0627	1.4	2	5	0	6	0	0	0	0	0
42	0.0679	1.8	1.86	2.14	5	0	6	0	0	0	0
27	0.0680	1.33	2	5	0	5.33	6	0	0	0	0
27	0.0682	1.8	2.17	5	0	6	0	0	0	0	0
22	0.0682	2	2.14	5	0	6	0	0	0	0	0
39	0.0682	2	2.13	2.14	5	0	6	0	0	0	0
41	0.0688	1.6	1.83	2.13	5	0	6	0	0	0	0
24	0.0689	2	2.13	5	0	6	0	0	0	0	0
11	0.0691	1.33	2	5	0	6	0	0	0	0	0
69	0.0716	1.83	1.88	4	0	5	5.5	5.75	6	0	0
31	0.0720	1.8	1.86	4	0	5	6	0	0	0	0
21	0.0726	1.5	2.17	5	0	6	0	0	0	0	0
48	0.0728	1.67	1.83	4	0	5	5.75	6	0	0	0
78	0.0728	1.75	1.8	4	0	4.75	5	5.5	5.75	6	0
61	0.0729	1.5	1.88	4	0	5	5.5	5.75	6	0	0
62	0.0729	1.67	1.88	5	0	5.25	5.33	6	0	0	0
65	0.0731	1.5	1.88	4	0	5	5.25	5.67	6	0	0
55	0.0733	1.75	1.8	4	0	4.75	5.33	6	0	0	0

28	0.0733	1.6	1.83	4	0	5	6	0	0	0	0
25	0.0734	1.5	1.86	4	0	5	6	0	0	0	0
46	0.0734	1.67	1.75	4	0	4.5	5	5.33	6	0	0
68	0.0734	1.5	1.6	1.88	5	0	5.25	5.33	6	0	0
36	0.0735	1.5	1.86	4	0	5	5.5	6	0	0	0
39	0.0735	1.75	1.8	4	0	4.75	6	0	0	0	0
27	0.0736	1.8	4	0	4.67	6	0	0	0	0	0
47	0.0737	1.83	1.88	5	0	5.33	6	0	0	0	0
42	0.0737	1.75	4	0	4.5	5	5.67	6	0	0	0
23	0.0740	1.67	1.8	4	0	5	6	0	0	0	0
34	0.0742	1.67	1.8	4	0	5	5.5	6	0	0	0
60	0.0742	1.8	4	0	4.8	5.75	6	0	0	0	0
62	0.0743	1.67	1.8	4	0	5	5.33	5.75	6	0	0
29	0.0743	1.5	1.6	1.8	4	0	5	6	0	0	0
36	0.0743	1.75	1.8	4	0	5	5.5	6	0	0	0
61	0.0749	1.8	1.86	5	0	5.5	5.75	6	0	0	0
56	0.0751	1.8	4	0	5	5.25	5.67	6	0	0	0
35	0.0754	1.75	4	0	4.75	5	6	0	0	0	0
51	0.0754	1.6	1.83	5	0	5.33	5.5	6	0	0	0
46	0.0755	1.75	4	0	4.75	5	5.5	6	0	0	0
37	0.0755	1.5	1.86	5	0	5.33	6	0	0	0	0
35	0.0756	1.67	1.75	4	0	4.75	6	0	0	0	0
34	0.0757	1.5	1.88	5	0	5.5	6	0	0	0	0
51	0.0757	1.75	4	0	4.75	5	5.33	6	0	0	0
23	0.0757	1.5	1.63	3	0	4	6	0	0	0	0
81	0.0759	1.5	1.63	3	0	4	4.67	5	5.33	5.75	6
30	0.0761	1.75	4	0	4.75	6	0	0	0	0	0
49	0.0762	1.5	1.86	5	0	5.5	5.67	6	0	0	0
32	0.0762	1.5	1.86	5	0	5.5	6	0	0	0	0
21	0.0764	1.67	1.75	4	0	5	6	0	0	0	0
44	0.0765	1.67	1.75	4	0	5	5.75	6	0	0	0
91	0.0766	1.67	1.75	4	0	5	5.2	5.33	5.5	5.67	6
40	0.0767	1.5	3	0	3.57	4	5	6	0	0	0
58	0.0767	1.67	1.75	4	0	5	5.2	5.5	6	0	0
27	0.0769	1.67	4	0	4.33	5	6	0	0	0	0
60	0.0769	1.67	4	0	4.33	4.4	5	5.5	6	0	0
61	0.0769	1.67	4	0	4.33	5	5.5	5.75	6	0	0
68	0.0769	1.5	3	0	3.57	4	5.33	5.67	6	0	0
44	0.0770	1.67	4	0	4.33	5	5.67	6	0	0	0
80	0.0770	1.67	4	0	4.33	4.5	4.6	5	5.25	6	0
38	0.0771	1.5	1.86	5	0	5.67	6	0	0	0	0
36	0.0771	1.5	1.63	3	0	4	4.33	6	0	0	0
56	0.0771	1.5	3	0	3.57	4	5.25	6	0	0	0
27	0.0772	1.8	1.86	5	0	6	0	0	0	0	0
73	0.0773	1.67	4	0	4.33	4.67	5.25	5.33	6	0	0
54	0.0773	1.67	4	0	4.33	5.25	5.5	6	0	0	0
29	0.0773	1.5	1.6	3	0	4	5.5	6	0	0	0
45	0.0773	1.5	1.6	3	0	4	5.33	5.5	6	0	0
44	0.0774	1.5	1.86	5	0	5.75	6	0	0	0	0
47	0.0775	1.6	1.83	5	0	5.75	6	0	0	0	0

Table 10.3. Top Sequences with $V_c = 0.3$ and non-tangential (NT) leveraging. (See preceding paragraphs for column descriptions).

T	ΔV	Sequence							
43	0.0505	1.8	2	0.06	5.25	5.5	6	0	0
30	0.0506	1.75	2	0.06	5.25	6	0	0	0
51	0.0507	1.75	2	0.05	5.2	5.33	6	0	0
62	0.0507	1.83	2	0.05	5.2	5.75	6	0	0
31	0.0507	1.67	1.75	2	0.06	5.67	6	0	0
36	0.0509	1.75	2	0.07	5.4	6	0	0	0
41	0.0509	1.6	1.67	2	0.05	5.2	6	0	0
37	0.0512	1.75	2	0.05	5.6	6	0	0	0
33	0.0512	1.67	2	0.05	5.2	6	0	0	0
26	0.0512	1.75	2	0.06	5.67	6	0	0	0
39	0.0512	1.8	2	0.05	5.6	6	0	0	0
34	0.0515	1.67	2	0.07	5.4	6	0	0	0
7	0.0522	2	0.1	5	6	0	0	0	0
62	0.0523	2	0.05	5.2	5.5	5.75	6	0	0
39	0.0523	2	0.05	5.2	5.5	6	0	0	0
34	0.0524	2	0.06	5.25	5.5	6	0	0	0
51	0.0524	2	0.05	5.2	5.75	6	0	0	0
46	0.0524	2	0.06	5.25	5.75	6	0	0	0
40	0.0525	2	0.06	5.25	5.67	6	0	0	0
28	0.0525	2	0.05	5.2	6	0	0	0	0
23	0.0525	2	0.06	5.25	6	0	0	0	0
44	0.0525	2	0.05	5.2	5.33	6	0	0	0
52	0.0527	2	0.07	5.4	5.75	6	0	0	0
29	0.0528	2	0.07	5.4	6	0	0	0	0
30	0.0531	2	0.05	5.6	6	0	0	0	0
19	0.0531	2	0.06	5.67	6	0	0	0	0
55	0.0537	1.5	2	0.07	5.4	5.75	6	0	0
49	0.0538	1.5	2	0.07	5.4	5.67	6	0	0
32	0.0538	1.5	2	0.07	5.4	6	0	0	0
39	0.0550	2	0.1	5	5.25	5.5	6	0	0
51	0.0551	2	0.1	5	5.25	5.75	6	0	0
28	0.0552	2	0.1	5	5.25	6	0	0	0
39	0.0553	1.4	1.5	2	0.07	5.4	6	0	0
34	0.0598	1.33	1.57	2	0.06	5.67	6	0	0
44	0.0679	1.33	2	0.06	5.25	5.67	6	0	0
34	0.0685	1.33	2	0.05	5.6	6	0	0	0
30	0.0715	1.75	1.8	0.08	4.5	5	6	0	0
42	0.0721	1.75	1.8	0.08	4.5	5.67	6	0	0
95	0.0722	1.8	1.86	0.1	4.8	5.25	5.5	5.67	6
67	0.0722	1.75	1.86	0.1	4.8	5.75	6	0	0
67	0.0724	1.8	1.86	0.1	4.8	5.25	6	0	0
85	0.0724	1.67	1.75	1.83	0.1	4.8	5.25	5.67	6
63	0.0724	1.8	1.86	0.1	4.8	5.67	6	0	0
69	0.0725	1.8	1.86	0.1	4.8	5.75	6	0	0

46	0.0726	1.8	1.86	0.1	4.8	6	0	0	0
81	0.0731	1.67	1.75	0.08	4.4	4.75	5	5.75	6
45	0.0731	1.6	1.86	0.1	4.8	6	0	0	0
39	0.0732	1.67	1.75	0.08	4.4	5	6	0	0
28	0.0732	1.8	0.07	4.67	5	6	0	0	0
73	0.0732	1.67	1.75	0.08	4.4	5	5.5	5.75	6
27	0.0733	1.8	1.86	0.1	5	6	0	0	0
92	0.0735	1.67	1.75	0.08	4.4	4.8	5.5	5.75	6
89	0.0736	1.67	1.75	0.08	4.4	5.25	5.5	5.75	6
71	0.0736	1.6	1.83	0.1	4.8	5.5	5.67	6	0
65	0.0736	1.67	1.75	0.08	4.4	5	5.2	6	0
44	0.0736	1.67	1.86	0.05	5.2	6	0	0	0
68	0.0737	1.67	1.75	0.08	4.4	4.6	5.5	6	0
57	0.0738	1.5	1.86	0.1	4.8	5.67	6	0	0
50	0.0738	1.67	1.75	0.08	4.4	5.33	6	0	0
43	0.0739	1.6	1.83	0.1	4.8	6	0	0	0
51	0.0739	1.67	1.75	0.08	4.4	5.67	6	0	0
40	0.0739	1.5	1.86	0.1	4.8	6	0	0	0
57	0.0739	1.67	1.75	0.08	4.4	5.75	6	0	0
34	0.0741	1.67	1.75	0.08	4.4	6	0	0	0
35	0.0741	1.83	0.1	4.8	6	0	0	0	0
21	0.0741	1.75	0.08	4.5	5	6	0	0	0
44	0.0742	1.67	1.75	0.08	4.5	5.75	6	0	0
40	0.0742	1.67	1.75	0.06	4.6	5	6	0	0
63	0.0743	1.67	1.75	0.06	4.6	5	5.75	6	0
70	0.0743	1.75	0.08	4.5	5	5.25	5.5	5.67	6
51	0.0745	1.75	1.8	0.1	4.8	5.5	6	0	0
42	0.0745	1.75	0.08	4.5	5	5.25	6	0	0
49	0.0746	1.75	0.08	4.5	5.33	5.67	6	0	0
56	0.0746	1.75	1.8	0.1	4.8	5.33	6	0	0
32	0.0747	1.75	0.08	4.5	5.33	6	0	0	0
63	0.0747	1.75	1.8	0.1	4.8	5.75	6	0	0
42	0.0748	1.5	1.63	1.75	0.07	4.67	5	6	0
16	0.0749	1.75	0.08	4.5	6	0	0	0	0
49	0.0752	1.8	0.1	4.8	5.33	6	0	0	0
33	0.0753	1.8	0.1	4.8	6	0	0	0	0
40	0.0755	1.6	1.83	0.06	5.25	6	0	0	0
43	0.0755	1.83	1.88	0.06	5.67	6	0	0	0
61	0.0761	1.5	1.71	0.08	4.4	4.8	6	0	0
58	0.0762	1.5	1.83	0.06	5.25	5.75	6	0	0
51	0.0762	1.67	1.75	1.83	0.08	5.6	6	0	0
65	0.0764	1.5	1.63	0.13	3.8	4.17	5	6	0
49	0.0765	1.6	1.86	0.08	5.6	6	0	0	0
70	0.0767	1.67	1.75	0.1	4.8	5.5	5.75	6	0
69	0.0768	1.5	1.63	0.13	3.8	4.17	4.5	6	0
30	0.0771	1.6	1.83	0.08	5.5	6	0	0	0
79	0.0772	1.5	1.67	0.08	4.25	5	5.2	5.75	6
60	0.0773	1.75	1.8	0.07	5.4	5.67	6	0	0
43	0.0773	1.75	1.8	0.07	5.4	6	0	0	0
65	0.0773	1.5	0.09	3.5	4	4.25	4.6	5.5	6

Table 10.4. Most efficient sequences for $V_c = 0.2$.

T	ΔV	Sequence										
37	0.05262	1.5	1.6	1.67	2	3	0.09	5.33	6	0	0	0
58	0.05264	1.4	1.5	1.78	2	0.15	3	0.08	4.4	5	6	0
74	0.05275	1.5	1.8	2	3	4.33	5	5.5	5.6	6	0	0
100	0.05413	1.5	1.6	2	2.71	2.75	3	5	0	5.2	5.75	6
75	0.05421	1.5	1.6	2	2.67	3	0.1	4.8	5.33	5.5	6	0
26	0.05446	1.67	1.75	2	0.13	3	4	0	5	6	0	0
44	0.05451	1.5	2	3	4	5	5.4	6	0	0	0	0
48	0.05456	1.5	1.6	2	2.67	3	0.1	4.8	6	0	0	0
81	0.05457	1.67	1.75	2	2.86	3	0.08	5.25	5.75	6	0	0
61	0.05460	1.5	2	3	4	5.2	5.75	6	0	0	0	0
22	0.05467	1.5	1.67	2	3	0	4	5	6	0	0	0
17	0.05487	1.5	2	3	4	0	5	6	0	0	0	0
66	0.05490	1.67	1.75	2	0.13	3	5	0	5.25	5.75	6	0
37	0.05491	1.67	2	3	4	5.75	6	0	0	0	0	0
38	0.05493	1.67	1.89	2	3	0.1	5.5	6	0	0	0	0
17	0.05494	1.6	2	3	4	6	0	0	0	0	0	0
61	0.05495	1.5	1.71	2	0.08	3.2	3.5	4	4.25	6	0	0
61	0.05496	1.5	2	3	4.5	5	5.33	5.75	6	0	0	0
43	0.05499	1.67	1.75	2	0.13	3	5	0	5.25	6	0	0
37	0.05500	1.5	2	3	4	4.5	5.33	6	0	0	0	0
12	0.05505	1.5	2	0.14	3	4	6	0	0	0	0	0
26	0.05514	1.67	2	3	3.5	4	5	6	0	0	0	0
54	0.05531	1.5	2	3	0.05	4.75	5.4	6	0	0	0	0
38	0.05532	1.5	2	3	0.07	4.67	5.33	6	0	0	0	0
45	0.05532	1.4	1.43	1.75	2	0.13	3	5	0	5.5	6	0
41	0.05536	1.5	2	3	0.09	5.33	5.67	6	0	0	0	0
48	0.05540	1.5	2	3	0.06	4.6	5.67	6	0	0	0	0
34	0.05543	1.5	2	3	5	0	5.25	6	0	0	0	0
41	0.05544	1.5	2	3	5	0	5.6	6	0	0	0	0
59	0.05547	1.5	2	0.13	3	0.1	4.8	5.4	6	0	0	0
13	0.05558	1.5	2	3	5	0	6	0	0	0	0	0
55	0.05561	1.5	2	3	4	0	4.75	4.8	6	0	0	0
26	0.05562	1.5	2	3	4	0	4.67	6	0	0	0	0
62	0.05563	1.5	2	2.71	3	4.5	5.2	6	0	0	0	0
18	0.05563	1.6	2	3	0.1	5	6	0	0	0	0	0
83	0.05564	1.5	1.67	2	0.19	3.8	4.5	4.6	5	5.67	6	0
109	0.05566	1.5	2	2.78	3	4.33	5.2	5.25	5.33	6	0	0
51	0.05568	1.75	2	3	3.8	4	5	5.5	6	0	0	0
37	0.05570	1.5	1.6	2	3	0	3.5	4.5	5	6	0	0
43	0.05575	1.75	2	3	4	5.4	6	0	0	0	0	0
70	0.05579	1.67	2	3	5	0	5.4	5.6	6	0	0	0
47	0.05580	1.5	2	2.67	2.86	3	0.1	5.5	6	0	0	0
59	0.05581	1.67	2	3	5	0	5.25	5.75	6	0	0	0
57	0.05583	1.5	2	0.17	3	5	0	5.4	5.67	6	0	0
44	0.05585	1.5	2	3	4.17	5.5	6	0	0	0	0	0
97	0.05585	1.5	2	2.63	3	0.1	4.8	5.25	5.75	6	0	0
78	0.05587	1.5	1.56	1.86	2	2.78	4	5.67	6	0	0	0

Table 10.5. Fastest sequences for $V_c = 0.2$.

T	ΔV	Sequence					
0	0.13147	6	0	0	0	0	0
4	0.10834	4	6	0	0	0	0
5	0.12155	5	6	0	0	0	0
6	0.06593	2	0.23	4	6	0	0
6	0.06654	2	0.25	4	6	0	0
6	0.06712	2	0.27	4	6	0	0
6	0.06723	2	0.27	4	6	0	0
6	0.06741	2	0.28	4	6	0	0
6	0.06750	2	0.29	4	6	0	0
6	0.06775	2	0.29	4	6	0	0
6	0.06800	2	0.3	4	6	0	0
6	0.06816	2	4	0	6	0	0
7	0.08917	3	4	6	0	0	0
8	0.08986	3	0.1	5	6	0	0
8	0.08989	3	0.11	5	6	0	0
8	0.09031	3	5	0	6	0	0
9	0.05996	1.5	2	0.25	4	6	0
9	0.06092	1.5	2	0.29	4	6	0
9	0.06103	2	3	4	6	0	0
9	0.06142	1.5	2	0.3	4	6	0
9	0.06158	1.5	2	4	0	6	0
9	0.06372	2	3	0	4	6	0
9	0.10814	4	5	6	0	0	0
9	0.11635	4.5	6	0	0	0	0
10	0.06172	2	3	0.1	5	6	0
10	0.06216	2	3	5	0	6	0
10	0.07147	1.33	2	0.25	4	6	0
10	0.07309	1.33	2	4	0	6	0
10	0.08771	2.5	0.18	5	6	0	0
10	0.08810	2.5	5	0	6	0	0
10	0.08826	2.5	0.17	5	6	0	0
10	0.08838	1.5	3	0	4	6	0
10	0.09238	1.5	0.31	3	4	6	0
10	0.13789	1.33	2	0	4	0	6
11	0.06042	1.67	2	0.25	4	6	0
11	0.06100	1.67	2	0.27	4	6	0
11	0.06111	1.67	2	0.27	4	6	0
11	0.06163	1.67	2	0.29	4	6	0
11	0.06188	1.67	2	0.3	4	6	0
11	0.06204	1.67	2	4	0	6	0
11	0.06597	2	4	0	5	6	0
11	0.06621	2	0.23	4	5	6	0
11	0.08531	1.5	0.28	3	0.11	5	6
11	0.08751	1.5	0.31	3	0.11	5	6
11	0.08838	2.33	4	0	6	0	0
11	0.09512	1.5	0.37	3	5	0	6
11	0.10021	3.5	4	6	0	0	0

Table 10.6 Fastest sequences for $V_c = 0.1$.

T	ΔV	Sequence									
0	0.1919	6	0	0	0	0	0	0	0	0	0
24	0.2696	1.67	0.62	2	5.67	0	6	0	0	0	0
28	0.1862	5.5	5.67	0	6	0	0	0	0	0	0
31	0.1721	4.5	0.15	5	5.67	0	6	0	0	0	0
33	0.1793	5	5.5	0	5.67	0	6	0	0	0	0
34	0.1882	5.67	5.67	0	6	0	0	0	0	0	0
34	0.1861	5.5	5.75	6	0	0	0	0	0	0	0
35	0.2633	1.67	0.61	2	5.5	0	5.67	0	6	0	0
35	0.2597	1.67	0.61	2	5.5	0	5.67	0	6	0	0
35	0.1706	4.33	0.17	5	5.67	0	6	0	0	0	0
36	0.2775	1.67	0.62	2	5.8	0	6	0	0	0	0
38	0.2651	1.6	0.61	2	5.5	0	5.67	0	6	0	0
39	0.1794	5	5.5	0	5.75	6	0	0	0	0	0
39	0.1683	4.25	0.15	5	5.67	0	6	0	0	0	0
39	0.1628	4	0.11	4.33	0.15	5	5.67	0	6	0	0
40	0.2586	1.67	0.59	2	5	0	5.5	0	5.67	0	6
42	0.1723	4.5	5	0	5.5	0	5.67	0	6	0	0
42	0.1720	4.5	0.14	5	5.5	0	5.67	0	6	0	0
42	0.1720	4.5	0.13	5	5.5	0	5.67	0	6	0	0
42	0.1718	4.5	0.11	5	5.5	0	5.67	0	6	0	0
42	0.1718	4.5	0.1	5	0.08	5.5	5.67	0	6	0	0
43	0.1641	4	0.08	4.25	0.17	5	5.67	0	6	0	0
44	0.1842	5.33	5.5	0	5.67	0	6	0	0	0	0
44	0.1841	5.33	5.5	5.67	0	6	0	0	0	0	0
44	0.1840	5.33	0.07	5.5	5.67	0	6	0	0	0	0
45	0.1862	5.5	5.67	5.67	0	6	0	0	0	0	0
45	0.1793	5	0.1	5.5	5.8	0	6	0	0	0	0
46	0.1699	4.33	5	0	5.5	0	5.67	0	6	0	0
46	0.1623	4	0.13	4.5	5	0	5.5	0	5.67	0	6
46	0.1621	4	0.18	4.67	5.5	0	5.67	0	6	0	0
46	0.1620	4	0.19	4.67	5.5	0	5.67	0	6	0	0
46	0.1619	4	0.13	4.5	0.1	5	5.5	0	5.67	0	6
47	0.2649	1.67	1.71	0.61	2	5.5	0	5.67	0	6	0
47	0.1752	4.67	5	0	5.5	0	5.67	0	6	0	0
47	0.1749	4.67	0.11	5.33	5.67	0	6	0	0	0	0
47	0.1747	4.67	0.11	5	0.08	5.5	5.67	0	6	0	0
47	0.1747	4.67	0.11	5	0.07	5.5	5.67	0	6	0	0
47	0.1747	4.67	0.11	5	5.5	0	5.67	0	6	0	0
48	0.1722	4.5	5	0	5.5	0	5.75	6	0	0	0
48	0.1634	4	0.15	4.4	0.17	5	5.67	0	6	0	0
48	0.1626	4	0.11	4.4	0.15	5	5.67	0	6	0	0
49	0.1795	5	0.05	5.33	5.5	0	5.67	0	6	0	0
49	0.1794	5	0.05	5.33	5.5	5.67	0	6	0	0	0
49	0.1794	5	0.07	5.4	5.67	0	6	0	0	0	0